Closed-loop Throttle Control of a Hybrid Rocket Motor

Timothy Johnathan Velthuysen

Submitted in fulfilment of the academic requirements for the degree of Master of Science in Mechanical Engineering, College of Agriculture, Engineering and Science, University of KwaZulu-Natal.

Durban, South Africa

August 2018

Supervisor: Dr Michael J. Brooks

Co-Supervisor: Mr Jean-Francois Pitot de la Beaujardiere

DECLARATION 1 – PLAGIARISM

I, Timothy Johnathan Velthuysen, declare that

1. The research reported in this thesis, except where otherwise indicated, is my original research.

2. This thesis has not been submitted for any degree or examination at any other university.

3. This thesis does not contain other persons' data, pictures, graphs or other information, unless specifically acknowledged as being sourced from other persons.

4. This thesis does not contain other persons' writing, unless specifically acknowledged as being sourced from other researchers. Where other written sources have been quoted, then:
   a. Their words have been re-written but the general information attributed to them has been referenced
   b. Where their exact words have been used, then their writing has been placed in italics and inside quotation marks, and referenced.

5. This thesis does not contain text, graphics or tables copied and pasted from the Internet, unless specifically acknowledged, and the source being detailed in the thesis and in the References sections.

Signed:………………………………………… Date:…………………………………………

Mr Timothy Johnathan Velthuysen

DECLARATION 2 – PUBLICATIONS

Velthuysen T.*, Broughton K., Brooks, M., Pitot de la Beaujardiere J.P., Lineberry, D., and Tingley E., "Safety Aspects of Nitrous Oxide Use in Hybrid Rocket Motor Design and Testing", July 9-11, 2018 AIAA/ASME/SAE/ASEE Joint Propulsion Conference and Exhibit, Cincinnati, Ohio.

Velthuysen T., Brooks M.J. and Pitot de la Beaujardiere J.-F., "Closed Loop Throttle Control for a Nitrous Oxide/Paraffin Wax Hybrid Rocket Motor", Annual Conference of the Aeronautical Society of South Africa (AESSA), CSIR, Pretoria, October 2017

*Primary Author

Signed:…………………………………………… Date:………………………………………
Mr Timothy Johnathan Velthuysen

As the candidate's supervisor I agree/do not agree to the submission of this thesis.

Signed:…………………………………………… Date:………………………………………
Dr Michael J. Brooks

As the candidate's co-supervisor I agree/do not agree to the submission of this thesis.

Signed:…………………………………………… Date:………………………………………
Mr Jean-Francois Pitot de la Beaujardiere

Ad majorem Dei gloriam

ABSTRACT

Hybrid rocket motors produce thrust by reacting a solid fuel with a liquid oxidizer inside a combustion chamber. This approach has certain advantages over conventional solid propellant rockets including improved safety and the potential for thrust control, while also being less expensive than liquid propellant engines. Liquefying hybrid fuels, such as paraffin wax, regress at a faster rate than the conventional solid fuels like HTPB that are dominated by vaporization at the solid-gas interface. Non-classical theory is still in its infancy, however, and more work is required to validate performance models experimentally, especially where throttling of the oxidizer mass flowrate is incorporated.

While hybrid motor throttlabilty remains a subject of considerable interest, there has been little investigation of throttling in motors that use high regression rate, liquefying fuels such as paraffin wax. This study proposes a closed-loop thrust control scheme for paraffin wax/nitrous oxide hybrid rocket motors using a low-cost ball valve as the controlling hardware element.

There are a number of advantages to throttling hybrid rocket motors but the most important is to enforce a constant thrust curve throughout the burn. A test facility and laboratory scale hybrid rocket motor utilizing paraffin wax as fuel and nitrous oxide as oxidiser were used for experimental testing. Using a mathematical model of a laboratory-scale hybrid rocket motor, the controller constants for a PID controller were obtained and tested through experimental testing. Open-loop testing was first done in order to determine the control authority of the ball valve over the oxidiser mass flowrate, as well as characterize the oxidiser mass flowrate in relation to each valve angle value.

Closed-loop testing was undertaken to verify and refine the controller constants obtained via the laboratory-scale model. The tests prompted a redesign of the injector and additions to the LabVIEW™ controller regime. Using results from the open-loop tests a feed-forward lookup table was developed to allow for the controller to move to a specified angle quickly and thereby remove nonlinearities present in flow control using ball valves. Three successful closed-loop tests were done where the controller causes the thrust of the motor to track a predetermined thrust or chamber pressure set point with a reasonable degree of accuracy. The set-point profile of the first test was a constant thrust throughout the burn while the second test had a ramp set-point profile. The final test used chamber pressure as the feedback variable and had a step-down set-point profile.

This study demonstrates that thrust control can be exercised over a paraffin wax/nitrous oxide hybrid rocket motor, using a low-cost ball valve as the control element to modulate the oxidiser mass flowrate.

CONTENTS

LIST OF FIGURES

LIST OF TABLES

NOMENCLATURE

Symbols	Description	Units
a	Regression rate ballistic coefficient	-
a_e	Nozzle exit velocity of sound	m/s
a_{ent}	Entrainment coefficient	-
A_b	Burnt cross-sectional area	m^2
A_e	Nozzle exit area	m^2
A_{inj}	Injector orifice cross-sectional area	m^2
A_p	Grain port cross-sectional area	m^2
A_t	Nozzle throat area	m^2
c_P	Specific heat capacity at constant pressure	kJ/kg
c_V	Specific heat capacity at constant volume	kJ/kg
c^*	Characteristic velocity	m/s
C_d	Discharge coefficient	-
C_F	Thrust coefficient	-
C_r	Contraction ratio	-
$\bar{C}_P$	Molar heat capacity at constant pressure	kJ/kg
$\bar{C}_V$	Molar heat capacity at constant volume	kJ/kg
C_H / C_{HO}	Blocking factor	-
D	Diameter	m
$D_{p,f}$	Final port diameter	m
$D_{p,i}$	Initial port diameter	m
E	Young's modulus	MPa
F	Thrust	N
F_r	Roughness parameter	-
G	Mass flux rate	kg/m^2·s
G_{ox}	Oxidiser mass flux rate	kg/m^2·s
h	Specific Enthalpy	J/kg
h_e	Total heat of entrainment	J
h_m	Total heat of melting	J

H	Enthalpy	J
$\bar{H}$	Molar enthalpy	J/mol
I_{sp}	Specific impulse	s
I_t	Total impulse	Ns
I_{vac}	Vacuum specific impulse	s
k	Specific heat ratio	-
k_c	Chamber specific heat ratio	-
k_e	Nozzle exit specific heat ratio	-
L_c	Conical-shaped nozzle cone length	m
L_{cx}	Contraction angle point to throat plane length	m
Lg	Grain length	m
L_v	Latent heat of vaporization	J/mol
m	Mass	kg
$\dot{m}$	Mass flow rate	kg/s
$\dot{m}_f$	Fuel mass flowrate	kg/s
$\dot{m}_{ox}$	Oxidiser mass flowrate	kg/s
$\dot{m}_{noz}$	Nozzle mass flowrate	kg/s
M_e	Nozzle exit Mach number	-
M_t	Nozzle throat Mach number	-
M_{N2O}	Nitrous oxide mass in tank	kg
$M1$	Mach number before shock	-
$M2$	Mach number after shock	-
MW	Molecular weight	unitless or amu
n	Number of moles	-
n_{ox}	Total number of moles of nitrous oxide	-
$\dot{n}$	Number of moles of fluid flowrate	moles/s
N_{inj}	Number of injector orifices	-
O/F	Oxidiser-to-fuel ratio	-
P	Pressure	Pa or bar
P_a	Atmospheric pressure	bar
P_c	Chamber pressure	bar

P_e	Nozzle exit pressure	bar
P_{losses}	Pressure drop in feed line	Pa or bar
P_{ox}^*	Saturated vapour pressure of nitrous oxide	Pa
$P_{o,c}$	Chamber stagnation pressure	Pa
$P_{o,e}$	Nozzle exit stagnation pressure	Pa
$P_{o,1}$	Stagnation pressure before shock	Pa
$P_{o,2}$	Stagnation pressure after shock	Pa
P_1	Static pressure before shock	Pa
P_2	Static pressure after shock	Pa
P_{1st}	Nozzle first critical pressure ratio	-
P_{2nd}	Nozzle second critical pressure ratio	-
P_{3rd}	Nozzle third critical pressure ratio	-
Q	Heat transfer energy	J
$\dot{Q}_c$	Convective heat transfer	J/s
$\dot{Q}_r$	Radiative heat transfer	J/s
r_i	Inner radius	m
r_o	Outer radius	m
$\dot{r}$	Regression rate	m/s
$\dot{r}_{ent}$	Entrainment regression rate	m/s
$\dot{r}_v$	Vaporisation regression rate	m/s
R	Gas constant, Radius	- or m
R_c	Chamber gas constant	-
R_e	Nozzle exit gas constant	-
R_{he}	Non-dimensional energy parameter for entrainment	-
R_{hv}	Non-dimensional energy parameter for vaporisation	-
R_p	Port radius	m
R_u	Universal gas constant	-
s	Specific entropy	J/kg·K
t_b	Burn time	s
T	Temperature	°C or K

T_c	Chamber static temperature	K
T_e	Nozzle exit static temperature	K
T_m	Melting temperature	K
$T_{o,c}$	Chamber stagnation temperature	K
$T_{o,e}$	Nozzle exit stagnation temperature	K
u	Specific internal energy	J/kg
U	Internal energy	J
$\bar{U}$	Molar internal energy	J
v_e	Nozzle exit velocity	m/s
v_{in}	Nozzle inlet velocity	m/s
V	Volume	m^3
$V_{f,f}$	Final fuel grain volume	m^3
$V_{f,i}$	Initial fuel grain volume	m^3
$\bar{V}$	Molar volume	m^3/mol
W	Work done	J
x	Axial port distance	m
ΔH	Molar heat of vaporization	J/mol
Δs	Entropy change	J/K
α	Coefficient of thermal expansion	-
α_c	Conical nozzle diverging cone half-angle	degrees
β	Blowing coefficient	-
ε_r	Nozzle expansion ratio	-
λ	Nozzle exit angle correction factor	-
η_{eff}	Combustion efficiency	%
θ_c	Nozzle contraction angle	degrees
κ	Thermal conductivity	W/m·K
λ_c	Conical-shaped nozzle correction factor	-
μ	Combustion gas viscosity	Pa·s
ν	Poisson's ratio	-
ρ	Density	kg/m^3

| ρ_e | Nozzle exit density | kg/m^3 |

Subscripts

a	Atmospheric
Al	Aluminium
c	Combustion chamber
e	Exit
f	Fuel
g	Gas or Grain
in	Inflow
l	Liquid
noz	Nozzle
opt	optimum
ox	Oxidiser
ox,o	Oxidiser outflow
ox,l	Liquid oxidiser
ox,v	Vapour oxidiser
sp,v	Supercharge gas
st	Steel
t	Total, Throat
the	Theoretical
T	Tank
v	Vapour
vac	Vacuum

Abbreviations

AMROC	American Rocket Company
ASReG	Aerospace Systems Research Group
CEA	Chemical Equilibrium with Applications
CFD	Computational Fluid Dynamics
DARE	Delft Aerospace Rocket Engineering
GIRD	Gruppa Izucheniya Reaktivnogo Dvizheniya

HEM	Homogenous Equilibrium Model
HRM	Hybrid Rocket Motor
HRPC	Hybrid Rocket Performance Code
HYROPS	Hybrid Rocket Performance Simulator
LEX	Lithergol EXperimental
LOX	Liquid Oxygen
LSPC	Laboratory-Scale Performance Code
NASA	National Aeronautics and Space Administration
ONERA	Office National d'Études et de Recherches Aérospatiales
PWM	Pulse Width Modulation
UKZN	University of KwaZulu-Natal
USA	United States of America
VOF	Volume of Fluid

1 HYBRID ROCKET MOTORS

1.1 INTRODUCTION

Since the early 1960s conventional space launch systems have been developed with extensive capabilities, however the operating costs of these vehicles have increased proportionally. This increase in costs is attributed to increasing operational and manufacturing complexity as well as stringent safety and environmental regulations regarding the propellants used. Solid and liquid-propelled rocket stages are still in wide use in both the commercial and governmental sectors due to their high thrust-to-weight ratios and proven performance over the years. For these reasons both solid and liquid-propelled rockets will likely remain propulsion methods of choice for large payloads and human spaceflight.

In recent years however, markets have emerged that require affordable means of transporting ultra-light or sensitive payloads to high altitudes/orbits and are willing to compromise on motor performance. Sounding rockets are specially developed to carry experimental instruments to a predetermined altitude, usually sub-orbital and parabolic in nature, which then record measurements during the flight. Hybrid rockets have been employed in this application because of their inherent safety factor, low transportation cost and quick turnover rate due to ease of manufacture. In November 2016 students at the University of Stuttgart launched a hybrid sounding rocket from the European Space and Sounding Rocket Range (ESRANGE) Space Centre to an apogee altitude of 32.3 km (Kobald et al., 2018).

Interest in space tourism, or space travel for recreational, business or leisure purposes, has also emerged in recent years. Virgin Galactic™, part of the Virgin™ Group, planned to be one of the first companies to offer suborbital spaceflights to paying customers (David, 2012). They use an air launched suborbital spaceplane designated SpaceShipTwo™. This is a low-aspect-ratio passenger aeroplane with a total capacity of eight people; two pilots and six passengers. SpaceShipTwo™ uses a 270 kN hydroxyl-terminated polybutadiene (HTPB) and nitrous oxide hybrid rocket motor designated RocketMotorTwo™ (Blau, 2013). The relative safety and low cost of manufacture of the rocket motor made this project viable.

There are various characteristics that distinguish hybrid rockets from their solid or liquid counterparts, as seen in Figure 1.1. Solid rocket motors consist of a propellant that contains all the chemical elements for complete burning, which are usually encased within the combustion chamber. The grain burns evenly over all exposed surfaces once ignited and the grain port gets larger until all the propellant is consumed. The hot combustion gases produced are then expelled out of a supersonic nozzle thereby producing thrust (Sutton and Biblarz, 2001).

Liquid rockets use two separated liquid propellants that are fed under pressure into a combustor which facilitates the combustion process and forces the resultant hot gases out of a supersonic nozzle to

produce the designed thrust. For larger, high-energy applications such as space launch vehicles the propellants are pump-fed into the combustor. This type of setup is usually very complex and requires many valves, turbines and pumps, sensors and filters (Sutton and Biblarz, 2001).

Hybrid rockets typically consist of one propellant in the solid phase, usually the fuel, and the other propellant in the liquid phase. The oxidiser is injected onto the pre-combustion chamber and then passes through the axial holes in the fuel grain combusting with the fuel vapour during the process. Hybrid rockets also use a post combustion chamber to ensure that all the gases have mixed properly and have burned to completion before exiting the nozzle. The oxidiser can be either cryogenic (such as liquid oxygen) or non-cryogenic. The oxidiser can be fed either by pressurization of the supply tank or by a pump.
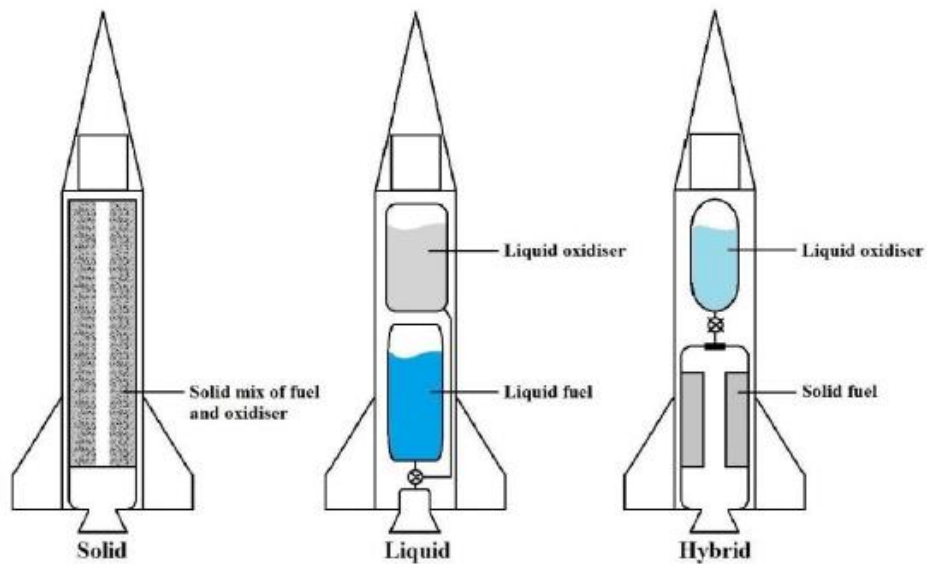
Figure 1.1: Comparison of different chemical rocket engines (Leverone, 2013)

Hybrid rockets are advantageous over their liquid and solid counterparts in a number of ways:

1. They are inherently safer than solid rockets since the fuel grain is inert and not in contact with the oxidiser
2. They are far simpler in operation and manufacture than liquid rockets and therefore are relatively inexpensive to make, and allow for fast redeployment
3. Since it is not required that the injector facilitates impingement of a liquid fuel and oxidiser, the injector is relatively simple and typically of the showerhead type
4. Like liquid rockets, hybrid rockets are throttleable with a comparatively large throttle turndown ratio

5. Fuel grain cracks in hybrid rockets are less destructive than in solid rocket motors because the oxidiser is only in contact with the fuel on the fuel grain surface of each port

There are also disadvantages associated with hybrid rockets that make them unsuitable or undesirable in certain applications, including the following:

1. Due to the increase of fuel grain surface area during the course of the burn, the oxidiser-to-fuel (O/F) ratio will vary and thereby affect the specific impulse
2. Hybrid rocket motors have lower density-specific impulse than solid rocket motors
3. Due to low regression rates, hybrid rockets do not perform as optimally as solid rocket motors. There are ways to counteract this such as adding more combustion ports but this directly affects the structural integrity of the grain.

Considering these factors, hybrid rockets have a role to play in niche applications. They can be used as sounding rockets due to their inherent safety and low cost, but have become particularly popular amongst academics and amateur rocket enthusiasts. Stanford University formed the Stanford Propulsion and Space Exploration Group, which launched numerous small-scale hybrid rockets and conducted a variety of experiments on hybrid rocket motors (Dyer et al., 2007). Delft University of Technology formed the Delft Aerospace Rocket Engineering (DARE) programme which saw the development of the Stratos II project, a hybrid vehicle using nitrous oxide as an oxidiser and a sorbitol/paraffin wax mixture with aluminium additives as the fuel (Knop et al., 2013).

Owing to their throttling capabilities, hybrids find use in tactical operations as a significant advantage may be derived through energy management and boost-and-sustain performance regimes. Hybrid rockets have been proposed for in-space applications due to throttling characteristics and stop-restart ability. This also makes hybrid rocket motors a potential candidate for providing the means of both velocity increment for acceleration-sensitive payloads as well as orbital insertion applications. Perhaps the most ideal application for the hybrid rocket motor is its potential use as a thrust augmentation vehicle. By making use of its throttling characteristics the exoatmospheric trajectory can be shaped for maximum performance and in addition, there remains the possibility of steering via differential control of each of the motor's thrust (Altman, 1991).

Following the Challenger Space Shuttle disaster in 1986, increasing safety concerns have led to proposals for using hybrid rocket motors as large launch boosters. In the early 1990s the largest hybrid engine was test fired by American Rocket Company (AMROC) and produced thrust in the 110 kN thrust class. More recently, in March 2017, NASA's Ames Research Centre successfully passed its final ground test of the Peregrine hybrid rocket motor using paraffin wax as a fuel and nitrous oxide as its oxidiser (Tabor, 2017). The aim was to design, develop and test a 100 km nitrous oxide-paraffin wax hybrid sounding rocket to demonstrate large-scale applications of hybrid technology involving liquefying fuels (Dyer et al., 2007)

1.2 HYBRID MOTOR THROTTLABILTY

Throttling hybrid rocket motors can be achieved by controlling the flowrate of the oxidiser into the chamber by means of adjustable valves placed before the oxidiser injector. Figure 1.2 shows the typical location of a valve in a hybrid rocket setup. When the flowrate of the oxidiser is varied, a shift in O/F ratio within the combustion chamber occurs and consequently the regression rate varies accordingly, which thereby produces a change in thrust. The thrust output is directly related to the chamber pressure which provides a reliable means of determining the motor's thrust in-flight allowing the on-board controller to adjust the control valve accordingly.
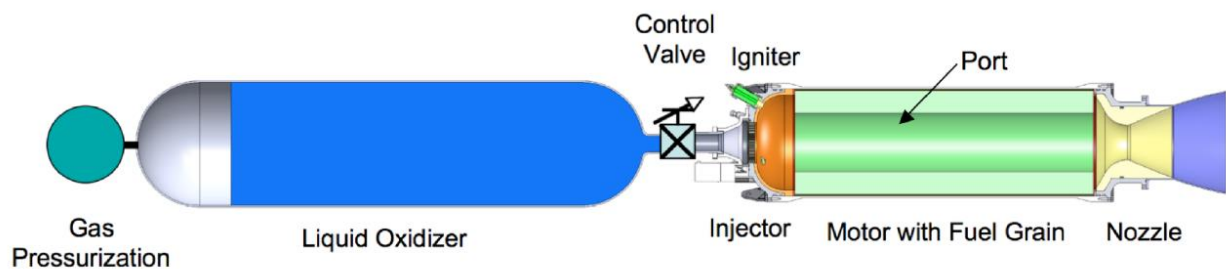
Figure 1.2: Schematic showing conceptual design of a hybrid rocket motor (Boiron and Cantwell, 2013)

With space exploration becoming increasingly popular in the long term plans of space programmes worldwide, there remains a market for motors that can accommodate soft landings on extra-terrestrial bodies. With performance characteristics like good safety, minimum environmental impact, responsiveness, reliability, lower life-cycle costs, soft ignition and shutdown, and a wide throttling range, hybrid rockets are suited to soft and precise planetary landings (Parissenti et al., 2011). Accurately throttling a hybrid engine is imperative in such an application.

Apart from throttling, the ability to shut down and restart a hybrid motor could be an attractive feature, particularly useful for micro and nanosatellite scale launch vehicles. This application also prefers low-g acceleration profiles for better optimized launch trajectories as well as protection of sensitive instruments in the launch vehicle payload. Developing robust control for hybrid motors remains a key priority for researchers, but devising and implementing such schemes necessarily requires an incremental approach, starting with experimentation at the laboratory scale.

1.3   STUDY AIMS

The aim of this study was to develop a versatile and robust controller for varying the thrust on a hybrid rocket motor according to a predetermined thrust profile. The specific aims comprise the following:

1. Develop a mathematical model of a laboratory-scale hybrid rocket motor
2. Use the model to determine the controller constants that best describe the desired response of the motor
3. Design and select hardware required to throttle the flowrate of oxidizer into the chamber
4. Perform open-loop hot-fire tests on the motor to obtain limits of throttlabilty
5. Demonstrate closed-loop thrust control on the laboratory scale motor

1.4   THESIS LAYOUT

In this thesis, Chapter 2 begins with a review of hybrid rocket theory and history of hybrid rocket motor development. It also provides a brief overview of the history of hybrid rocket motor throttling. Basic control theory and how it applies to the throttling of hybrid rocket motors is discussed, along with valve types and an appropriate actuator that are determined to be suitable for throttling.

Chapter 3 lays out the experimental setup of this study and shows how the experimental hardware interacts with the control software. It opens with a brief introduction to the Phoenix Hybrid Sounding Rocket Programme conducted by UKZN, and how the laboratory-scale tests are integral to the programme. The test facility at UKZN is then described as well as how the laboratory-scale motor is configured in the facility. A brief description of the motor itself is given followed by an explanation of the propellant delivery system operation. The LabVIEW™ control system, and how it integrates with the laboratory-scale rocket hardware, is also described at the end of the chapter.

A mathematical model of the laboratory-scale rocket motor is described in Chapter 4. The mathematical model simulates the motor response to various inputs and therefore allows accurate prediction of system behaviour when closed-loop feedback control is installed. The chapter describes the equations used for each control volume and all assumptions made, as well as how the control volumes interact within the MATLAB™ script in which they are written. A brief description is also given on how the script interacts with other software, such as NASA CEA™, to obtain the combustion dynamics and characteristics.

Chapter 5 details the control system regime and how it was developed. A method for obtaining an accurate transfer function for the controller is described. Complications regarding the non-linearity of the ball valve and how it affects the controller set-up are discussed as well as potential solutions. The chapter also gives an overview of the controller within the LabVIEW™ software and its integration with the other elements present in the laboratory-scale LabVIEW™ code.

Chapters 6 and 7 detail the results from the open-loop and closed-loop hot-fire tests respectively. In Chapter 6 the results from the open-loop tests show the approximate thrust produced at every valve

angle value as well as demonstrate the control authority of the valve. Chapter 7 provides results from the closed-loop tests and describes the fidelity and accuracy of the controller.

Chapter 8 summarises the study with concluding remarks in reference to the study aims, and identifies potential areas of application and improvement.

2   LITERATURE REVIEW

2.1   INTRODUCTION

The development of hybrid rockets dates back to the 1930s as a response to the hazardous nature of solid rockets using gunpowder as propellant. The first successfully launched hybrid rocket attained an apogee of 1.5 km under the Russian Gruppa Izucheniya Reaktivnogo Dvizheniya (GIRD) programme. The rocket used gelled gasoline suspended on a metal mesh and liquid oxygen (LOX) under its own pressure as oxidiser (Altman and Holzman, 2007)

During the same period, German engineer Hermann Oberth attempted to construct and test a LOX – graphite rocket but attained poor results due to the very high heat of sublimation of carbon and therefore poor combustion characteristics. Thereafter hybrid rockets were more seriously investigated with companies such as I.G. Farben testing a 10 kN rocket using coal as fuel and nitrous oxide as the oxidiser. However, the same problem persisted as the carbon in the coal yielded similar results to Oberth's LOX – graphite rocket.

Shortly after, in the 1940s, the Pacific Rocket Society used LOX and wood, more specifically Douglas Fir, to create a series of hybrid rockets designated as XDF - #. The company also experimented with various other base fuels such as wax loaded with carbon black and finally rubber. After many iterations the XDF – 23 was successfully launched in 1951 and reached an estimated altitude of approximately 30000 feet. This hybrid used LOX as oxidiser and rubber base fuel combined with an aluminium alloy nozzle (Altman, 1991).

In 1952 William Avery of the Applied Physics Laboratory began investigating a hybrid motor configuration classified today as a "reverse hybrid". It is termed this because it uses a liquid fuel and a solid oxidiser as opposed to the more common combination of solid fuel and liquid oxidiser. Avery selected jet propellant (JP) fuel and ammonium nitrate pressed into a cylinder with a circular port running axially through the grain as the oxidiser. These materials were selected for their availability and low cost, but did not perform well. Later in the mid-1960s reverse hybrids were further studied by Thiokol and United Technology Center using hydrazine based fuels and solid oxidisers such as ammonium perchlorate pressed into a non-reactive fluorocarbon binder (Altman, 1991).

During the 1960s the United States of America began active sponsorship of hybrid rocket programmes and investigations into hybrid rocket research. The United Technology Centre, funded by the US Navy, performed a series of experiments into the internal ballistics and fundamental characteristics of hybrid rocket combustion. These consisted of taking Schlieren photographs of Plexiglas burning in an oxygen atmosphere producing one of the very first hybrid combustion models. Using this model, along with droplet burning theory, a theoretical model was derived and improved on later by Spalding and Jain

(1959) at Imperial College London. The resultant equation for calculating the regression rate of the solid fuel was given as follows:

$$\dot{r} = \frac{a * G^n}{x^{0.2}} \qquad (2.1)$$

where $\dot{r}$ is the regression rate of the solid fuel during combustion, a is the constant accounting for viscosity, the Prandtl and Stanton numbers, and the velocity ratio at the edge of the boundary layer, G is the total mass flux at point x, and x is the axial distance through the solid grain from the end closest to the injector plate.

During the same period, the Office National d'Etudes et de Recherches Aérospatiales (ONERA) in France also began investigating hybrid combustion. Using diffusion boundary layer theory, they argued that there exists a laminar region for which the "n" exponent is 0.5, and a turbulent region where the exponent is equal to 0.8.

Very little additional research on hybrid rocket motors was done until the mid-1980s when demand for commercial satellites increased. Spurred on by the Space Shuttle Challenger and Titan III disasters, interest was renewed and hybrid rocket motor research restarted as a viable, safer alternative to solid rocket boosters (Altman, 1991). During this time, NASA began the Hybrid Propulsion Technology (HPT) programme which saw the design of a large scale 4448 kN motor, as well as a ¼ scale motor designed to be used in a cluster of four. These motors were evaluated using a large number of fuel-and-oxidiser combinations (Thiokol Corporation, 1989).

Recently, Karabeyoglu et al. (2002), have shown that paraffin-based fuels burn between three and four times faster than conventional rubber fuels. The enhancement in regression rate is attributed to a liquid layer that is formed on the surface of the paraffin wax during burning, which is hydro-dynamically unstable leading to droplet entrainment in the gas stream, as illustrated in Figure 2.1. This also has the effect of greatly reducing port grain complexity and manufacturing, requiring only a single port rather than a multi-port configuration.
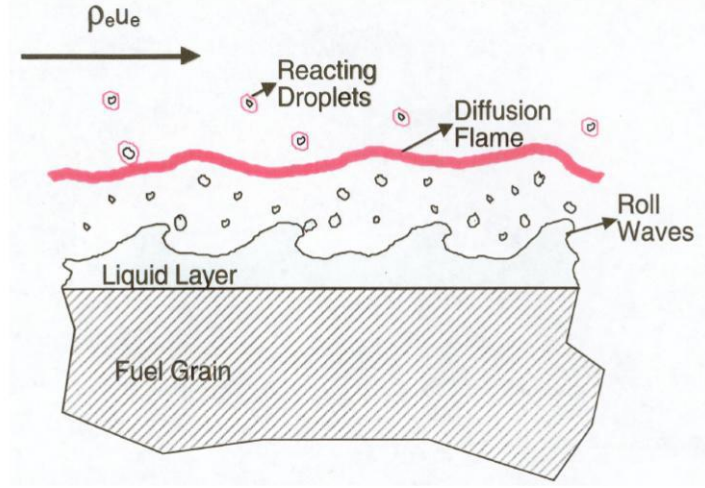
Figure 2.1: Non-classical mechanism of droplet entrainment in the gas stream (Karabeyoglu et al., 2001)

The non-classical regression rate is calculated as the sum of the evaporation regression rate $\dot{r}_v$ for the gasification mechanism and $\dot{r}_{ent}$ due to the mass transfer of the entrainment mechanism. The total regression rate is then given as:

$$\dot{r} = \dot{r}_v + \dot{r}_{ent} \tag{2.2}$$

Expanding this and taking an energy balance at the liquid-gas interface, the following correlation is obtained:

$$\dot{r}_v + \left[R_{he} + R_{hv} \left(\frac{\dot{r}_v}{\dot{r}_t} \right) \right] \dot{r}_{ent} = F_r \frac{0.03 \mu^{0.2}}{\rho_f} \left(1 + \frac{\dot{Q}_r}{\dot{Q}_c} \right) \beta \frac{C_H}{C_{HO}} G_t^{0.8} \frac{1}{x^{0.2}} \tag{2.3}$$

where R_{he} is the non-dimensional energy parameter for entrainment. Likewise, R_{hv} is the non-dimensional energy parameter for vaporisation, F_r is the roughness parameter, μ is the combustion gas viscosity, β is the blowing coefficient, $\dot{Q}_r$ is the radiative heat transfer, $\dot{Q}_c$ is the convective heat transfer, ρ_f is the density of the fuel, G_t is the total mass flux, C_H / C_{HO} is the blocking factor and x is the position along the longitudinal axis of the grain.

Other enhancements, like adding black dye to the grain to reduce radiative heat transfer, were also made during this period (Karabeyoglu, 2001).

2.2 OVERVIEW OF THROTTLING OF HYBRID ROCKET MOTORS

2.2.1 History of Throttling

The earliest instance of throttling hybrid rocket motors was recorded by Moore and Berman (1956). The vehicle used 90% hydrogen peroxide and polyethylene as the solid fuel however the motor was described as an augmented monopropellant motor due to the exceedingly high O/F ratio. Since this investigation was part of a US Army ordinance contract, most of the results were redacted save for the confirmation statement that hybrid rockets can be throttled using a single valve on the oxidiser feed line. During the 1960s ONERA in France developed a hybrid sounding rocket called Lithergol EXperimental (LEX). The rocket used a solenoid valve to throttle the thrust from a 10 kN peak down to 2 kN during flight. During the time period of 1964 to 1967, a total of eight LEX rockets were flown, all successfully (Duban, 1968).

During roughly the same period, the United States Air Force (USAF) developed a throttleable hybrid rocket programme for aerial target drones. Titled "*Sandpiper*", the programme employed MON-25 (75% nitrogen tetroxide and 25% nitric oxide) as an oxidiser and 10% magnesium and 90% polymethylmethacrylate as the solid fuel. The motor could achieve a peak thrust of 2.3 kN with an 8:1 turndown ratio (Franklin et al., 1969). A second programme for aerial drones developed by the USAF and built on the *Sandpiper* project was known as HAST, for High Altitude Supersonic Target. This motor was larger than the *Sandpiper* series with a 5.3 kN peak thrust. The motors used a pintle valve actuated by a torque motor, and allowed for a turndown ratio of 10:1 (Penn and Branigan, 1975).

Also during the 1960s the US United Technology Centre (UTC) developed several hybrid rocket programmes including a high performance hybrid motor for use in the upper stage of a launch vehicle (Sutton and Biblarz, 2001). This motor used a hypergolic mixture of a lithium based fuel and an oxygen difluoride (OF_2) oxidiser. The motor had a peak thrust output of 22.2 kN and could be throttled with an 8:1 turndown ratio. This motor was never used outside of ground testing due to the propellant toxicity. In another project by UTC, a pre-packaged hybrid rocket motor was developed for use in tactical missiles. For the oxidiser control system, this motor used a custom control system that included two solenoids to control two poppet valves on two separate distribution manifolds. The motor could be throttled to either 22.2 kN or 11.1 kN by switching between the manifolds. The motor could also be restarted a maximum of twice at either thrust level (Hamers, 1967).

The success of solid and liquid rocket systems during the 1970s and early 1980s, resulted in little significant hybrid motor research being performed in this period. However, as a result of the 1986 Space Shuttle Challenger disaster, as well as the increasing demand for commercial satellites, research into hybrid propulsion systems was restarted. During this time AMROC was formed and developed a number of hybrid motors of various sizes, using mostly hydroxyl-terminated polybutadiene (HTPB) as the fuel and either LOX or nitrous oxide as the oxidiser (Kniffen and McKinney, 1990). These motors

were typically throttled by modulating the flowrate through the use of valves to the gas driven turbo pumps used to pump the liquid oxidiser. One of the company's largest motors, the H-1500, had a peak thrust of 1112 kN designed for the company's *Aquilla* launch vehicle (Flittie et al., 1992).

More recently, in 1999, Lockheed Martin and NASA's Marshall Space Flight Centre collaborated with the intention of producing a large, single stage hybrid rocket motor to replace the two stage sounding rockets that were in use. These used HTPB mixed with aluminium as the fuel and LOX oxidiser. They had two branching oxidiser lines that could be turned on and off independently by ball valves to step-throttle the motor. The project ended in 2003 after a series of successful ground static tests (Arves et al., 2003).

Over the last decade, a number of academic institutions have begun research into hybrid motor technology. Stanford University, in collaboration with NASA Ames Research Centre, NASA Wallops, and the Space Propulsion Group (SPG) company, began the Peregrine Sounding Rocket Programme in an effort to flight-test a liquefying fuel hybrid to an altitude of 100 km (Dyer et al., 2007). In this collaboration, Stanford University developed a custom oxidiser throttling device for the Peregrine rocket (Doran et al., 2009), consisting of a plate mated to the injector face within the manifold. This rotates about the longitudinal axis of the injector and therefore restricts oxidiser flowrate through the injector. The plate rotates to a degree that can regulate the oxidiser flowrate between 50 and 100% of its nominal value.

2.2.2   Control Theory

In order to achieve a particular thrust profile, a certain control structure must be implemented. A proportional-integrative-derivative (PID) controller is a feedback loop control mechanism that is the most commonly used in industrial processes. Feedback loop controllers of this type operate by calculating the error between the desired set-point and the actual output of the system. The controller then adjusts the control/manipulated variable, that is fed to the input of the plant, a new error is calculated and the controller adjusts accordingly. PID controllers use a combination of proportional, integrative and derivative control to achieve a controlled arrival at a desired set point accurately and timeously as depicted in Figure 2.2.
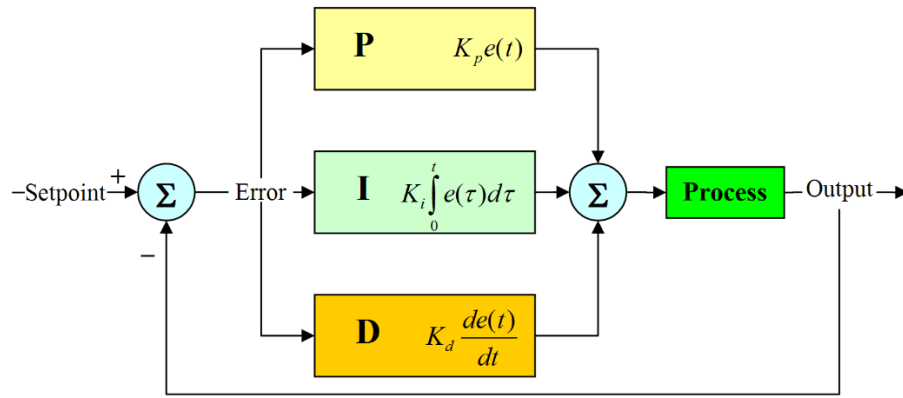
Figure 2.2: Closed-loop feedback diagram for a PID controller (Stienecker, 2011)

Proportional control adjusts the manipulated variable in proportion to the amount by which the actual output varies from the desired set-point (the error value). Although proportional-only controllers, so-called P controllers, are fairly common, they are not useful in more dynamic or transient systems since different levels of input are required for different situations. This is why the integral and derivative terms are important.

The integrative action of the controller measures two aspects: how large the error value is and how long the system has had an error value. The longer the system has an error value the larger the controller output will be. This is especially useful in dynamic plants where, as in the case of the laboratory-scale test stand employed here, numerous transients exist. It is possible to have an integral-only controller, however these are slow to react, as they rely on how long the system has been in error, and are prone to oscillations and overshoot. Integral controllers approach the set-point aggressively as long as they are in error.

The derivative term of the controller does not consider the error but rather the rate of change of error. For this reason, derivative-only controllers do not exist since they cannot bring the error to zero, only the rate of change of error. The derivative component's purpose is to flatten the error trajectory and in effect reduce or eliminate overshoot and oscillations. For the purpose of laboratory-scale testing and of rocketry in general, the controller should react quickly with little overshoot and a high degree of accuracy under constantly changing conditions.

PID controllers are used in a wide variety of systems. To make the PID control more responsive and effective, other methods are used in conjunction with the standard PID feedback loop to achieve the desired result. Some systems are nonlinear thereby making control of the output slow or oscillatory in nature. Other systems have a large time constant and can benefit from using cascade control – using two or more PID controllers in parallel to reach the desired set point faster. There also exist many systems where the actuators have a slow response (large dead-time) that must be accounted for.

Mathematically, it has been shown that the thrust output of hybrid rocket motors is directly proportional to the oxidiser flowrate, as discussed in Chapter 5. It can also be seen that a change in oxidiser flowrate rapidly changes the thrust output, meaning that there is a very small thermal and transport lag time. At a glance, it appears that no modification to the standard PID setup is required, since the system is responsive and the output changes in proportion to the change in oxidiser flow. However, the method of adjusting the oxidiser flow (the valve) typically does not have linear characteristics. Figure 2.3 shows the variation in valve flow coefficient, CV, versus the percentage the valve is open. Most valves, except for the plug valve and the globe valve, do not exhibit a linear valve flow coefficient and so are not preferable from a control system point of view. A primary drawback of the plug and globe valve is their slow opening and shutting times, making them unviable for use in transient applications where a quick and accurate response is required, as in this study.
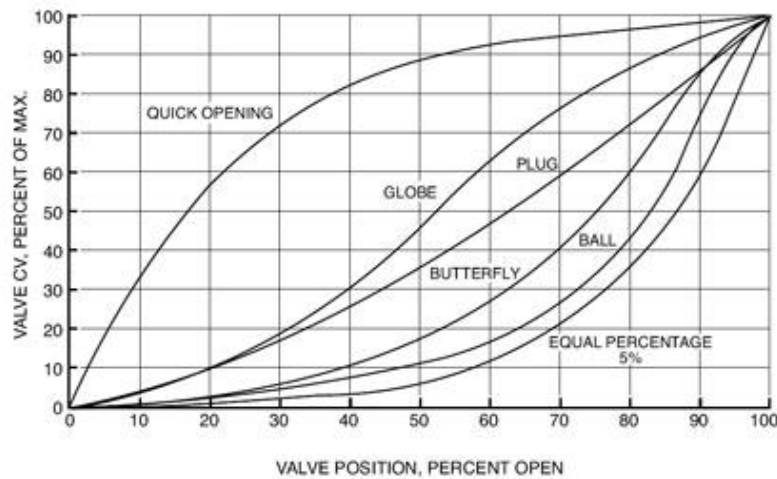
Figure 2.3: Varying flow coefficients for different types of valves (Pump & Systems, 2011)

2.3   FLOW CONTROL BY VALVES

In this study, the hybrid rocket motor test stand was to incorporate a valve that could be transferred directly to a flight vehicle to ensure that the vehicle performance is as predictable as possible. The valve was required to fit the design criteria of being both sufficiently light for optimal flight vehicle performance and robust enough to fully control the oxidiser flowrate in accordance with the thrust command profile.

A variety of failures regarding valves in the rocket engine industry have been observed, including unacceptable leakage due to fracture/wear/overstress on the sealing surfaces, excessive thermal contraction of critical parts due to cryogenic propellants, and attack of the seat by a propellant. In addition, failures to actuate have been noted due to differing thermal contractions, binding of shafts, contamination in close clearances, lubricant failure and poor alignment. Valve housings and shafts have failed due to vibrational loads, stress concentrations, low temperature brittleness, and inertial loads (National Aeronautics and Space Administration, 1973).

The valve and actuator in this study were therefore carefully selected to mitigate these common failures as much as possible. Factors considered included: valve housing material, valve seating material, type of valve, size of valve, shaft material and configuration, coupling connections, actuator type and strength, actuator configuration.

The valve/actuator assembly was selected to meet the following design criteria:

- Safe operation in sub-freezing temperatures
- Material compatibility with nitrous oxide
- Ability to throttle the oxidiser mass flowrate
- Fast translation between fully open and fully closed positions
- Ability to withstand a nominal pressure of approximately 65 bar
- Compact and light enough to be considered for a flight-weight component
- Easily configurable to an actuator without the need of specialist components

2.3.1 Valve Types

The most commonly used valves in liquid rocket systems are poppet valves, butterfly valves and ball valves as illustrated in Figure 2.4. Poppet valves are also frequently referred to as pintle valves and are most extensively used in throttling applications. Although there exist many more types of valves they were not considered for this application due to their inherent unsuitability (size, actuation time and so on).
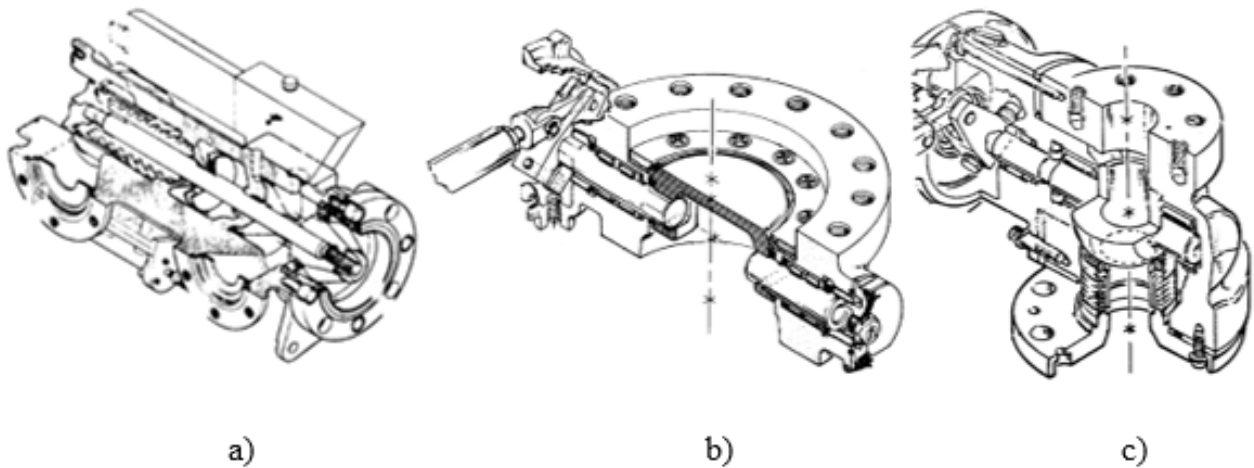
Figure 2.4: Cross-section views of a) pintle (poppet), b) butterfly, and c) ball valves respectively. Adapted from (National Aeronautics and Space Administration, 1973)

Various parameters must be considered when selecting a throttling valve, including cost effectiveness, availability, flight weight when combined with the chosen actuator, low pressure drop, material

compatibility, large range of control authority as well as a linear flow profile. Table 2.1 shows a summary of design criteria and how they relate to each valve type considered.

2.3.1.1 *Pintle Valves*

Pintle valves, also called poppet valves, match most of the aforementioned criteria especially those related to effective throttling of the hybrid motor. They allow for precise control and offer the greatest accuracy in throttling applications. Pintle valves also require relatively little actuation input to translate from the fully open to the fully closed position, which allows for almost immediate reaction from a control input. A serious disadvantage of poppet valves is their flow geometry, which causes an undesirably high pressure drop. In addition, the majority of pintle valves are designed for low flow applications, which is undesirable for the requirements of this study. Many liquid rocket motors still use pintle valves for throttling, however these are specially designed for the application and manufactured exclusively for that purpose.

2.3.1.2 *Butterfly valves*

Butterfly valves are used extensively for flow control of propellant in booster engines. Well designed and manufactured butterfly valves are reliable, have a low pressure drop and are easily controllable with an electric actuator. In addition, butterfly valves are compact and simply constructed, making them an attractive choice for flow control in rocket engines, especially for propellant flow control for liquid rocket engines. However, commercial butterfly valves are usually designed for control of gases or of liquids at low pressures due to ineffective sealing. In addition, the small sealing surface has been observed to warp under thermal load providing a leak passage for the propellant. Entities such as NASA and Lockheed Martin have bypassed these issues by designing and manufacturing their own specialized butterfly valves. Cost and time constraints mitigated against the manufacture of specialised butterfly or poppet valves in this study, with preference given to an off the shelf solution.

2.3.1.3 *Ball Valves*

Due to their reliability and robustness, ball valves are often used as safety valves. They have very high flow coefficients, are readily available and relatively inexpensive. They are also highly configurable, easy to clean and maintain, and require only 90° of rotation to open fully from the fully closed position. A drawback of ball valves for controllability purposes is their non-linear flow characteristic. There are commercial ball valve inserts that allow for linear flow characteristics but at a large expense with limited availability. Another concern with ball valves is their occasional sealing malfunction; oxidiser leakage in the Lunar Descent Module Engine (LMDE) was found to have been caused by a creased seal (Culick, 1996). The seal on a ball valve usually has a large contact area and a tight fit which thereby requires a large initial actuation torque. This is undesirable as it necessitates a larger actuator/gear assembly which adds weight to the flight vehicle.

Ultimately the ball valve was selected to be used for the flow control of oxidiser because of its low cost, availability and reliability.

Table 2.1: Summary of valve selection criteria

Valve Design Criteria Comparison			
	Ball Valve	**Poppet**	**Butterfly**
Cost	Cheapest option	Very expensive to design and manufacture	Very expensive to design and manufacture
Weight	Heavy	Usually light	Very light and compact
Availability	Readily Available	Must be made in-house for this application	Must be made in-house for this application
Material	Stainless steel/brass	Varies	Varies
Pressure drop	Very low	High	Low
Control linearity	Non-linear	Linear	Non-linear

2.3.2 Actuator Types

In a rocket motor throttling application, the valve actuator is required to:

- Have a sufficiently large torque to overcome the initial seal friction
- Enable precise control and positioning
- Be flight weight when coupled to the ball valve the actuator/valve assembly
- Perform repeatedly and reliably

In the present study, an electric actuator with pulse-width modulation (PWM) control was considered, however, most DC motors that are small enough to be considered flight weight do not have sufficient torque to reliably position the ball valve. Thus, other actuator types were considered, including hydraulic and pneumatic. Although hydraulic and pneumatic actuators are able to deliver the required torque, they are more difficult to integrate into a sounding rocket. Preliminary designs were considered in which chamber pressure is used to power a pneumatic/hydraulic type actuator but ultimately these designs were discarded due to their unnecessary complexity.

To ensure that there is sufficient torque, two DC electric servos configured with 3D printed ABS gears connected to the ball valve, as illustrated in Figure 2.5 were used. The servos are made by JX™ and designated as PDI-HV2060MG High Torque Servos for RC models. They are specified to turn a maximum of 180° and have just over 6 N-m of torque. They are meshed to the valve via a 2:1 gear ratio, enabling the valve to turn a maximum of 90° and exerting a theoretical 24 N-m on the valve at maximum voltage. This configuration is too heavy and large to fit on a flight weight vehicle but since this valve

is to be operated frequently unlike that of a sub-orbital sounding rocket, the laboratory-scale assembly, is used repeatedly and therefore the system was made as robust and reliable as possible. A ¾ inch ball valve in conjunction with a single servo motor of the same type has been fitted and tested on a previous sounding rocket (the Phoenix 1-B) and has shown positive results (Balmogim, 2017).
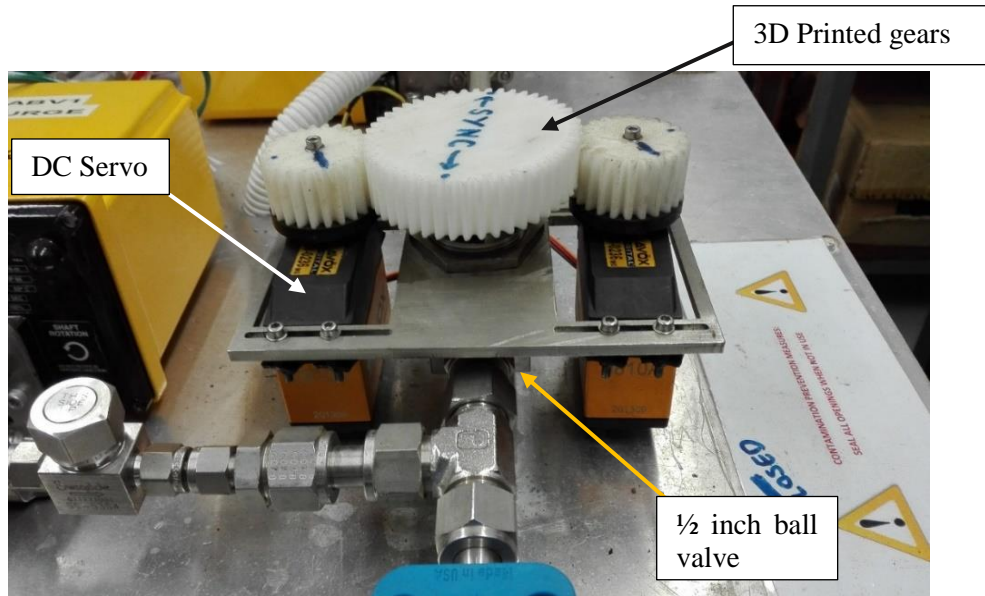
Figure 2.5: Two DC servo motors connected to the control valve via ABS plastic 3D printed gears on the laboratory-scale test stand

The valve angle is controlled by a PI controller, according to the difference in thrust commanded and thrust recorded. In this study, a series of open-loop tests were done to determine the precise numerical value of the valve angle in relation to the thrust produced. This allows for a higher degree of control and faster response time of the controller. Although it is not necessary, knowing the angle of the ball valve is also important for research purposes, making it easier to compare to Computational Fluid Dynamics (CFD) results and verify values determined in the lookup table. The final assembly consisted of two high torque DC servo motors operating in tandem to rotate a full-bore ½ inch ball valve. The servo motors had internal encoders making an external encoder unnecessary. The total cost of the valve assembly including the Swagelok™ stainless steel full-bore ball valve, the two servo motors, and the 3D printed ABS plastic gears was R 5150, considerably cheaper than a specialised throttling valve with linear flow characteristics.

3 EXPERIMENTAL SETUP

3.1 INTRODUCTION

In 2010 the UKZN Aerospace Systems Research Group (ASReG) established the Phoenix Hybrid Sounding Rocket Programme in an attempt to provide sounding rockets for the local scientific community (Brooks et al., 2010). The Phoenix programme requires that ground tests are first completed to verify performance and ensure safe operation before flight attempts are made. Owing to budget constraints and safety concerns, a laboratory-scale motor is first tested in a designated facility to ensure feasibility before designing and building a flight-scale motor. A laboratory-scale hybrid rocket test facility has been constructed at UKZN to enable safe testing with a quick turnover time allowing propulsion concepts to be evaluated. The facility was designed to provide a protective barrier in an event that catastrophic failure of the combustion chamber or nitrous oxide run-tank occurs.

3.2 LABORATORY-SCALE TEST FACILITY

Previously, laboratory-scale hybrid motor tests were undertaken at a temporary site adjacent to the Mechanical Engineering building on the UKZN campus. The test stand was wheeled in and bolted down to compacted concrete flooring.

As part of this project, a dedicated test facility was developed on the UKZN campus for the laboratory-scale test motor. The facility was constructed primarily so that in the event of an explosion or over-pressurisation event, the incident will be contained so as to prevent injury to persons or further damage to other equipment. Figure 3.1 shows the front and rear views of the new test facility prior to completion. A fireproof door was installed to provide access. The test facility is located adjacent to high banks that act as barriers in the event of a motor disintegration.

a)   b)

Figure 3.1: (a) Test facility prior to completion and (b) location of access to existing laboratories

A computer rendering of the facility can be seen in Figure 3.2. The facility was capped with a solid slab roof to contain a blast in the vertical direction. A primary objective in the design of the facility was to

separate the oxidiser feed components from the motor. This allows for better containment in the case of an explosion or overpressurization event and aims to mitigate the possibility of a chain reaction causing further damage. Figure 3.3 shows the current configuration of the oxidiser run-tank and nitrogen pressurant tank separate from the combustion chamber side of the facility. A water supply was provided for the water cooling of nozzles where necessary. Finally, a fire resistant door was fitted to provide access from within the building.
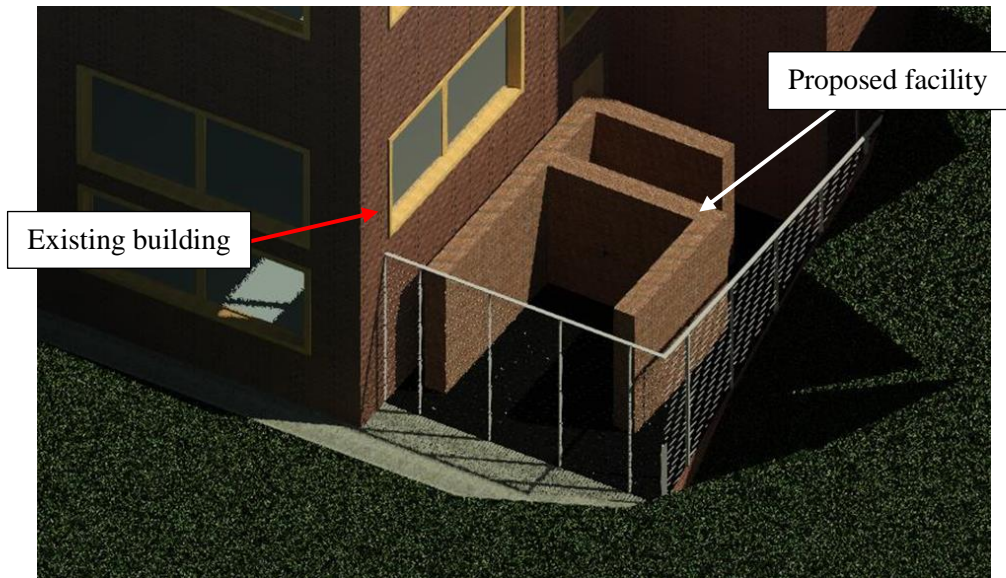
Figure 3.2: 3D rendering of hybrid rocket motor test facility with roof removed (Maritz, 2017)
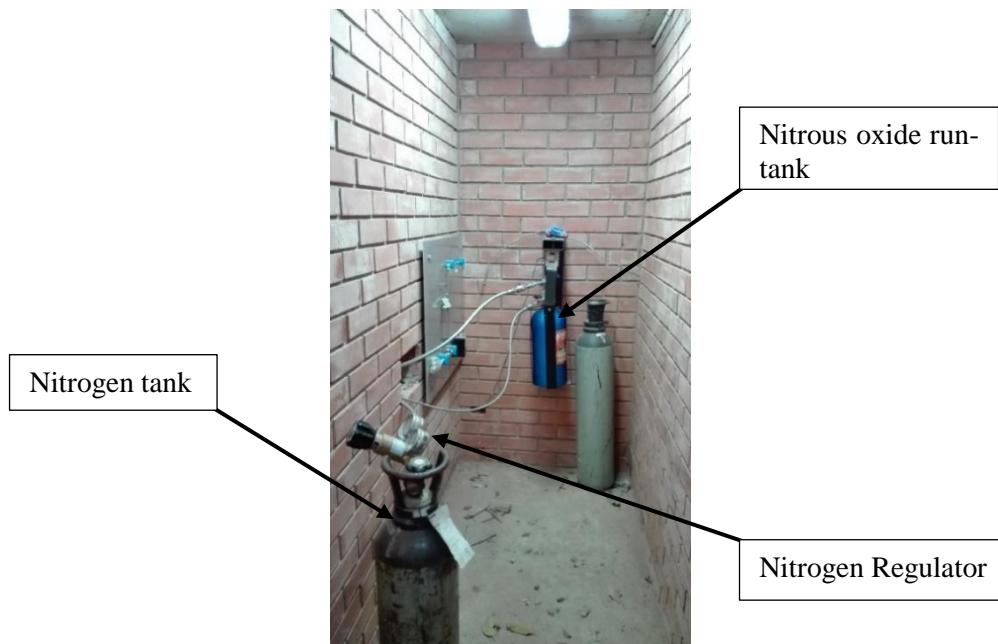
Figure 3.3: Oxidiser run-tank and nitrogen tank in oxidiser section of the facility

3.3 LABORATORY-SCALE HYBRID ROCKET MOTOR

The combustion chamber used in this study was the same used in a previous study by Maharaj (2018). The fuel grain cartridge slots into the main combustion chamber body with a flange on either side. The fore end flange contains the injector bulkhead and connects to the oxidiser feed system. The aft end flange retains the solid copper nozzle in the motor assembly. Figure 3.4 shows the assembly of the motor and Table 4.1 lists the components accordingly.

Table 3.1: Combustion chamber components (Maharaj, 2018)

Component	Description
1	Combustion chamber
2	Combustion chamber flange
3	Injector bulkhead flange
4	Nozzle retaining flange
5	Manifold support
6	Manifold
7	Injector
8	Nozzle
9	Capillary tube mounting point
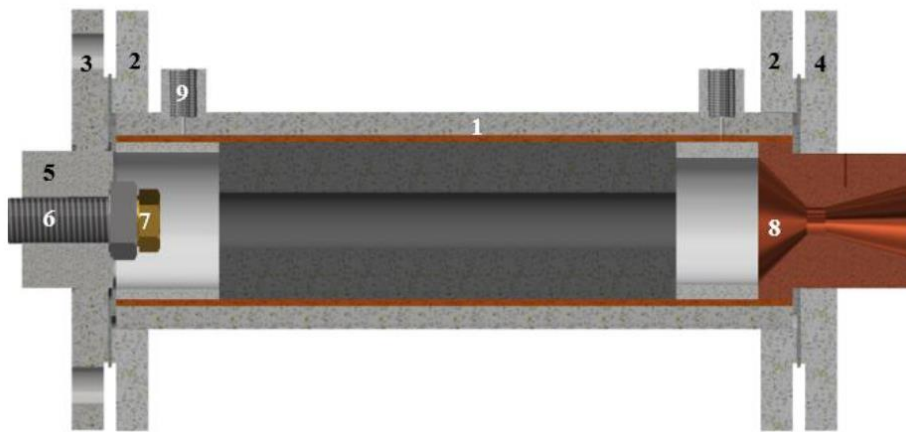
Figure 3.4: Combustion chamber cross-section with inserted fuel grain cartridge (Maharaj, 2018)

Figure 3.5 shows the combustion chamber and stand configuration in the motor firing side of the facility, and a hot fire test inside the newly built test facility.

Figure 3.5: (a) Laboratory-scale motor installed in test facility and (b) motor firing during a closed-loop test

The facility incorporates high definition cameras for live recording and observing the operation of the motor from a safe distance. Figure 3.6 shows the layout of the test control software panel and the camera screen. The cameras allow real-time monitoring of tests. This is essential to ensuring that proper ignition of the motor occurs, that the burn proceeds with stability and that no fire breaks out after conclusion of a test. In addition, the live footage is necessary to monitor the manipulation of the angle of the flow control valve and detect leaks in the nitrous oxide supply lines.
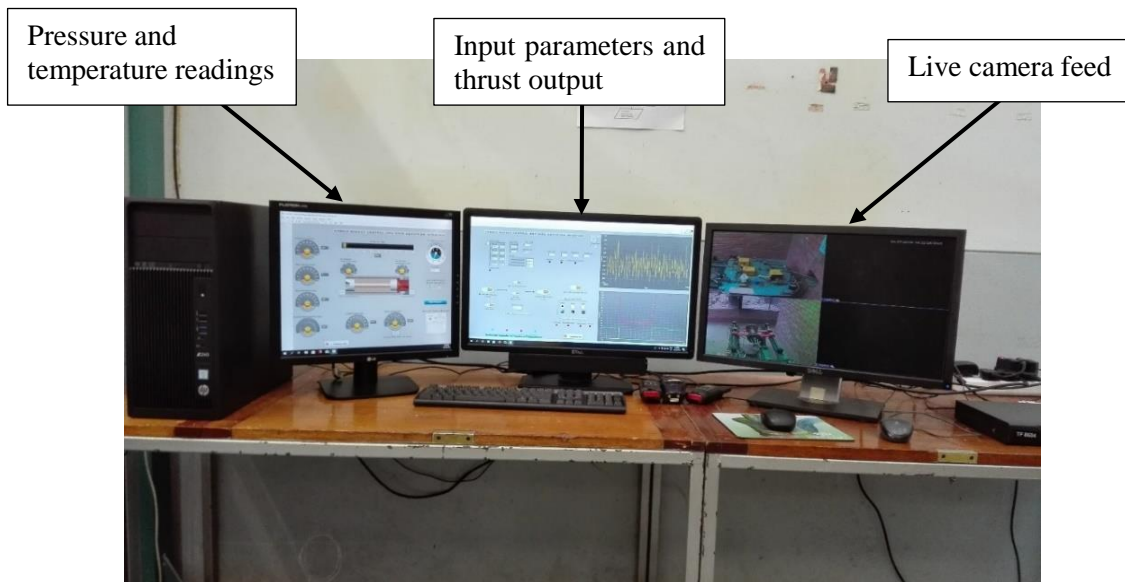
Figure 3.6: Hybrid rocket control panel and camera setup

3.4 PROPELLANT DELIVERY SYSTEM

In a hybrid rocket motor, the oxidiser mass flowrate is directly related to the total mass flux of the rocket and therefore the thrust output. It is imperative then to measure oxidiser mass flowrate during testing to create a predictable model of system behaviour.

The flow meter ought to measure the flowrate with high fidelity whilst allowing for very low amounts of pressure loss. An ultrasonic flowmeter was considered, specifically the Doppler shift type, which relies on the reflection of an ultrasonic beam of sonically reflective materials such as solid particles or entrained bubbles. However liquid N_2O does not typically contain particles nor does it always have bubbles in the flow.

A Coriolis-type meter was also considered. Coriolis meters make use of a vibrating tube through which the process fluid flows. As the oxidiser enters it is forced to accelerate as it advances toward the point of peak-amplitude vibration. This causes the tube to twist in relation to the mass flowrate, allowing for highly accurate flowrate measurement. However, these instruments typically have complex internal geometry creating an undesirably large pressure drop. These meters are also exceptionally expensive and were beyond the reach of this current study.

Another viable option was to make a cavitating venturi measurement device. A venturi for this specific application needs to be designed and manufactured, considering the physical properties of the fluid as well as the velocity and mass flowrate at nominal operating conditions. Using these properties, basic fluid flow calculations can be done to design a venturi best suited for this flow measurement application.

A simpler approach is the measurement of the weight of the oxidiser run-tank during the burn. With the application of a shielded load cell with a high sample rate, the weight of the run-tank was measured. Integrated LabVIEW™ software, continuously derived the mass with respect to time to display a real-time reading of the mass flowrate of the oxidiser. The principal problem with employing this method is the large amount of noise transmitted by the motor to the load cell. For this reason, the load cell measurements were filtered and additional post-processing was done. In addition, to further reduce signal noise, the run-tank was suspended and isolated from the stand as much as possible. Figure 3.7 shows the comparison of unfiltered tank weight read during the test, shown in red, and the filtered tank weight, shown in black, superimposed. An average between the two amplitudes of the filtered tank weight was taken to form a uniform, continuous line from which a mass flowrate of oxidiser could be derived.
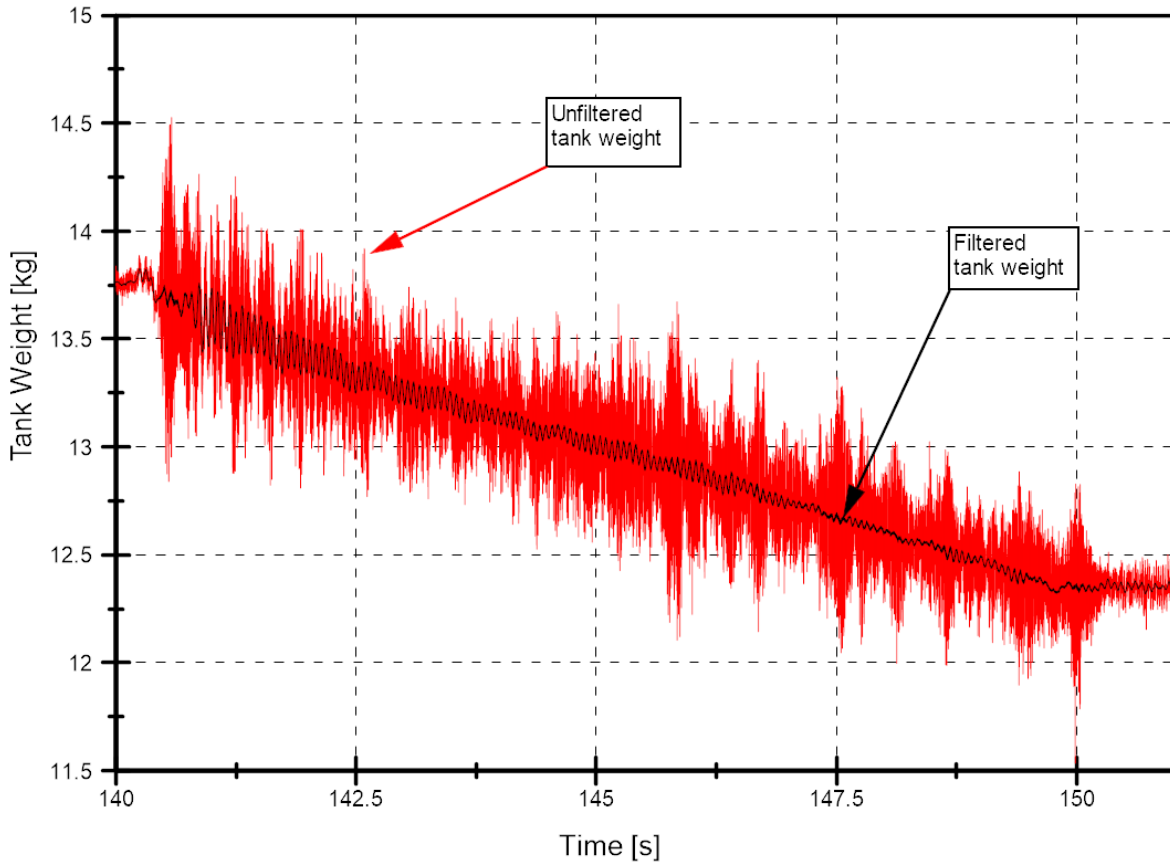
Figure 3.7: Filtered run-tank weight superimposed on unfiltered run-tank weight

The oxidiser feed system setup emulated that used by Genevieve (2013) with minor modifications. A schematic is given in Figure 3.8. The nitrous oxide run-tank is connected by a stainless steel braided hose, through a port in the separating wall to the Enable Oxidiser Flow Valve (ABV3), and then to the Control Valve (CV1) and finally to the injector coupled to the motor. Also connected to this feedline is a dump valve (SV1), a temperature sensor (T1), and two pressure sensors (P3 and P4). Parallel to the nitrous oxide feed system are the nitrogen supercharge and purge lines. The nitrogen tank is connected to two manual valves (a fine-adjustment needle valve NV1 and a manual ball valve MV1). After this the quarter-inch pipe splits in two, with one being used to purge the combustion chamber after hot fire testing and the other line connected to the run-tank. The purge valve (ABV1) can only be opened and permit flow through it when ABV3 is closed, to prevent the run-tank being flooded with nitrogen. Valve ABV2 controls flow to supercharge the run-tank which entails using nitrogen to pressurise the ullage section of the run-tank to 65 bar. Once opened, a solenoid valve (SV1) is manually opened and closed until the run-tank is at the desired supercharge pressure.
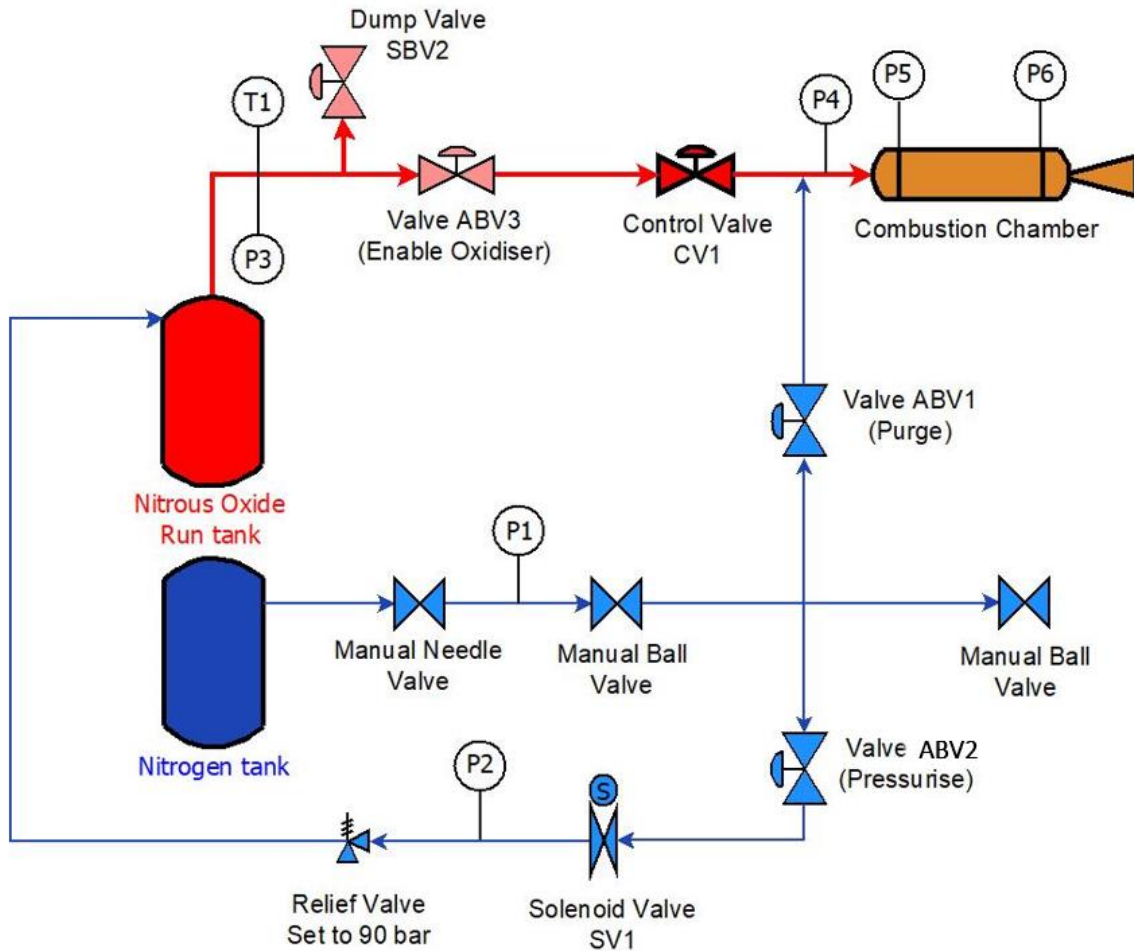
Figure 3.8: Schematic of oxidiser feed system.

Prior to the test, the oxidiser run-tank and the nitrogen tank are connected via Swagelok QuikConnect™ fitting. The nitrogen tank is fitted with a high pressure regulator valve which is set to deliver a pressure of 65 bar. The run-tank is then opened whilst pressure and temperature are monitored closely.

3.5   LABVIEW™ CONTROL SYSTEM

The LabVIEW™ program contains restrictions that will not allow the test to run if the pressure at P3 is higher than 70 bar and the temperature at T1 is greater than 40° C. Once all safety checks have been passed, the range is confirmed to be clear before supercharging the run-tank. The manual valves are opened and from that point in time no person is permitted to enter the testing area. The LabVIEW™ program then commands the servo valve ABV2 to open allowing nitrogen to pressurise the supercharge pipe. The actual supercharging takes places by opening the solenoid valve SV1 periodically for a few seconds until the pressure reading of P3 is at 60 bar. After some time has passed and the tank has cooled down, the tank is pressurised again back to 60 bar.

Once supercharging is complete, valve ABV2 is closed to completely isolate the nitrogen tank from the run-tank. Following this, valve ABV3 is opened, allowing all pressure from the run-tank to rest on the control servo valve CV1. The auto-sequence is initiated and from that point on, the user has no further control over the feed system save to shut it off. The ignitor burns for three seconds followed by the control servo CV1 opening to allow oxidiser into the combustion chamber. During the burn, only the servo valve CV1 is manipulated by the PID controller, and thrust data is recorded as well as the pressures inside the combustion chamber from P5 and P6. At the end of the burn sequence, the servo valve shuts as well as the control valve CV3. After one second's delay, control valve CV1 opens to allow nitrogen into the combustion chamber to purge any flame or hot particles therein. This process lasts three seconds total. In the event of pressure and/or temperature measurements exceeding safety limits, all oxidiser feed valves will shut and servo valve SBV2 will open, dumping the entire nitrous oxide run-tank to atmosphere. Figure 3.9 shows the current system in place.
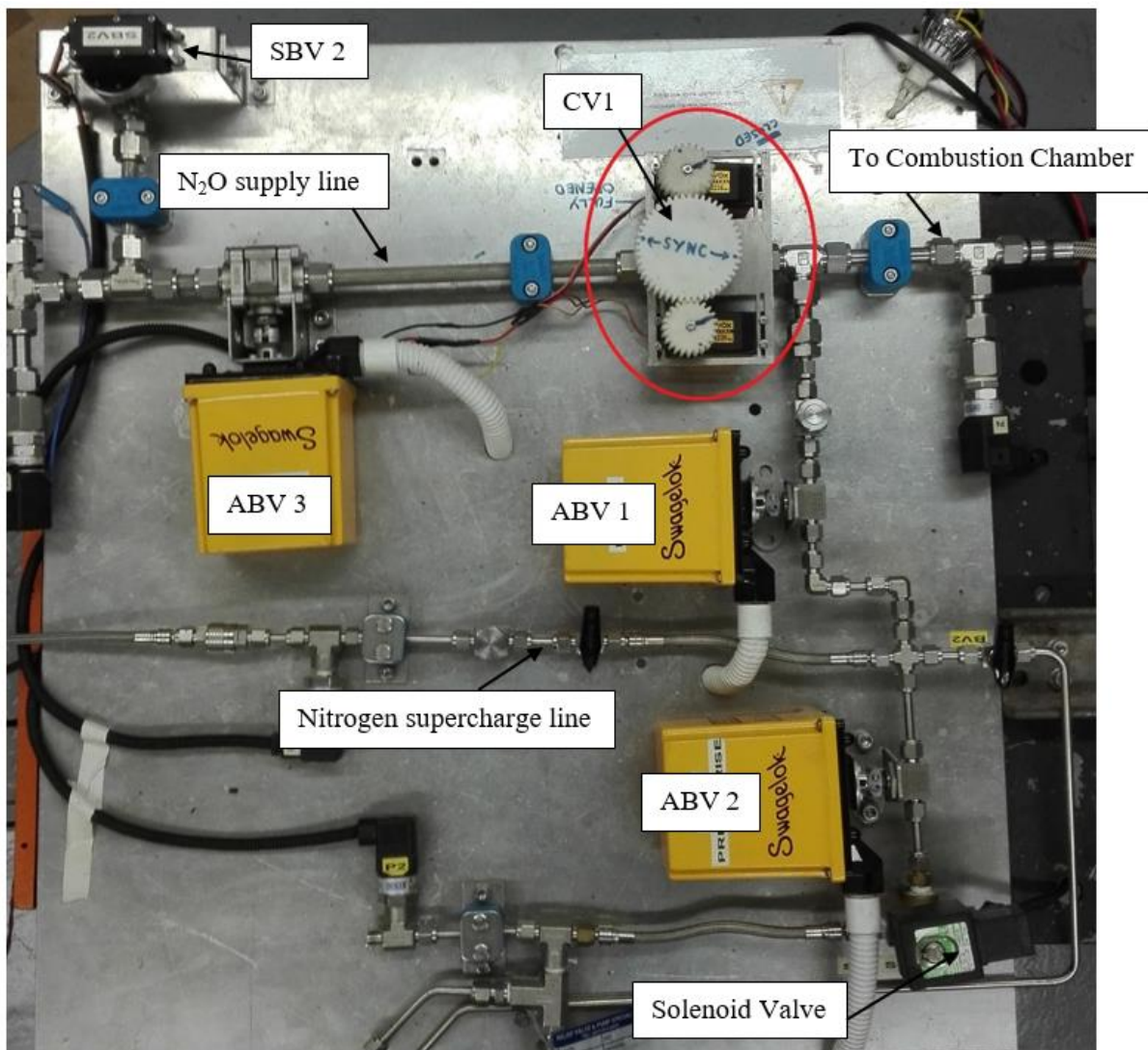
Figure 3.9: Oxidiser feed system with control valve meshed to the servos shown within the red oval

3.6 CONCLUSION

A physical test stand was set up in a new test facility to ensure a safe operation of the laboratory-scale hybrid rocket motor. The test-stand configuration and operation are described. The facility was built with two sections, one for the test stand and another section with the oxidiser run-tank and nitrogen supercharge tank. The test stand is connected to the tanks via a port in the wall. The facility is also fitted with live-feed cameras for observation during tests, and with high-definition cameras used for recording and post-processing of data. A method was devised to obtain the oxidiser mass flowrate by measuring the mass of the run-tank using a sensitive load-cell and digital filters.

4   SYSTEM SIMULATION

4.1   INTRODUCTION

The hybrid rocket laboratory-scale setup was simulated in MATLAB™ to predetermine viable parameters for the implemented control regimen. This allowed a set of parameters to be tested repeatedly under various control inputs to predict the outcome of the control scheme, and hence select the most robust values to install as the control set. Various programs and applications were used to numerically simulate the laboratory-scale set-up which will be discussed in detail and reviewed further in this study. The model was designed such that, if need be, it can be scaled up and used on larger flight-weight motors with minor modification to the code.

The model utilises MATLAB™ code to describe physical phenomena during the emptying of the tank, filling of the feed system pipes, oxidiser injection process, and expulsion of combustion gas through the nozzle. The NASA CEA™ application is used to perform combustion calculations using the laboratory-scale chamber geometry and results are recorded for various O/F ratios and posted to a Microsoft Excel™ spreadsheet. The MATLAB™ code then employs a lookup table for the relevant values and delivers these to the regression rate model to compute the total mass flowrate of both oxidiser and fuel. Finally, these values are input into the nozzle calculations section for the code where the laboratory-scale thrust is predicted. The entire numerical simulation is contained within a single MALAB™ script which itself contains various sections for different areas of modelling. The first sections of the code are used to store initial conditions and fixed constants like material properties, the next section creates an empty array to store values from the nested FOR loop, the following section is a single FOR loop that is run using a Runge-Kutta time marching scheme and the final section processes the calculated values by plotting graphs.

The MATLAB™ code is designed and written to be run inside of a simulation loop in LabVIEW™ from which predictions can be made regarding the output thrust of the motor for a given control scheme. For this to run successfully, the MATLAB™ script must be as robust and as simple as possible while not compromising the overall accuracy of the model.

The numerical model was divided into six control volumes which are connected by the relevant variables. Figure 4.1 shows the schematic of the overall simulation work flow.
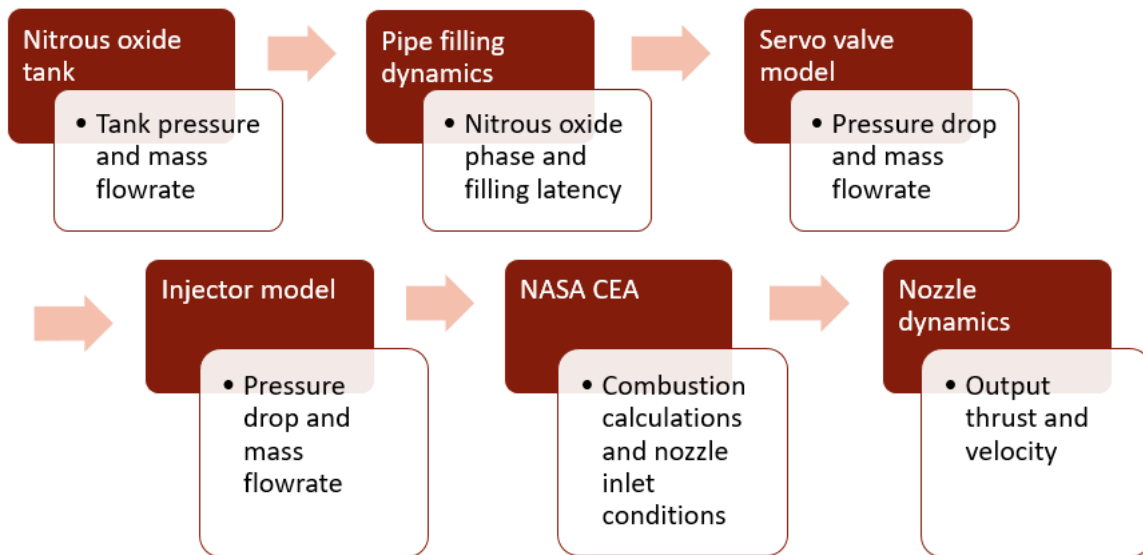
Figure 4.1: Simulation workflow and control volumes of the laboratory-scale hybrid rocket motor model

4.2   TANK PRESSURISATION AND EMPTYING

The run-tank contains liquid nitrous oxide which is volatile at room temperature and therefore self-pressurising. For safety and to achieve higher pressures, the run-tank is supercharged with an insoluble inert gas, in this case nitrogen, and is discharged with the nitrous oxide upon the end of the test. As the nitrous oxide depletes in the tank, the thermodynamic properties change. There is a loss of internal energy due to the draining of the nitrous oxide, and as the nitrous oxide evaporates to equilibrate the system, the total thermal energy of the system decreases accordingly. This all results in a decrease in vaporisation pressure which subsequently translates to a lower tank pressure. Modelling these changes to predict the oxidiser flowrate and therefore the thrust of the system is critical for determining the correct control parameters. The general assumptions made are as follows:

1. The walls of the nitrous oxide tank are in thermal equilibrium with tank contents
2. The walls of the tank are adiabatic to the external environment
3. The effects of gravity are ignored
4. The tank contents are assumed to be in phase equilibrium for all instances of the draining process i.e. the temperature and pressure are uniform at all times
5. The ideal gas law is obeyed
6. Friction losses within the tank are ignored
7. Only liquid is drained and that after the test there is still liquid remaining in the tank

The following model has been adapted from Fernandez (2009) with modifications regarding pressurisation species and delivery calculations. Differential equations derived from conservation of mass and energy are used to calculate tank temperature and pressure, as well as the number of moles of

liquid and vapour nitrous oxide in the tank. Figure 4.2 illustrates the control volume used for the modelling of the blow-down process.
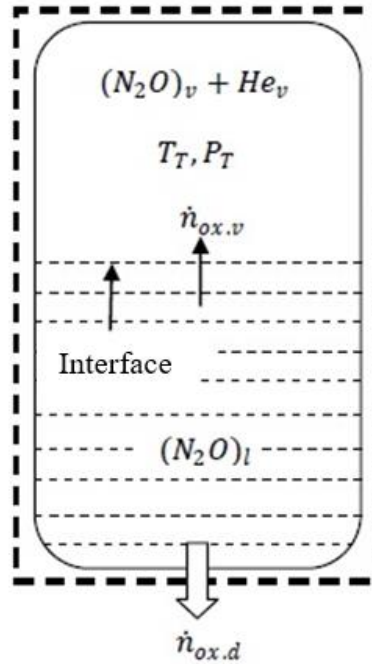
Figure 4.2: Tank blow-down process (Genevieve, 2013)

Using conservation of mass, the change in number of moles is given by:

$$\frac{d}{dt}\left(n_{ox,l} + n_{ox,g}\right) = -\dot{n}_{ox,o} \qquad (4.1)$$

where $n_{ox,g}$ is the number of moles of gaseous nitrous oxide while $n_{ox,l}$ is the number of moles of liquid nitrous oxide, and $\dot{n}_{ox,o}$ is the nitrous oxide going out the tank. The change in number of moles of gaseous and liquid nitrous oxide is therefore equivalent to $\dot{n}_{ox,o}$, which is the amount of moles of liquid nitrous oxide leaving the tank. The mass flowrate of liquid nitrous oxide, $\dot{m}_{ox,l}$, passing through an orifice can be calculated as:

$$\dot{m}_{ox,l} = C_d N_{inj} A_{inj} \sqrt{2\rho_{ox,l}(P_T - P_{losses} - P_c)} \qquad (4.2)$$

Using Equation (4.2), the rate at which liquid nitrous oxide moles leave the tank can be calculated as:

$$\dot{n}_{ox,l} = C_d N_{inj} A_{inj} \sqrt{\frac{2(P_T - P_{losses} - P_c)}{(MW)_{ox}\bar{V}_{ox,l}}} \tag{4.3}$$

Here, C_d is the discharge coefficient, N_{inj} is the number of holes in the injector, A_{inj} is the cross-sectional area of each hole in the orifice, P_T is the tank pressure, P_{losses} represents the pressure drop across the feed system and injector, and P_c is the chamber pressure. In Equation (4.2), $(MW)_{ox}$ is the molecular weight of nitrous oxide and $\bar{V}_{ox,l}$ is the molecular volume of liquid nitrous oxide. The rate of moles leaving the system can then be calculated by Equations (4.3) and (4.2):

$$\frac{d}{dt}(n_{ox,g} + n_{ox,l}) = -C_d N_{inj} A_{inj} \sqrt{\frac{2(P_T - P_{losses} - P_c)}{(MW)_{ox}\bar{V}_{ox,l}}} \tag{4.4}$$

The total internal volume of the tank, V_T , can be calculated by summing the internal liquid volume, V_l, and the internal gaseous volume, represented by V_g. The gaseous volume consists of two species, namely gaseous nitrogen and nitrous oxide vapour. This can be described as:

$$V_T = V_g + n_{ox,l}\bar{V}_{ox,l} \tag{4.5}$$

Applying the perfect gas law to the tank yields:

$$P_T V_g = n_g R T_T \tag{4.6}$$

Using Raoult's law the following relation is obtained:

$$P_T = \frac{P_{ox}^*|_{T_T}}{\left[\dfrac{n_{ox,v}}{n_{ox,v} + n_{sp,v}}\right]} \tag{4.7}$$

where P_{ox}^* is the saturated vapour pressure of nitrous oxide and is a function of tank pressure and mole fraction. Substituting Equation (4.7) into Equation (4.6) obtains:

$$P_{n2o}^* V_g = n_{n2o,v} R_u T_T \tag{4.8}$$

This equation relates the saturated vapour pressure with the number of moles of nitrous oxide in the run-tank, the total volume of gas inside the tank, and the tank temperature. Substituting Equation (4.8) into Equation (4.5) and differentiating with respect to time yields:

$$
\begin{aligned}
-\bar{V}_{ox,l} P_{ox}^* \frac{dn_{ox,l}}{dt} + \left[\left(V_T - n_{ox,l}\bar{V}_{ox,l} \right) \frac{dP_{ox}^*}{dT} - n_{ox,l} P_{ox}^* \frac{d\bar{V}_{ox,l}}{dT} \right] \frac{dT_T}{dt} \\
= R_u \left[n_{ox,v} \frac{dT_T}{dt} + T_T \frac{dn_{ox,v}}{dt} \right]
\end{aligned}
\tag{4.9}
$$

Assuming no boundary work being done on the system, and no heat exchange to the environment, the following relation can be made:

$$\frac{d}{dt}\left(m_T u_T + n_{ox,l}\bar{U}_{ox,l} + n_g \bar{U}_g \right) = -\dot{n}_{ox,o}\bar{H}_{ox,l} \tag{4.10}$$

where m_T is the mass of the tank and u_T is the specific internal energy of the tank. $\bar{U}_{ox,l}$ is the internal energy of the liquid phase of nitrous oxide and $\bar{U}_g$ is the internal energy of the gas phase of nitrous oxide. Finally, $\bar{H}_{ox,l}$ represents the molar enthalpy of liquid nitrous oxide. Expanding this, one obtains:

$$
\begin{aligned}
m_T \frac{du_T}{dt} + n_{ox,l} \frac{d\bar{U}_{ox,l}}{dt} + n_{ox,v} \frac{d\bar{U}_{ox,v}}{dt} + n_{sp,v} \frac{d\bar{U}_{sp,v}}{dt} \\
= \frac{dn_{ox,v}}{dt}\left(\bar{H}_{ox,l} - \bar{U}_{ox,v} \right) + \frac{dn_{ox,l}}{dt}\left(\bar{H}_{ox,l} - \bar{U}_{ox,l} \right)
\end{aligned}
\tag{4.11}
$$

The difference between liquid and vapour phase enthalpies is the heat of vaporisation and defined as $\Delta\bar{H}_{ox,v} = \bar{H}_{ox,v} - \bar{H}_{ox,l}$. Additionally, the enthalpy of the vapour phase can be defined as $\bar{H}_{ox,v} = \bar{U}_{ox,v} + P_T\bar{V}_{ox,v}$. Substituting this into Equation (4.11):

$$m_T \frac{du_T}{dt} + n_{ox,l} \frac{d\bar{U}_{ox,l}}{dt} + n_{ox,v} \frac{d\bar{U}_{ox,v}}{dt} + n_{sp,v} \frac{d\bar{U}_{sp,v}}{dt}$$
$$= \frac{dn_{ox,v}}{dt}\left(R_u T_T - \Delta\bar{H}_{ox,v}\right) + \frac{dn_{ox,l}}{dt}\left(P_T \bar{V}_{ox,l}\right) \tag{4.12}$$

The rate of change of molar internal energy of the vapour phase is calculated as $\frac{d\bar{U}_{ox,v}}{dt} = \bar{C}_{V_{ox,v}} \frac{dT_T}{dt}$. The rate of change of liquid nitrous oxide internal energy can likewise be calculated as $\frac{d\bar{U}_{ox,l}}{dt} = \bar{C}_{V_{ox,l}} \frac{dT_T}{dt} \approx \bar{C}_{P_{ox,l}} \frac{dT_T}{dt}$. The rate of change of specific internal energy of the run-tank can also be approximated as $\frac{du_T}{dt} \approx \frac{dH_T}{dt} = C_{P_T} \frac{dT_T}{dt}$. Substituting these equations into Equation (4.12) yields:

$$\left(m_T c_{P_T} + n_{ox,l}\bar{C}_{P_{ox,l}} + n_{ox,v}\bar{C}_{V_{ox,v}} + n_{sp,v}\bar{C}_{V_{sp,v}}\right)\frac{dT_T}{dt}$$
$$= \frac{dn_{ox,v}}{dt}\left(R_u T_T - \Delta\bar{H}_{ox,v}\right) + \frac{dn_{ox,l}}{dt}\left(P_T \bar{V}_{ox,l}\right) \tag{4.13}$$

There are therefore three unknown time derivatives namely tank pressure, $\frac{dT_T}{dt}$, number of moles in the nitrous oxide vapour phase, $\frac{dn_{ox,v}}{dt}$, and number of moles in the nitrous oxide liquid phase, $\frac{dn_{ox,l}}{dt}$. These terms are solved simultaneously using a Runge-Kutta numerical time marching scheme, described by Genevieve (2013). The tank pressure is finally calculated by:

$$P_T = \frac{\left(n_{ox,v} + n_{sp,v}\right)R_u T_T}{V_T - n_{ox,l}\bar{V}_{ox,l}} \tag{4.14}$$

4.3 OXIDISER MASS FLOWRATE THROUGH THE VALVE

Modelling nitrous oxide flow through a ball valve presents difficulties due to the complicated mathematics associated with two-phase flow and numerous assumptions that would yield inaccurate results. To approximate the mass flowrate of the oxidiser through the ball valve, a CFD analysis was performed for nitrous oxide flow at selected angles of the valve. The parameters such as the inlet and outlet pressures as well as the temperatures were chosen based on data from previous tests. The results were then extrapolated and used in the simulator to predict oxidiser mass flowrate at each valve angle. Using the value for oxidiser mass flowrate, the net thrust of the motor can be determined. This provides a direct link to the valve angle and the thrust produced.

The valve was measured and drawn in a 3D modelling package and the interior volume at different valve angles was exported to STAR CCM+. Valve angles were chosen based on previous laboratory-scale tests and correspond to the upper and lower limits of controllability, as well as an intermediate valve position. From this data, mass flowrates and thrust values could be mapped to all possible valve angles.

It was determined that the smallest valve angle that provided sufficient oxidiser was 44.5° while the largest angle that will still provide control over the thrust output of the motor was set at 65.5°. Between the angles of 65.5° and 90° no change over the mass flowrate of nitrous oxide will occur. An additional, intermediate angle of 51.5° was chosen to more accurately interpolate predicted flowrates between 44.5° and 65.5°.

Valve Angle at 44.5°

All parameters of this simulation, such as the stagnation pressure before the valve and the pressure just after the valve, were obtained from test data pertaining to the approximate moment in time the valve was set at 44.5° in the open-loop tests. In addition, the oxidiser mass flowrate value obtained from these simulations was compared to the measured mass flowrate of the open-loop tests to ensure the simulation results were accurate.

<u>Simulation Setup</u>

Besides the parameters obtained from test data, mesh size and type were selected using general practice norms and adjusted to provide accurate results without wasting computational resources. The imported geometry is shown in Figure 4.3, and a detailed view of the completed mesh is shown in Figure 4.4. The wall y^+ values were also calculated using flat plate boundary layer theory to coincide with engineering best practices to accurately capture the flow field near the wall. The nitrous oxide properties were obtained from the NIST database (NIST Standard Reference Database 23, 2007). Initially, the inlet of the flow domain was set to be fully liquid and the outlet as fully gaseous, this allows for faster convergence. Table 4.1 shows a summary of parameters used in the simulation.

Table 4.1: Summary of primary simulation parameters

Mesh type	Polyhedral combined with prism layer meshing
Mesh size	0.4 mm base size and 0.1 mm at refinement area
Prism layer total thickness	0.03776 mm
Inlet stagnation pressure	60 bar
Outlet pressure	28 bar
Initial volume fraction	Fully liquid at inlet and fully gaseous at outlet
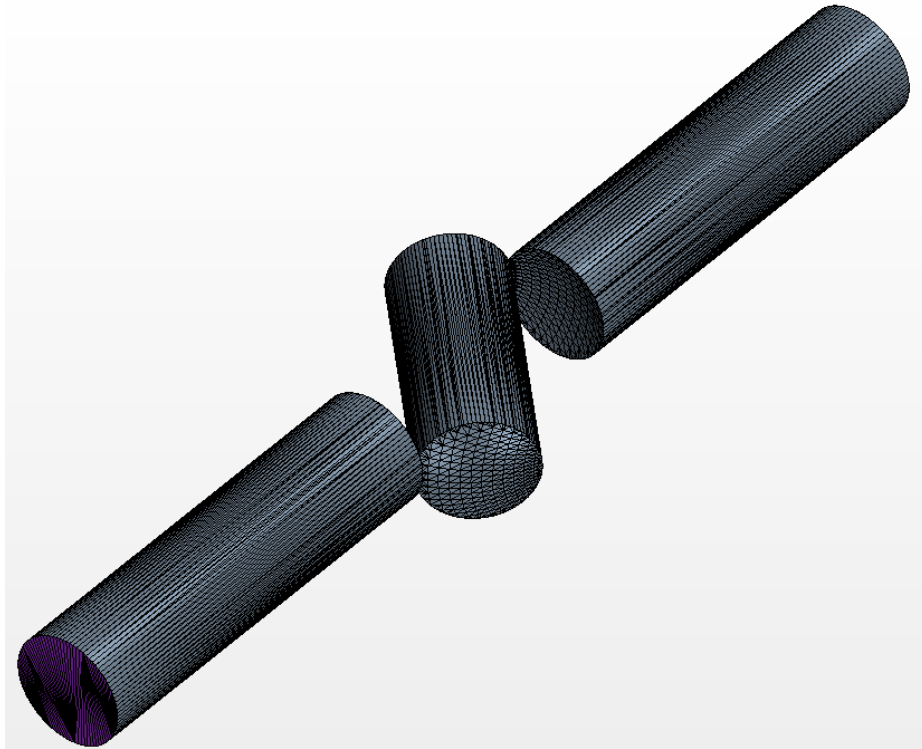
Figure 4.3: Imported geometry of the flow domain
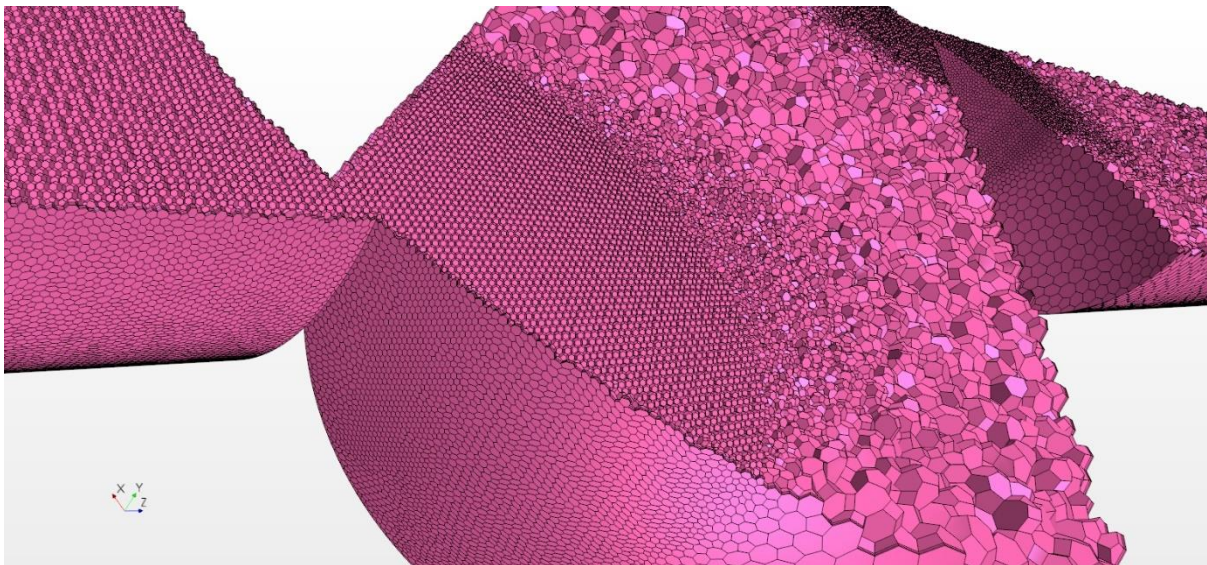
Figure 4.4: View of mesh size and refinement for 44.5° flow simulation

The valve and its components were measured and drawn in a 3D-CAD package such that the valve was at 44.5° from the fully open position. The internal geometry was exported to STAR-CCM+ and prepared for meshing. A polyhedral mesher combined with prism layer meshing was used as well as mesh refinement for areas where greater flow vortices and eddies can occur, such as the transition into the

angled ball, as illustrated in Figure 4.9. It was determined that the geometry did not extend far enough past the ball to adequately simulate flow effects and therefore the extruder mesher was added at the outlet. Initially the mesh was relatively large and the physics were relaxed to allow for initial convergence. There after the mesh was set to a low enough value and the physics were made more realistic.

Wall y^+ Calculations.

The viscous boundary layer can be divided into three sublayers as shown in Figure 4.5. To ensure accurate simulation of the flow field, the mesh near the wall must be properly sized and this relies on the correct wall treatment for the application. Due to the geometry of the flow domain, it was expected that there would be areas where both high wall y^+ and low wall-y^+ wall treatment would be required. To resolve this, a hybrid treatment termed all-y^+ wall treatment was used. The treatment emulates a low wall-y^+ wall treatment for fine meshes and a high wall-y^+ wall treatment for coarse meshes. For meshes with intermediate resolution, walls with cell-centroids that are in the buffer region of the boundary layer, a blending function is used as described in Figure 4.6.
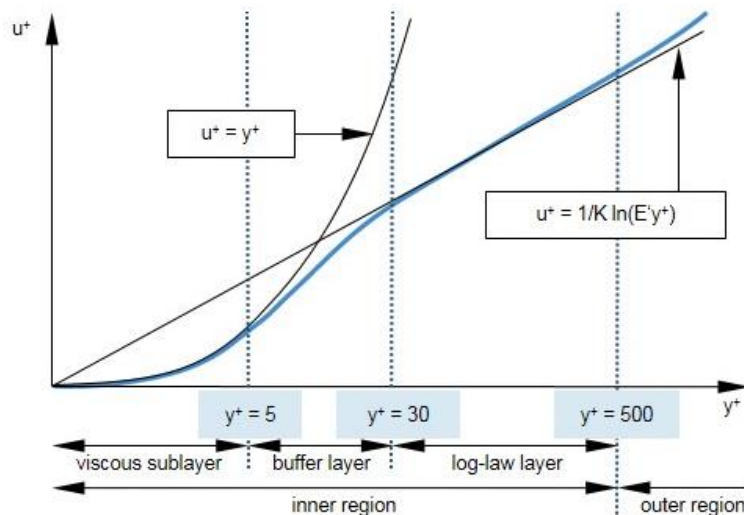
Figure 4.5: Boundary layer divided into three sub-layers (STAR-CCM+, 2015)
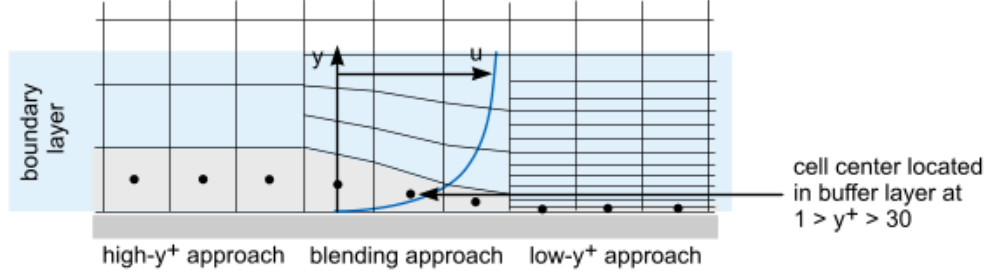
Figure 4.6: Blending approach for all-y⁺ wall treatment (STAR-CCM+, 2015)

In order to calculate the thickness, first the Reynold's number must be calculated:

$$Re_x = \frac{\rho \, U_\infty \, L}{\mu}$$ (5.15)

where ρ is density of nitrous oxide, U_∞ is the freestream velocity, L is the axial length of the flow domain and μ is the dynamic viscosity. Following this, the skin friction coefficient, C_f, is obtained:

$$C_f = \frac{0.026}{Re_x^{\frac{1}{7}}}$$ (5.16)

From this the skin shear stress on the wall, τ_{wall} is computed:

$$\tau_{wall} = \frac{C_f \, \rho \, U_\infty^2}{2}$$ (5.17)

Then:

$$U_{fric} = \frac{\sqrt{\tau_{wall}}}{\rho}$$ (5.18)

Finally, the distance between the wall and the centroid of the first cell (Δs) can be calculated:

$$\Delta s = \frac{y^+ \, \mu}{U_{fric} \, \rho}$$ (5.19)

Here y^+ refers to a desired value of y^+ rather than a calculated value. The geometry of the flow domain suggests that there will be both large areas of relatively slow moving fluid and areas of very high fluid velocity. This can produce areas where high-y^+ wall treatment is required and areas where low-y^+ wall treatment is needed. The above equations yielded a value of 1.516×10^{-5} m for the total thickness of the first layer. This was applied throughout all simulations.

As can be seen in Figure 4.7, there are a large range of wall y^+ values for the various sections of this simulation. The inlet and outlet sections of the valve remained largely in the low-y^+ region of boundary flow whilst the sections of high velocity, in particular the area at the exit of the ball section, show large wall y^+ values. Large areas of the ball section are situated in the buffer layer (between $y^+ = 5$ and $y^+ = 30$) as well as some areas of the valve after the ball.
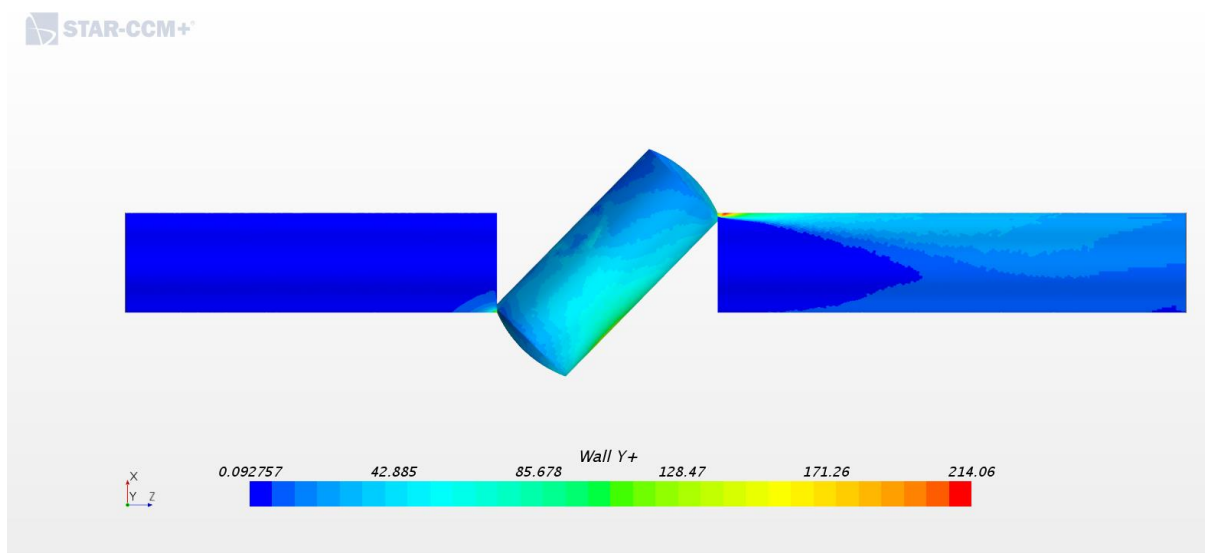
Figure 4.7: Wall y+ values after running the simulation

The initial inlet conditions were assumed to be fully liquid nitrous oxide at 20° C and 60 bar stagnation pressure. The solution did not converge when a stagnation pressure inlet condition was used so instead the inlet was initially set as a mass flow inlet with a roughly calculated value from previous hot fire tests, this was used until convergence was achieved where after the inlet condition was changed to a stagnation inlet. Outlet conditions were estimated from the open-loop tests to be approximately 28 bar; therefore, this was used as the value for the pressure outlet. At this angle it was assumed that the nitrous oxide will fully cavitate upon passing through the ball section of the valve, therefore the initial conditions were set such the volume fraction of nitrous oxide would be fully liquid at the inlet and fully gaseous at the outlet.

It was expected that the flow will cavitate when passing through the valve and so the Eulerian multiphase (volume of fluid) physics model was used. The flow was modelled as turbulent using the Reynolds-Averaged Navier Stokes turbulence solver in conjunction with the K-Epsilon model. The Volume of Fluid (VOF) model was used to determine the phase of the fluid using the density, temperature and surface tension properties of gaseous and liquid nitrous oxide. For cavitation, a Schnerr-Sauer model was employed. The same physics models were used for all simulations.

CFD Results

The nitrous oxide fully cavitated at the exit of the ball section of the valve. In Figure 4.8 it is seen that at the inlet section and within the ball section itself, the nitrous oxide is fully liquid while after exiting the ball the nitrous oxide rapidly cavitates to its fully gaseous state. This has implications regarding the throttling of the motor since the injector was designed to receive fully liquid nitrous oxide at the inlet. Figure 4.9 shows the pressure drop across the valve, with a total pressure drop of 32.4 bar from the inlet to the outlet of the valve. This drop in pressure is consistent with preliminary estimates and results from open-loop testing.
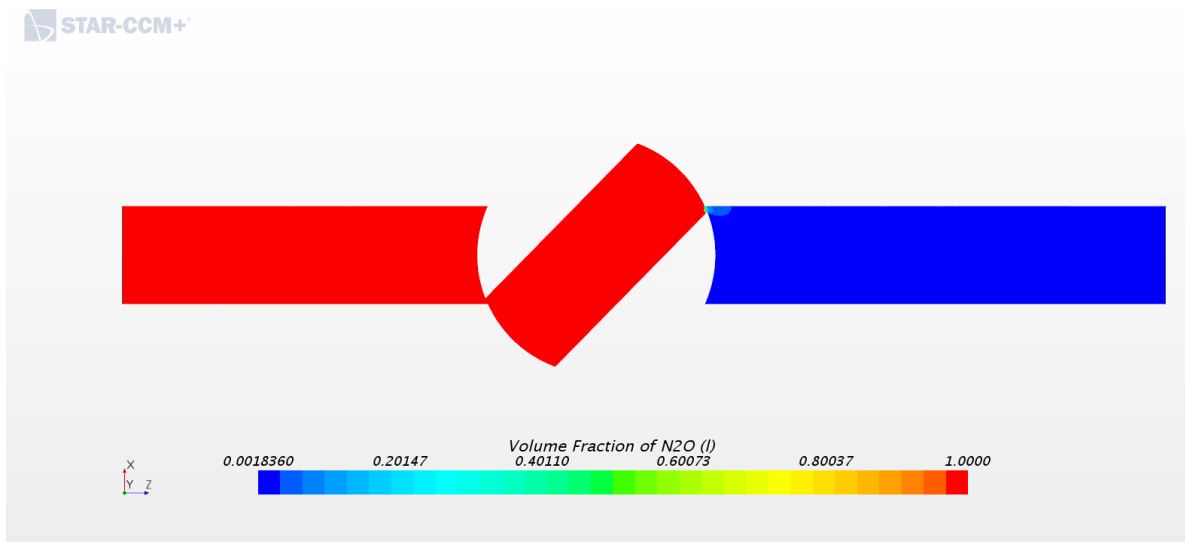
Figure 4.8: Representation of fraction of volume of nitrous oxide. Red indicates fully liquid whilst blue indicates fully gaseous. Intermediate colours represent intermediate volume fractions.
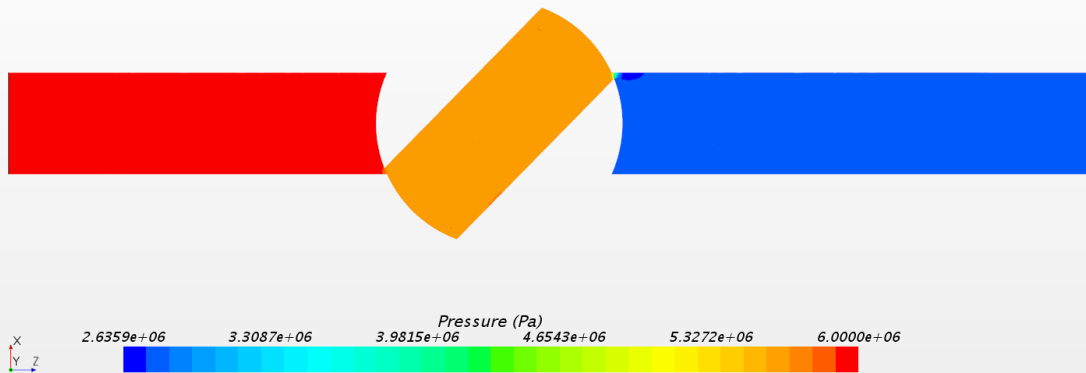
Figure 4.9: Pressure drop across the ball section of the valve

The velocity vectors of the flow through the valve were also modelled to examine the effects the internal geometry could have on the fluid. Figure 4.10 shows the velocity vectors as a line integral convolution with colour denoting magnitude. Maximum velocity occurs at the exit of the ball where the flow subsequently cavitates and causes swirling and various eddies to form. Figure 4.11 plots mass flowrate through the valve versus iterations of the simulation. The averaged mass flowrate value after the simulation had reached convergence is 0.0266 kg/s or 26.6 g/s. Figure 4.12 shows the resultant residuals for the simulation.
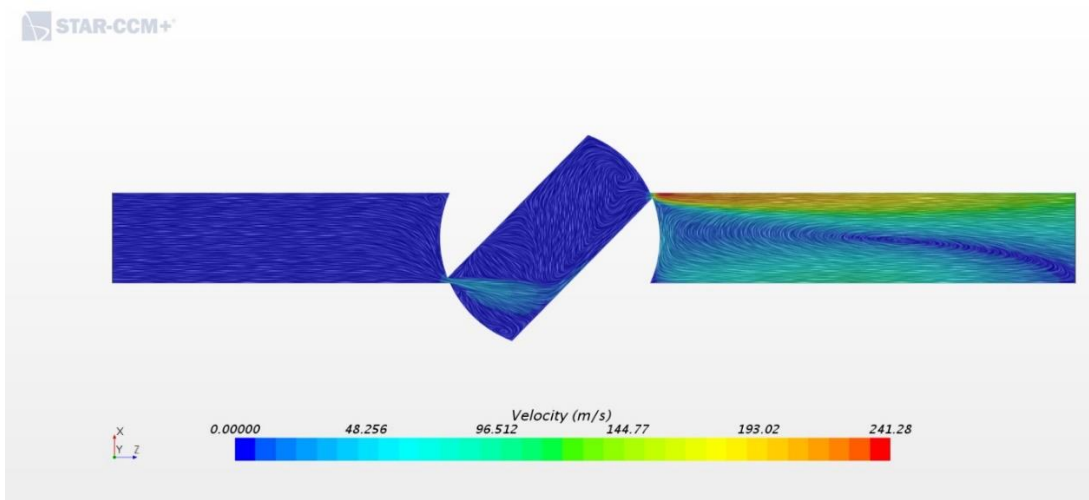
Figure 4.10: Velocity vectors and vortices through the valve

The simulation was repeated with the same mesh and physics parameters for two other valve angles, 51.5° and 65.5°, with the outlet pressures adjusted to that found in previous hot fire tests in reference to the same valve angle. The results of the mass flowrate values from each simulation were used to construct a profile from which the mass flowrate can be estimated in relation to the angle of the ball valve, as shown in Figure 4.13. From the value of mass flowrate one can calculate the thrust that could be generated and thus formulate an algorithm that relates valve angle and thrust for use in both open-loop and closed-loop control.
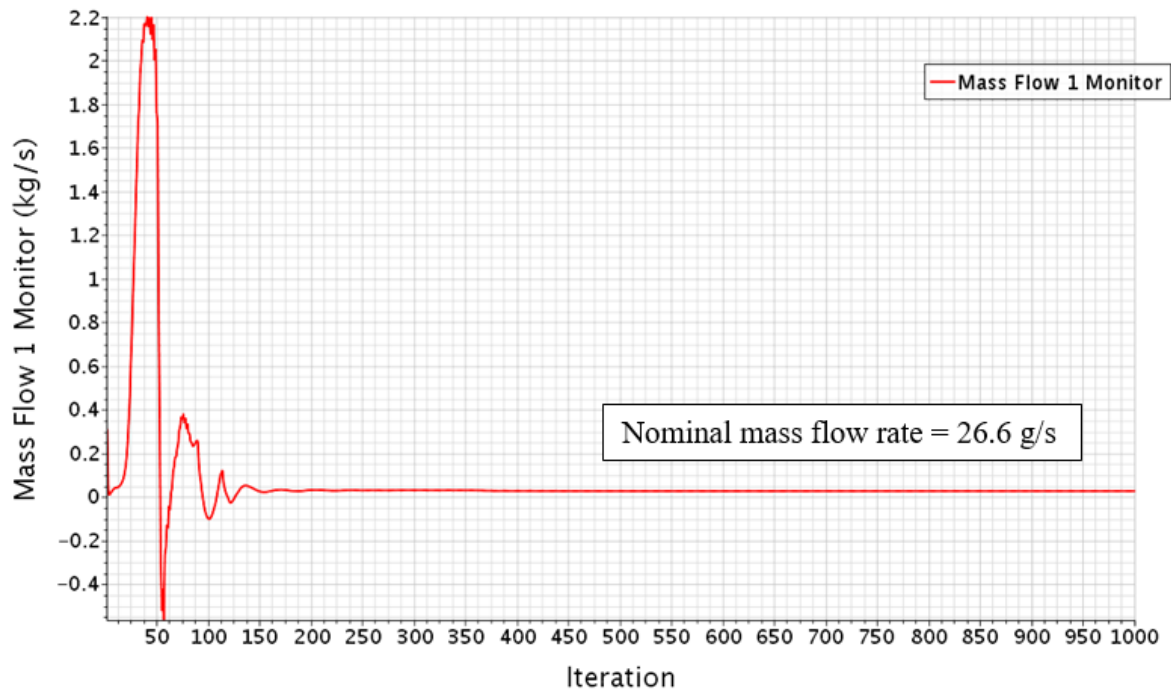
Figure 4.11: Mass flowrate [kg/s] vs the number of iterations in the simulation
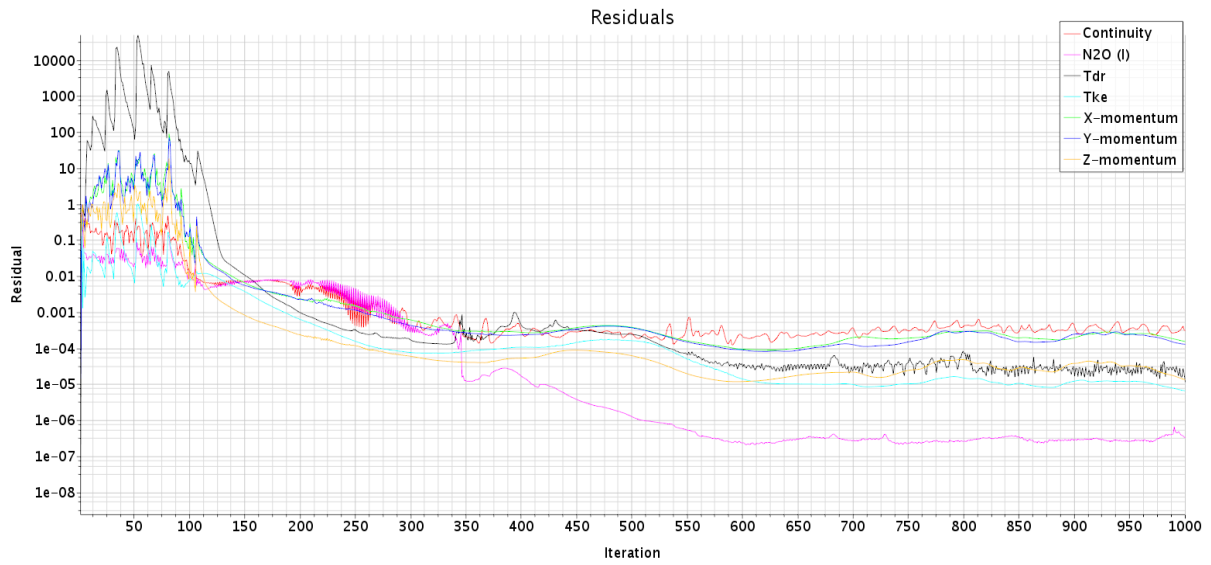
Figure 4.12: Residuals for the simulation

$$y = 0.0006x^2 - 0.0452x + 0.8159$$
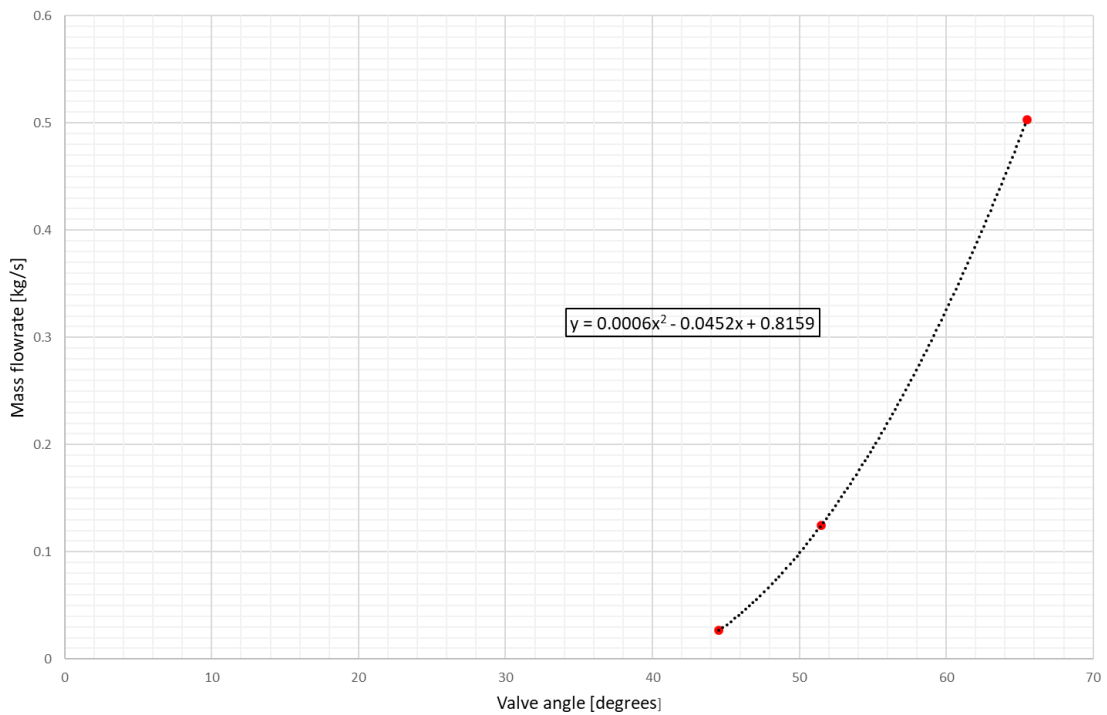
Figure 4.13: Mass flowrate versus valve angle as per computational simulations

Figure 4.13 shows the interpolation following the results from the three simulations run, using a simple quadratic function to create a line of best fit and obtain predictive data for every valve angle value. Although it is seen that the relationship is not strictly linear which might cause issues from a control perspective, this graph can be tabulated and allows the controller to effectively cancel the nonlinear characteristics by referring to this table in order to reach a specified mass flowrate and hence, thrust.

41

Operating this way, the controller becomes more robust and responsive by quickly moving to a valve angle position to obtain a specified thrust and then using the closed-loop mechanism to refine the command input with high fidelity. This setup and operation is further explained in Chapter 5.

4.4 INJECTOR MODEL

The injector was designed such that liquid nitrous oxide will enter the injector which would completely cavitate the flow into a fine, atomised mist projected axially through the port of the motor. The incompressible model will be considered:

$$\dot{m}_{inj} = C_d \, A_{inj} \, N_{inj} \sqrt{2 \, \rho_i (P_i - P_c)} \tag{4.20}$$

where $\dot{m}_{inj}$ is the mass flowrate of oxidiser through the injector, C_d is the discharge coefficient, A_{inj} is the cross-sectional area of a single port in the injector, N_{inj} is the total number of holes/ports in the injector, ρ_i is the density of oxidiser just before the injector, P_i is the oxidiser pressure just before the injector and finally, P_c is the combustion chamber pressure.

This equation suffices for the modelling of the injector section of the simulator and so no additional formulae are required. However, when a new injector had to be designed, the incompressible liquid model was deemed insufficient due to multiphase nature of the flow. For this reason, the homogenous equilibrium model (HEM) was employed. HEM takes into account multiphase flow but fails when the system being modelled involves high pressure differences and large driving potentials. The new injector design and equations are detailed in Chapter 7.

4.5 REGRESSION RATE MODELLING

Equation (4.21) was employed to calculate the total thrust of the motor:

$$F = \dot{m} \, V_e + (p_e - p_a) A_e \tag{4.21}$$

Here, F is force or the total thrust produced, $\dot{m}$ is the total mass flowrate of the motor, V_e is the exit velocity of gases out the nozzle, p_e is the exit pressure of the nozzle, p_a is atmospheric pressure, and A_t is the cross-sectional area of the throat. The regression rate of the motor is primarily concerned with the mass flowrate of the fuel ($\dot{m}_f$) and so only that component of the equation will be considered in this section. The total mass flowrate ($\dot{m}$) of the motor can be written separately as:

$$\dot{m} = \dot{m}_{n2o} + \dot{m}_f \tag{4.22}$$

Assuming the port of the fuel grain is fully circular and uniform throughout:

$$\dot{m} = \rho_f \, A_g \dot{r} \qquad (4.23)$$

where ρ_f is the density of the fuel, A_g is the surface area on the inside of the port of the grain, and $\dot{r}$ is the regression rate of the fuel. Expanding the surface area term:

$$\dot{m} = \rho \, \pi \, D(t) \, L \, \dot{r} \qquad (4.24)$$

where $D(t)$ is the diameter of the port as a function of time and L is the axial length of the fuel grain port. According to classical regression rate theory:

$$\dot{r} = a \, G_{ox}^n \qquad (4.25)$$

where G_{ox} is the oxidiser mass flux, and a and n are experimentally obtained for individual oxidiser/fuel combinations. The values for a and n were first approximated using values empirically derived from Stanford University (Karabeyoglu, et al., 2001) but were later adapted to more precise values after sufficient experimentation had taken place and regression rate could be measured with reasonable accuracy. Oxidiser mass flux is defined as:

$$G_{ox} = \frac{4 \, \dot{m}_{ox}}{\pi \, D(t)^2} \qquad (4.26)$$

The oxidiser mass flux term (G_{ox}) can therefore be expanded further:

$$\dot{r} = a \left(\frac{4 \dot{m}_{ox}}{\pi \, D(t)^2} \right)^n \qquad (4.27)$$

It follows then:

$$\dot{m}_f = \rho_f (\pi \, D(t) \, L) a \left(\frac{4 \dot{m}_{ox}}{\pi D(t)^2} \right)^n \qquad (4.28)$$

It can be seen the mass flowrate of fuel can be expressed as a function of the mass flowrate of oxidiser, and therefore the total mass flowrate as a function of oxidiser flowrate:

$$\dot{m} = \dot{m}_{ox} + [\rho_f \, \pi \, D(t) \, L \, a] \left[\frac{4 \dot{m}_{ox}}{\pi D(t)^2} \right]^n \qquad (4.29)$$

Most variables in Equation (4.29) are constants based on physical characteristics of the fuel grain and constants derived empirically. This equation shows that the total mass flowrate of the motor is dependent on only the mass flowrate of oxidiser. The only other non-constant variable is the diameter of the port at a given time ($D(t)$). Since this is dependent on the regression rate, the simulator will employ a 4th order Runge-Kutta time marching scheme to predict values given a user defined time-step. In order to calculate the instantaneous diameter at any given time, the following equation can be used (Sutton and Biblarz, 2001):

$$D(t) = 2\left(a(2n+1)\left(\frac{\dot{m}_{ox}}{\pi}\right)^n t + R_i^{2n+1}\right)^{\frac{1}{2n+1}} \tag{4.30}$$

where R_i is the initial radius of the fuel grain port.

4.6   GAS DYNAMICS MODELLING AND NASA CEA

From Equation (4.21) only one variable remains to be calculated, namely exit velocity (V_e). The exit velocity of the motor can be calculated as follows:

$$V_e = \sqrt{\frac{2\,k}{k-1}\frac{R}{M}T_1\left[1-\left(\frac{p_2}{p_1}\right)^{\frac{k-1}{k}}\right]} \tag{4.31}$$

where k is the ratio of specific heats of combustion, M is the molar mass of the combustion gases, R is the universal gas constant, T_1 is the temperature at the nozzle inlet, p_1 is the pressure at nozzle inlet, and p_2 is the pressure at nozzle outlet. Exit velocity can also be calculated by:

$$V_e = \eta_{eff}\, c^*\, C_F \tag{4.32}$$

where η_{eff} is the combustion efficiency, c^* is the characteristic velocity, and C_F is the thrust coefficient. Typically, the combustion efficiency ranges from 92% to 99% (Sutton and Biblarz, 2001), for the purposes of the simulation the combustion efficiency will be assumed to be constant at 0.95 (95%). C_F can be calculated by:

$$C_F = \lambda\sqrt{\left(\frac{2k_c^2}{k_c-1}\right)\left(\frac{2}{k_c+1}\right)^{\frac{k_c+1}{k_c-1}}\left(1-\left[\frac{P_e}{P_c}\right]^{\frac{k_c-1}{k_c}}\right)} + \left(\frac{P_e-P_a}{P_c}\right)\left(\frac{A_e}{A_t}\right) \tag{4.33}$$

where λ represents the nozzle correction factor, P_e is the nozzle exit plane pressure, P_a is the pressure of the surrounding atmosphere and A_e represents the cross-sectional area of the nozzle exit plane. Using these equations, the thrust can be obtained by:

$$F = \dot{m}_{noz}\eta_{eff}c^*\left[\lambda\sqrt{\left(\frac{2k_c^2}{k_c-1}\right)\left(\frac{2}{k_c+1}\right)^{\frac{k_c+1}{k_c-1}}\left(1-\left[\frac{P_e}{P_c}\right]^{\frac{k_c-1}{k_c}}\right)}+\left(\frac{P_e-P_a}{P_c}\right)\left(\frac{A_e}{A_t}\right)\right] \quad (4.34)$$

In order to calculate the fluid flow and pressure fluctuations inside the combustion chamber, a zero-dimensional model was utilized. This model assumes that there is no change in pressure through the chamber and that the combustion product behaves like an ideal gas. Uniform regression rate is also assumed. The model used is the same created and described by Genevieve (2013), and employs a fourth order Runge-Kutta time marching scheme to solve for state vectors. The model determines the change in fuel regression rate and chamber pressure in relation to the change in oxidiser mass flowrate. This is instrumental in modelling the behaviour of the motor during throttling.

All the combustion gas properties, such as the specific heat capacity and specific heat ratio are calculated by the NASA Chemical Equilibrium with Applications (CEA)™ program for a specified chamber pressure and O/F ratio. NASA CEA™ is a code developed by Gordon and McBride (1994) to obtain chemical equilibrium compositions and transport properties for specified thermodynamic states. The program also calculates theoretical rocket performance for both finite and infinite-area combustion chambers. The input values that are fed into NASA CEA™ are chamber pressure, oxidiser/fuel properties, nozzle expansion ratio, and the O/F ratio. NASA CEA™ calculates the exit velocity, combustion gas temperature, and specific heat ratios which is modelled through the nozzle to obtain the thrust of the motor.

4.7 NOZZLE DYNAMICS

Fluid flow is modelled through the nozzle with idealised assumptions. Figure 4.14 shows the cross-section of the nozzle setup on the laboratory-scale motor. One-dimensional flow theory is employed which will provide sufficient accuracy for this application. For these calculations the following assumptions are made:

1. The fluid behaves like an ideal gas
2. The nozzle inlet gas velocity is assumed to be zero
3. The gaseous mixture is completely homogenous
4. The flow expansion is adiabatic
5. Exhaust gas flow is one-dimensional, i.e. all velocity vectors are axially directed
6. After leaving the combustion chamber, the gas composition does not change inside the nozzle

7. Boundary layer effects and lambda shocks are ignored
8. The chamber pressure is equal to the stagnation pressure and the chamber temperature is equal to the stagnation temperature
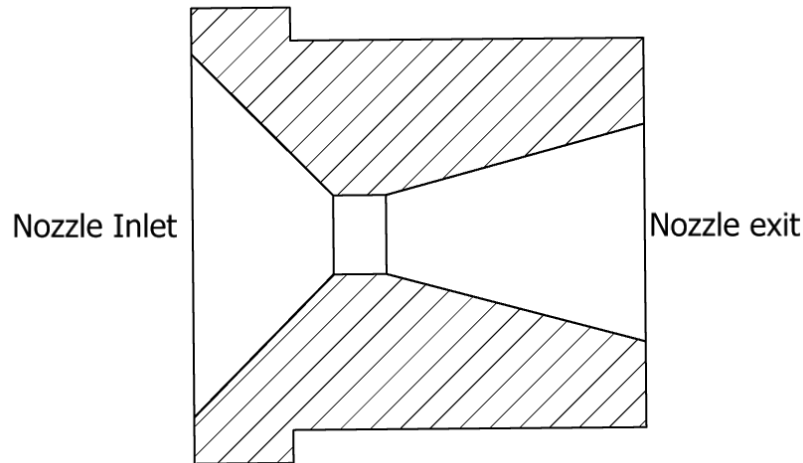
Figure 4.14: Section view of laboratory-scale hybrid rocket motor nozzle

The gas flow properties and conditions change depending on the ratio of chamber pressure to atmospheric pressure, $\left(\frac{P_c}{P_a}\right)$. These changes are more pronounced for a launch vehicle in flight due to the varying atmospheric pressures as altitude increases than for motors tested at sea level. However, even at ground level testing, a hybrid rocket motor undergoes a wide change in pressure ratios during the start-up sequence and various other transient conditions such as when the motor is being throttled. In general, there are three critical pressure ratios that a hybrid motor could experience during a hot fire test. Figure 4.13 shows the distribution of pressures in a converging-diverging nozzle for a variety of flow conditions. When the pressure ratio is above the 1st critical condition (that is, above line A-H), the flow is deemed sub-sonic throughout and acts as a venturi. Here the flow is considered to be "unchoked" meaning the Mach number of the fluid through the throat of the nozzle is below 1.
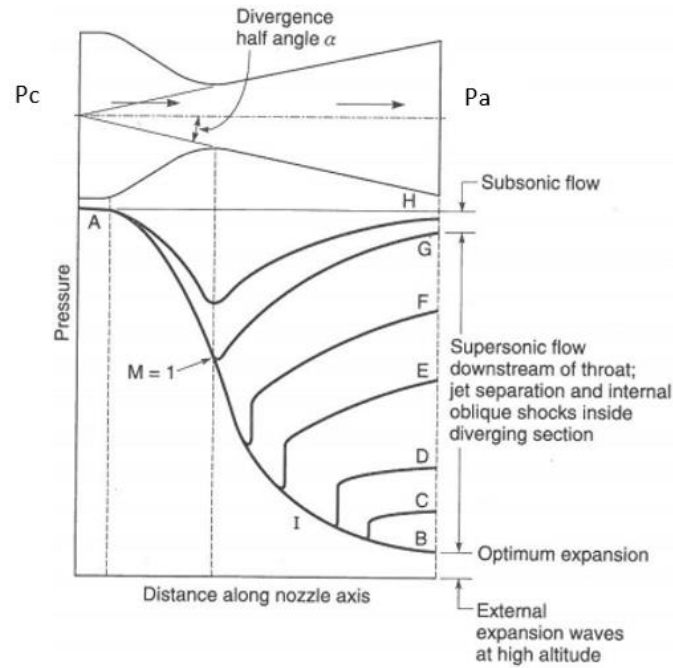
Figure 4.15: Pressure distributions inside a nozzle for varying pressure conditions. In this figure nozzle inlet pressure remains the same while exit pressure varies (Sutton and Biblarz, 2001)

If the pressure ratio is between the first and second critical ratio (between lines A-H and A-B) the flow is choked and a normal shock occurs downstream of the nozzle throat at some point in the diverging section. The flow is supersonic from the throat until it encounters the first shock, thereafter the flow is subsonic. The second critical point corresponds to when the shock is in the same plane as the exit plane of the nozzle and flow is supersonic from the throat until the exit plane. Line A-B represents the third critical condition, which is also the condition where optimal thrust is obtained. Here the pressure at the exit of the nozzle is equivalent to the atmospheric pressure. Flow regimes below the third critical point (called under-expansion) create expansion waves outside the nozzle, and flow regimes between the second and third critical points, called over-expansion, create compression waves outside the nozzle.

In order to obtain an accurate model for a hybrid rocket motor, all pressure ratios were factored in due to the inherent transient nature of throttling rocket motors.

4.7.1   Subsonic Flow Regimes
The flow through the nozzle is characterised as subsonic when the pressure ratio is equal to or above the first critical pressure ratio. A more accurate rendering of Equation (4.21), taking into account various efficiencies, is described by:

$$F = \lambda \eta_{eff} \dot{m}_{noz} v_e + (P_e - P_a) A_e \qquad (4.35)$$

where F is the force or thrust produced, λ is the nozzle exit angle correction factor, η_{eff} is the combustion efficiency, $\dot{m}_{noz}$ is the mass flowrate of gas through the nozzle, v_e is the exit velocity of gas leaving the nozzle, P_e is the pressure at the nozzle exit, P_a is the atmospheric pressure and A_e is the cross-sectional area of the nozzle exit. The exit velocity can be calculated by first finding the Mach number at exit and the temperature at exit:

$$M_e = \left(\frac{\left(\frac{P_{o,e}}{P_e} \right)^{\frac{(k_c-1)}{k_c}} - 1}{\frac{[k_c-1]}{2}} \right)^{\frac{1}{2}} \tag{4.36}$$

where $P_{o,e}$ is the stagnation pressure at the nozzle exit, and k_c is the specific heat ratio in the chamber. The temperature can be calculated as:

$$T_e = \frac{T_{o,e}}{\left[1 + \left(\frac{k_c-1}{2} \right) M_e^2 \right]} \tag{4.37}$$

where T_e is the exit temperature and $T_{o,e}$ is the stagnation temperature at the nozzle exit and is equivalent to the stagnation temperature in the chamber, $T_{o,c}$, and the static temperature in the chamber, T_c, because of the perfect gas assumption. The exit velocity can then be calculated by:

$$v_e = M_e \sqrt{k_e R_e T_e} \tag{4.38}$$

where k_e and R_e are the specific heat ratio at exit and the gas constant at exit, respectively. Since it is assumed that the flow composition remains unchanged, $k_e = k_c$ and $R_e = R_c$. When the pressure ratio is equivalent to the first critical point, the Mach number at the throat is 1. However, for pressure ratios above the first critical ratio, the throat Mach number must be computed iteratively from the following equation:

$$\frac{A_e}{A_t} = \frac{M_t}{M_e} \left[\frac{1 + \left(\frac{[k_c-1]}{2} \right) M_e^2}{1 + \left(\frac{[k_c-1]}{2} \right) M_t^2} \right]^{\frac{k_c+1}{2(k_c-1)}} \tag{4.39}$$

Knowing the nozzle expansion ratio, A_e / A_t, and the Mach number at the exit of the nozzle, the Mach number at the throat, M_t, can be calculated using a simple iterative loop. If the pressure ratio is the same as the first critical point, the mass flowrate through the nozzle can be calculated by:

$$\dot{m}_{noz} = \frac{P_c A_t}{\eta_{eff} c^*} \tag{4.40}$$

If the flow is not choked, that is, if the Mach number at the throat is less than 1, the following equation is used:

$$\dot{m}_{noz} = \frac{\rho_e A_e v_e}{\eta_{eff}} \tag{4.41}$$

Here ρ_e is the density of the gas at the exit of the nozzle and is defined from the ideal gas assumption as follows:

$$\rho_e = \frac{P_e}{R_e T_e} \tag{4.42}$$

The results from Equations (4.39), (4.40) and (4.38) can be substituted into the thrust equation, Equation (4.35) and the thrust can be calculated for sub sonic flows.

4.7.2 Supersonic Flow Regimes

Supersonic flow regimes are those that occur when the pressure ratio is below that of the second critical point. Here the flow is subsonic in the converging section and supersonic in the diverging section. For clarity, when the pressure ratio of the flow is between the second and third critical points, the flow is defined as over-expanded. When the pressure ratio is equal to the third critical point, the flow is defined as perfectly expanded. Finally, if the pressure ratio of the flow is less than the third critical point, the flow is defined as under-expanded.

For supersonic flow the Mach number in the throat is necessarily equal to one, and so the Mach number at the exit, M_e, can be calculated using an iterative process as follows:

$$\frac{A_e}{A_t} = \frac{1}{M_e} \left[\frac{1 + \left(\frac{[k_c - 1]}{2} \right) M_e^2}{1 + \left(\frac{[k_c - 1]}{2} \right)} \right]^{\frac{k_c + 1}{2(k_c - 1)}} \tag{4.43}$$

The pressure at the exit of the nozzle is thereafter calculated:

$$P_e = \frac{P_{o,e}}{\left[1 + \left(\frac{[k_c - 1]}{2} \right) M_e^2 \right]^{\frac{k_c}{k_c - 1}}} \tag{4.44}$$

Following this, Equations (4.37) and (4.38) are used to calculate nozzle exit temperature and velocity respectively. All relevant variables are substituted into Equation (4.40) to determine the mass flowrate through the nozzle for choked conditions. Finally, the thrust can be calculated using Equation (4.35).

4.7.3 Normal Shock Wave Flow Regimes

Normal shock wave flow regimes occur when the pressure ratio is above the second critical point but below the first. Flow is subsonic in the converging section and supersonic in the diverging section until the shock, the flow is subsonic after the shock. The Mach number at the throat is equal to 1.

To obtain the Mach number at the exit of the nozzle an iterative process is required of the product of Equations (4.43) and (4.44):

$$\frac{A_e}{A_t}\frac{P_e}{P_c} = \frac{1}{M_e}\left[\frac{1+\left(\frac{[k_c-1]}{2}\right)M_e^2}{1+\left(\frac{[k_c-1]}{2}\right)}\right]^{\frac{k_c+1}{2(k_c-1)}} \times \frac{1}{\left[1+\left(\frac{[k_c-1]}{2}\right)M_e^2\right]^{\frac{k_c}{k_c-1}}} \tag{4.45}$$

All losses are assumed to take place across the shock, the exit pressure of the nozzle is assumed to be equal to atmospheric pressure, and the flow is assumed to be isentropic after the shock wave. Therefore $P_{o,1} = P_{o,c}$ and $P_{o,2} = P_{o,e}$ where the subscript "1" denotes a position just before the shock and "2" a position just after. The pressure ratio across the shock wave can be calculated as:

$$\frac{P_{o,2}}{P_{o,1}} = \frac{P_{o,e}}{P_{o,c}} \tag{4.46}$$

To find the stagnation exit pressure Equation (4.44) is used whilst the Mach number just before the shock, M_1, is given by:

$$\frac{P_{o,2}}{P_{o,1}} = \left[\frac{\left(\frac{[k_c+1]}{2}\right)M_1^2}{1+\left(\frac{[k_c-1]}{2}\right)M_1^2}\right]^{\frac{k_c}{(k_c-1)}} \times \left[\left(\frac{2k_c}{k_c+1}\right)M_1^2 - \left(\frac{k_c-1}{k_c+1}\right)\right]^{\frac{1}{1-k_c}} \tag{4.47}$$

The axial location of the shock wave in the nozzle is assumed to be determined by the pressure ratio across the nozzle. As such the location at an area expansion ratio can be calculated thus:

$$\frac{A_1}{A_t} = \frac{1}{M_1}\left[\frac{1+\left(\frac{[k_c-1]}{2}\right)M_1^2}{1+\left(\frac{[k_c-1]}{2}\right)}\right]^{\frac{k_c+1}{2(k_c-1)}} \tag{4.48}$$

In order to calculate the pressure and temperature after the shock wave, the temperature and pressure before the shock wave first needs to be found. Pressure before the shock is given by:

$$P_1 = \frac{P_c}{\left[1 + \left(\frac{[k_c - 1]}{2}\right) M_1^2\right]^{\frac{k_c}{k_c - 1}}}$$
(4.49)

Similarly, the temperature before the shock is calculated as:

$$T_1 = \frac{T_c}{\left[1 + \left(\frac{[k_c - 1]}{2}\right) M_1^2\right]}$$
(4.50)

From this the pressure and temperature after the shock can be determined:

$$P_2 = P_1 \left[\frac{1 + k_c M_1^2}{1 + k_c M_2^2}\right]$$
(4.51)

$$T_2 = T_1 \left[\frac{1 + \left(\frac{[k_c - 1]}{2}\right) M_1^2}{1 + \left(\frac{[k_c - 1]}{2}\right) M_2^2}\right]$$
(4.52)

Using these variables, the stagnation conditions after the shock for pressure and temperature can be calculated. Since the flow is assumed to be isentropic after the shock, $P_{o,2} = P_{o,e}$ and $T_{o,2} = T_{o,e}$.

$$P_{o,2} = P_2 \left[1 + \left(\frac{[k_c - 1]}{2}\right) M_2^2\right]^{\frac{k_c}{k_c - 1}}$$
(4.53)

$$T_{o,2} = T_2 \left[1 + \left(\frac{[k_c - 1]}{2}\right) M_2^2\right]$$
(4.54)

$$T_e = \frac{T_{o,2}}{1 + \left(\frac{[k_c - 1]}{2}\right) M_e^2}$$
(4.55)

Using these results, the mass flowrate is calculated by Equation (4.40) and thereafter the thrust can finally be determined by Equation (4.35).

4.8   CONCLUSION

In this chapter a full mathematical model of the laboratory-scale motor was described. The purpose was to predetermine viable parameters for the implemented control regimen. The model makes use of control volumes where each separate element of the test stand is mathematically described and later integrated to form the final model. A CFD analysis was done on the nitrous oxide flow through the ball valve due to model multiphase flow. The results were used to construct a look-up table relating a particular valve angle with an oxidiser mass flowrate which the model used where necessary. NASA's CEA™ program was used alongside the model to calculate combustion properties and conditions prior to the nozzle inlet.

5   CONTROL REGIME

5.1   INTRODUCTION

Laboratory-scale hybrid rocket motors, even those constructed identically and fired in an automated fashion, can exhibit substantial variability in thrust output, as described by Peterson (2012). All N_2O-Paraffin wax motors express this variability which is caused by a number of factors including whether there exist bubbles or voids in the grain, ambient temperature and pressure, and run-tank pressure.

A PID control scheme was prescribed to maintain the hybrid rocket thrust levels at a given set point. The derivative aspect of the control scheme is problematic in transient application as it is known to amplify higher frequency process noise that could cause large changes and oscillations in controller output. This resulted in the decision to use only the Proportional-Integral (PI) components of the controller (Peterson, 2012).

A research objective of this dissertation was to implement optimal parameters on the controller to yield effective and efficient results. Two primary criteria were considered when evaluating whether the given control scheme is functioning in an acceptable manner. The first is disturbance rejection, keeping the process variables at a given set point, and the second is command tracking, referring to how well the controller tracks the command set point. The degree to which the controller tracks the command set point well is determined by rise time (the time it takes for the process variables to meet the command set point), settling time (the time required for the process variable to settle within a predetermined error band) and overshoot (the percentage the process variables overshoot the command set point) criteria.

Parameter considerations

Controller parameters were determined based on the allowable amount of overshoot in system response, settling time, and steady state error. In addition, the minimum time taken to reach the prescribed set-point was important in choosing the most appropriate control parameters. The controller was designed for use in a variety of applications, and for this reason, the controller parameters that were chosen were responsive and had a very small steady state error. This required a trade-off in undesirable overshoot and settling time. A number of control parameters were input into the simulator and from this a final set was chosen for use on the test stand.

5.2   OVERVIEW AND METHODOLOGY

1. Performance data from the laboratory-scale hybrid rocket motor system was first analysed graphically by observing characteristics such as the thrust peak amplitude and settling time, from which a first-order plus dead time (FOPDT) model was calculated. This was used to obtain initial controller tuning constants.

2. A second-order transfer function was obtained graphically from results for previous pure-paraffin hot-fire tests. This is an empirical description of a stable dynamic process and was used to verify the transfer function obtained from the simulator.

3. The mathematical model described in Chapter 5 was used to simulate the system response from various inputs. The response was used to generate a final transfer function. The transfer function was compared to previous iterations and, if valid, used to find more precise controller tuning constants.

4. A controller was designed and embedded into the code used to run and control the laboratory scale motor.

5. Effects such as nonlinearity of the valve's flow characteristic were considered and implemented into the controller.

A simulation model of the hybrid rocket laboratory-scale motor was developed in order to predict suitable control parameters without the cost and time of repeatedly making and firing laboratory-scale motors. In addition, to ensure accuracy and to obtain the approximate parameters of the controller, a first order plus dead time (FOPDT) model was created from the step response observed in previous test data. This also allowed for comparison to the transfer function generated by the simulator so as to ensure the parameters were within reasonable bounds. This required a simulated step response of the system. A FOPDT model transfer function is defined as follows:

$$H(s) = \frac{K_p e^{-\theta_D s}}{1 + \tau s} \qquad (5.1)$$

where K_p is the process gain, τ is the process time constant, and θ_D is the process dead time. The process gain is calculated by the change in process output over the change in process input, or $\left(\frac{\Delta y}{\Delta u}\right)$. The process time constant is calculated by finding the amount of time needed for the output to reach $(1 - e^{-1})$ or 63.2% of steady state conditions, or formally put, if initial condition $y(0) = 0$ and at time $t = \tau_p$ then:

$$y(\tau_p) = (1 - e^{-1})K_p \, \Delta u = 0.632 \, K_p \Delta u \qquad (5.2)$$

The process time delay is simply expressed as a time shift in the input variable. Figure 5.1 shows the step response characteristics that are analysed.
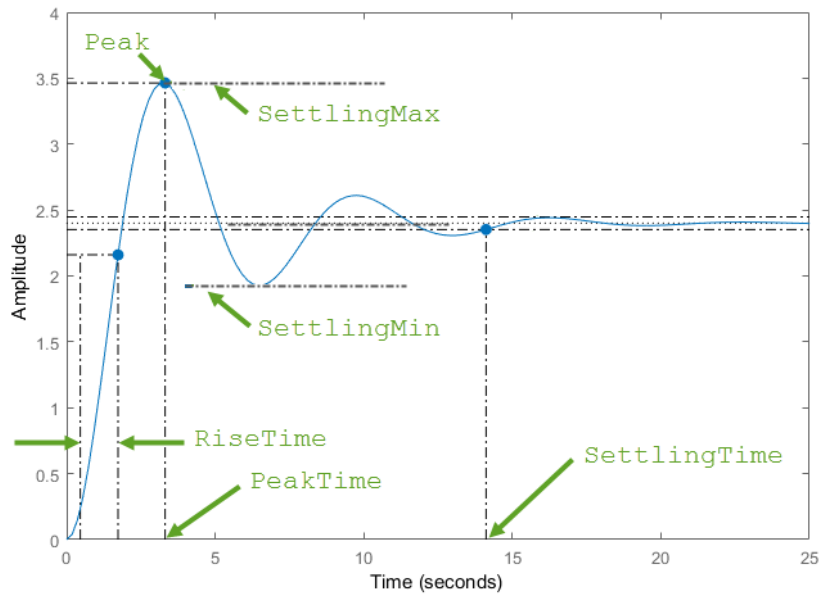
Figure 5.1: Important aspects of a step response (Mathworks, 2006)

Following this, results from a number of previous pure paraffin hot-fire tests were graphically analysed and, using established methods such as those proposed by Smith and Copripio (1985), a transfer function was derived. In this work, the ignition and subsequent start-up of the motor were treated as a step input, following which, certain aspects and characteristics of the response are identified and analysed. This method is often used in industry where complex systems make it unfeasible to mathematically derive a suitable transfer function, which is often more inaccurate. Due to the various transients, complex combustion, multiphase flow and so on, this method is also applicable to the creation of transfer functions for hybrid rocket motors. Figure 5.2 shows the resulting step response from the transfer function derived from graphical analysis and given as Equation (5.3).

$$H(s) = \frac{7.36}{s^2 + 2.937s + 7.885} \tag{5.3}$$
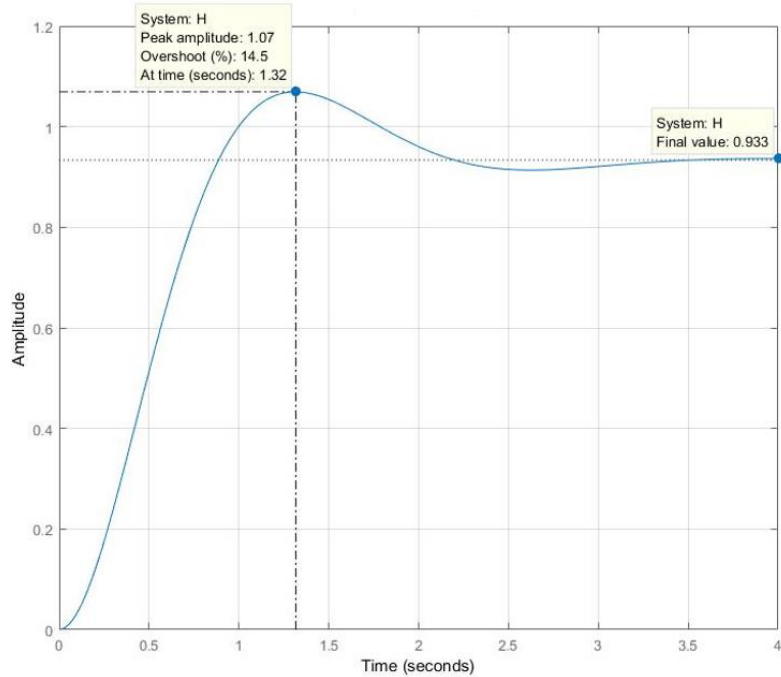
Figure 5.2: Step response of transfer function obtained from graphical analysis

For the sake of accuracy, a number of tests were compared and the various characteristics (settling time, overshoot and so on) were averaged when calculating the transfer function. The transfer function was used in simulation to obtain controller constants which were compared to those derived from the mathematical simulation so as to ensure that major discrepancies did not exist that may have affected the laboratory-scale rocket test.

Using this function, it is possible to roughly predict the controller response for a range of controller parameters and throttling regimes. The data-derived function was used to ensure that the simulated transfer function performed within reasonable bounds.

The mathematical simulator that was detailed in Chapter 4 was used create the final transfer function, labelled Equation (5.4). This function was simulated from which criteria were obtained for desired parameters. Controller constants were then obtained, and compared to the controller constants from the previous transfer function, Equation (5.3), to verify the output of the mathematical simulation.

$$H(s) = \frac{12.788}{s^2 + 3.416s + 12.788} \tag{5.4}$$

Using this transfer function, the controller parameters were found by running a LabVIEW™ simulation loop and adjusting the Proportional, Integral, and Derivative constants until the desired output was obtained. The LabVIEW™ setup is shown in Figure 5.3
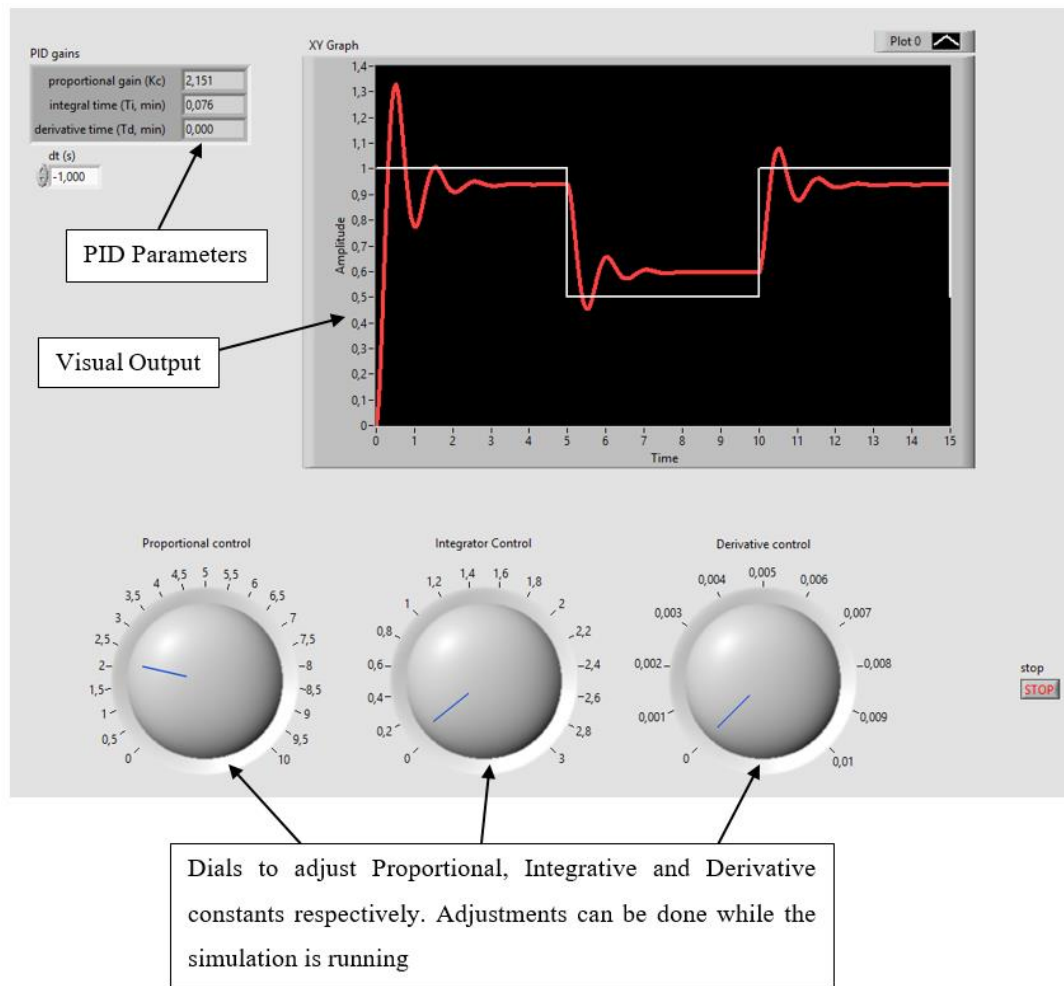
Figure 5.3: Control panel of simulation used to select controller constants.

The controller constants derived from simulation were implemented into the LabVIEW™ software used to run and control the test motor. The parameters derived from this final transfer function are indicated in Table 5.1.

Table 5.1: Parameters derived from final transfer function

Parameter	Value
Proportional Gain [P]	1.250
Integral Gain [I]	0.015
Derivative Gain [D]	0.004

These parameters were integrated into the LabVIEW™ virtual PID controller for use on the closed-loop hot fire testing of the laboratory-scale motor, depicted in Figure 5.4. The controller was designed to be run inside a loop running every 250 ms to mitigate the effects of the derivative function due to the noisy signal from the load cell measuring thrust.
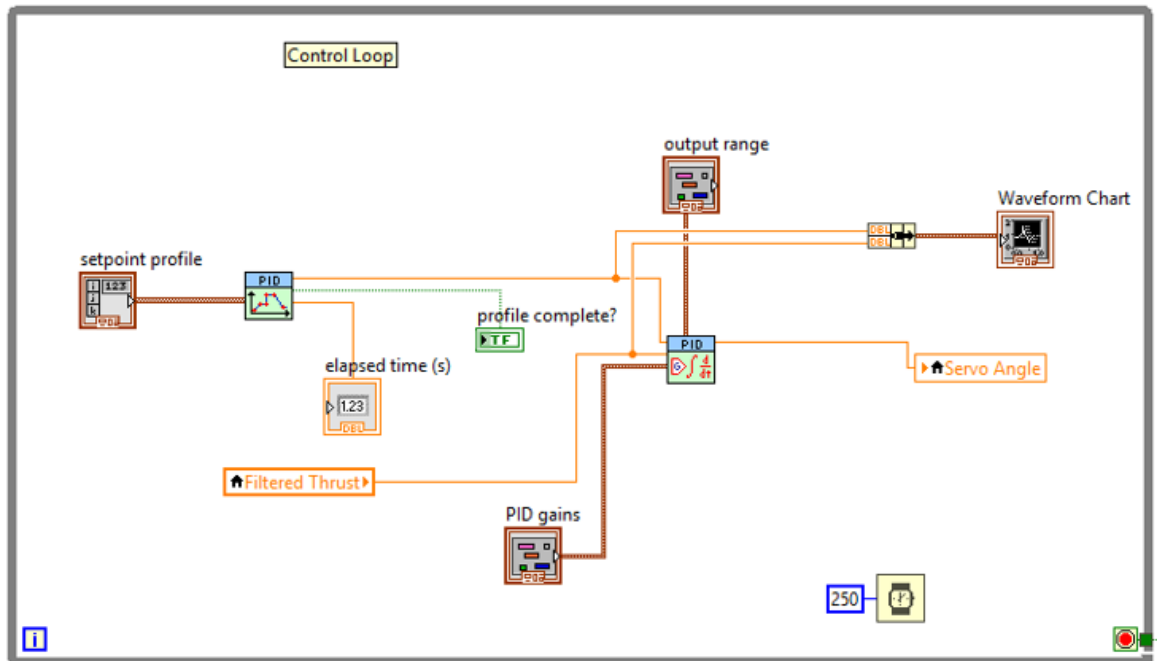
Figure 5.4: Early version of control scheme setup

Ultimately this set-up did not produce satisfactory results due to transients and non-linearities present in the laboratory-scale motor, and was updated to include safety mechanisms, valve angle change rate limiters and coercion algorithms. The derivative constant was set to zero in order to produce a smooth output that was used to control the final three successful closed-loop hot fire tests. This control loop is shown in Figure 5.5 and Table 5.2 gives a description of the associated figures.
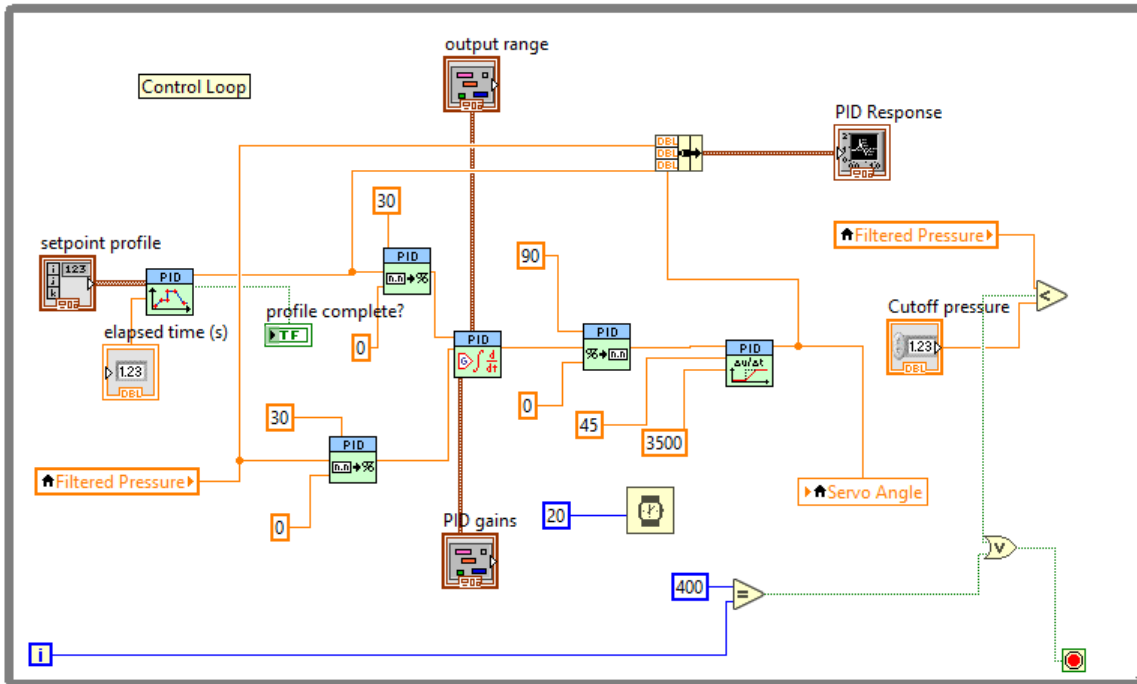
Figure 5.5: Updated control scheme with valve angle rate limiters and safety mechanisms

Table 5.2: Explanation of figures in control loop

Figure	Explanation
	PID set-point input
	Conversion from engineering units to a percentage
	PID controller. PID constants are set here.
	Conversion from percentage to engineering units
	Rate-limiter. Sets maximum units/second

5.3   NONLINEARITY

A through-bore ball valve was selected for modulating the flowrate of oxidiser to the motor. Ball valves inherently exhibit a non-linear flow characteristic which makes integration into PID controlled systems, that are designed for linear first-order control systems, problematic. There are a number of methods used to counteract the nonlinearity of a particular system depending on which component of the system

exhibits the nonlinear behaviour. In the case of the ball valve, a compensator or a gain scheduling scheme could be integrated. A compensator uses empirical data united with computer software to characterise the behaviour of the valve angle with respect to the flowrate of oxidiser. This essentially allows the controller to send a signal to the servo motor that corresponds to a linear relationship. Yet, with the nature of hybrid motors, this becomes inaccurate due to the difficulties associated with yielding consistent, repeatable results with the accuracy needed to implement a reliable compensator.

Gain scheduling pertains to setting different controller parameters corresponding to various states within the system. Regarding the ball valve flow characteristic, there is clearly a mostly linear region of the ball valve flow characteristic within the middle of the ball valve angle range, which becomes exponential toward either end of the range. Gain scheduling techniques were considered by discretizing the flow characteristic and setting appropriate parameters for each section. It was observed that, for this application, this was unnecessarily complicated and unlikely to have consistent success over a series of motors, because of the transient response of hybrid motors.

Another solution is to throttle the motor only within the constraints where the valve exhibits linear or near-linear flow characteristic and restrict the controller to not achieve valve angles outside these constraints. This is a viable approach and easy to implement since the controller does not have to compensate for the non-linearities inherent in ball valve flow configurations. However, this means the overall throttlabilty of the motor is limited to that which can be achieved in the valve angle range. Also, due to the blowdown configuration of the oxidiser run-tank, as the pressure decays over time, the valve will have to either open or close more than the limits allow to achieve a certain thrust set point in the later stages of the burn.

5.4   FEEDFORWARD LOOKUP TABLE

Due to the transient nature of the motor as well as the non-linearity of the ball valve flow characteristic, it was considered beneficial to employ a feed-forward loop in the controller as an aid to reject disturbance, mitigate transient effects, and, most importantly, to counter the effects of the non-linear flow characteristic. Figure 5.6 shows a feed-forward lookup table configured within a feedback loop. In an ideal environment, feed-forward exclusive control would be preferable as theoretically the response would be faster with less error. However, with high levels of variability from motor to motor it is almost impossible to implement this sort of regime.

There are two primary methods of obtaining parameters for the implementation of a feed-forward control scheme. If the system consists of physical or chemical principles that are well known and easily measureable, then an accurate model can be created whereby the feed-forward parameters can be accurately implemented. In the case of hybrid rocket motors, the complexity of the combustion process makes it almost impossible to construct a model accurate enough to provide precise tuning controls for

the feed-forward controller. In such a case, empirical data can be relied upon but this requires that data be gathered over a large range of possible scenarios and in varying conditions. Due to the cost and time involved, this is not a practical approach.
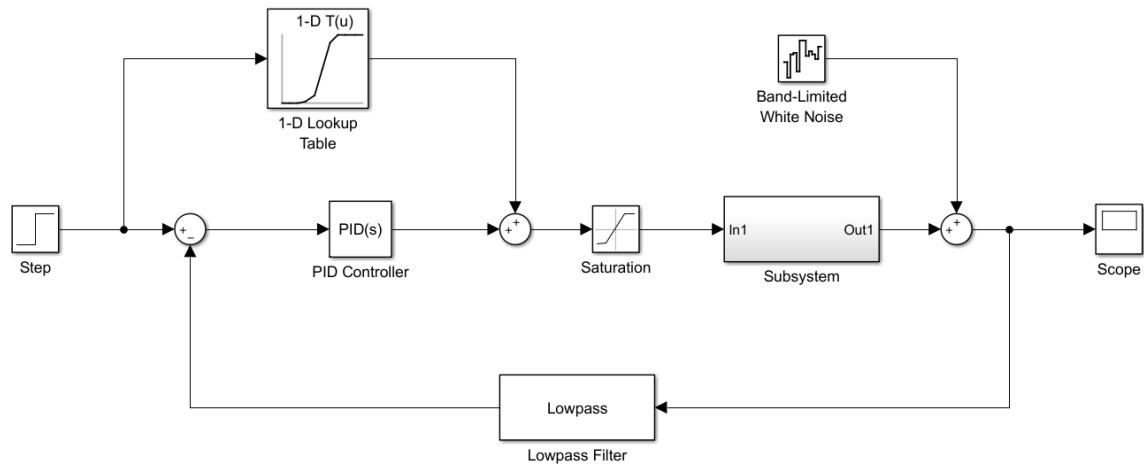
Figure 5.6: Schematic showing the possible configuration of the implementation of a combined feed-forward and weak feedback control regime.

A combination of methods is thus required to find appropriate control parameters. Using the model created to simulate the lab scale hybrid rocket motor, combined with data from the open-loop tests, reliable values were extracted for use in the feed-forward scheme of this study. In practice this still may not yield accurate control due to non-linearities inherent in hybrid motors and the ball valve flow characteristic. Ultimately, an appropriate mix of feed-forward and feed-back control provides the most robust control regime. Thrust and chamber pressure values were parameterized as a function of the angle of the valve and the closed-loop mechanism functions to further reduce error. Closing the loop around the error in valve angle would, in effect, cancel the non-linear relationship between valve angle and the effective port area.

When using a predefined control scheme, an alternate approach is to use coercion functions to move the valve angle quickly to a predetermined value that has shown, through open-loop testing, to result in the set point thrust. Due to the variability of hybrid rocket motors, using coercion functions in conjunction with a lookup table will provide the smoothest results since the valve will first be forced to a particular angle and then adjusted slightly by the PID controller. A similar principle could be applied by relaxing the input of the feed forward component, ultimately resulting in the same effect. Due to the fact that all tests were done with a predefined set-point profile, a coercion function was used to initially adjust the valve to an angle that produced the relevant thrust/pressure in the open-loop tests.

5.5 CONCLUSION

This chapter described the methodology used in obtaining viable control parameters using a combination of both analytical and graphical methods. A transfer function was first obtained using the mathematical model described in the previous chapter. This was compared to a transfer function obtained graphically by observing the rise time, settling time, steady state error and related parameters of previous hot-fire tests. A hybrid transfer function was made from these two methods that was further refined during testing to produce the final transfer function, from which controller constants were obtained. A feed-forward lookup table was implemented due to the non-linear flow characteristic of the ball valve.

6   OPEN-LOOP TESTING

6.1   INTRODUCTION

Ball valves have non-linear flow characteristics and therefore it was important that the control authority was determined first before performing closed-loop tests. The motor was thus fired for a short period until stability was reached - 1.5 seconds was deemed to be sufficient - and the valve was then slowly closed until the motor shut off. The angle of the valve was then compared to the thrust produced by the motor, thereby approximating the angle the valve must be set at to produce a particular thrust. This was also done to determine the control authority of the valve.

Open-loop testing was also carried out to measure the noise from the thrust load cell and to enable design of a filter for use with the controller. The test stand structural harmonic resonance was obtained from Fourier analysis and a low pass filter constructed with a cut off frequency below that of the harmonic frequencies.

6.2   TEST SETUP

A total of three tests were done using the open-loop control scheme. All tests were set up as described in Chapter 3 and parameters were changed according to the type of test carried out. In the first test the motor failed to ignite but still yielded usable results due to data obtained from the thrust produced by the nitrous oxide, while both the following tests worked as designed and produced satisfactory results.

Test 1

Table 6.1 shows the initial conditions and parameters programed into this test.

Table 6.1: Parameters for first open-loop test

Parameter	Value
Opening angle	90°
Time at open position	3.5 s
Set point	N/A
Final Valve Angle	0°
Time to close	6 s

The test stand was set up as required for a standard hot fire test. The only variable that changed for the open-loop test was the command sent to open the valve. Instead of opening the valve to its maximum position for a set time and then closing it again, the valve was commanded to open for 3.5 s to reach steady state and then slowly close over a period of 6 s. There was no feedback control and no other inputs or changes were made. The motor did not ignite but thrust measurements were taken and useful

data was acquired. After some investigation it was hypothesised that the potassium nitrate (KNO₃) igniter was wet and therefore did not create sufficient energy in order to successfully ignite the motor.

A non-negligible amount of thrust was produced by the flow of the oxidiser through the nozzle and therefore conclusions could be reached regarding the linearity and control authority of the control valve. Figure 6.1 shows the thrust produced by the oxidiser flow superimposed over the control command to the valve. From this graph it can be seen that initially (between 35.5 s and 38.5 s), the thrust produced by the free flowing oxidiser naturally decays after time. This is most likely due to the decaying tank pressure, causing a lower mass flowrate. After approximately 38.5 seconds there appeared to be significant change in the output thrust. This was when the valve was at about 45°. The measured thrust then appeared to decrease linearly until the oxidiser flow was shut off at 20°. Although the control authority and linearity could be estimated from the test, a successful open-loop hot fire test was still required to validate the parameters.
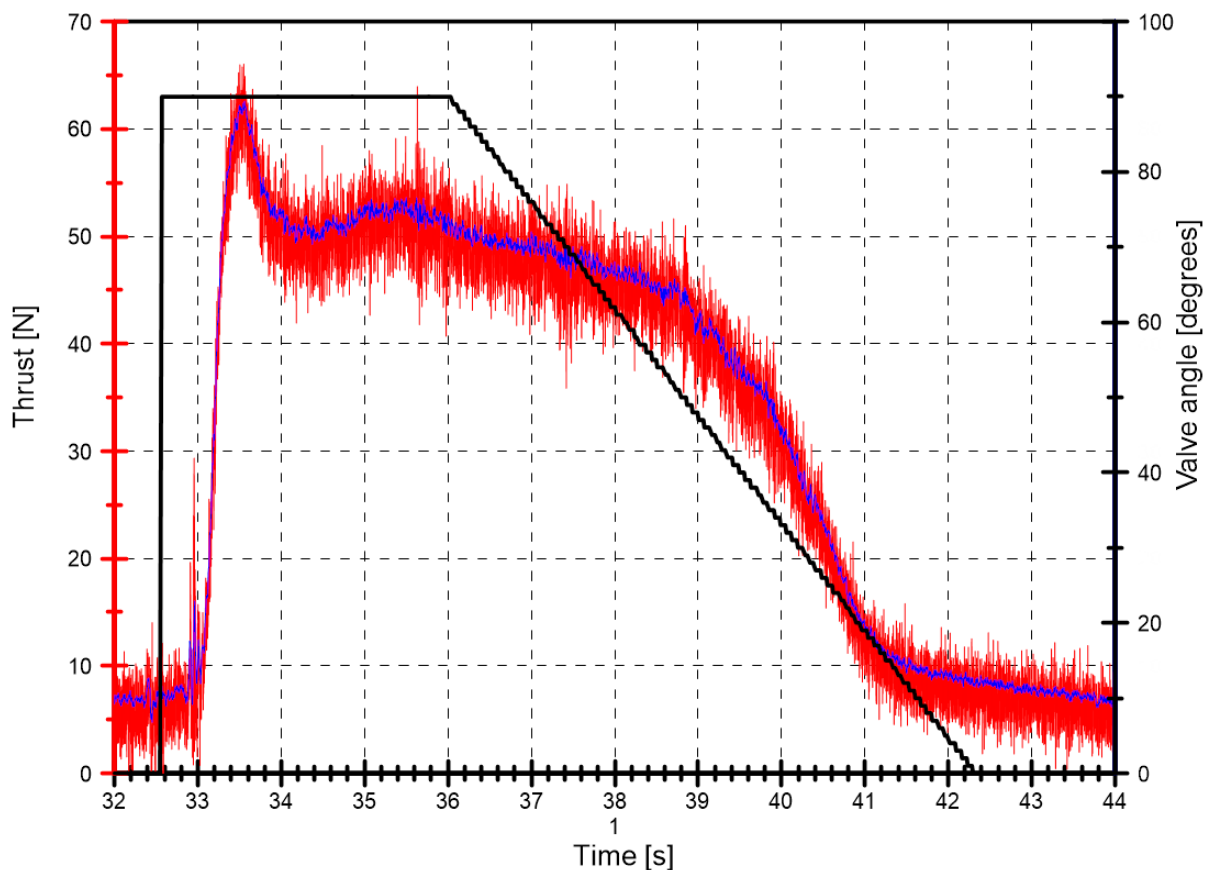

Figure 6.1: Relationship between valve angle and thrust produced from the nitrous oxide ejected through the combustion chamber out the nozzle. The blue series represents the filtered thrust.

Test 2

Table 6.2 shows the initial conditions and parameters programed into this test.

Table 6.2: Parameters set for second open-loop hot fire test.

Parameter	Value
Opening angle	90°
Time at open position	3.5 s
Set point	N/A
Final Valve Angle	0°
Time to close	6 s

The second test used the same control command as the first. The motor ignited and the test functioned as intended (opened for 3.5 seconds to reach steady state and then slowly closed over a period of 6 seconds).

Figure 6.2 shows the thrust output of the second open-loop hot fire test alongside the valve angle command output. Two things were observed. First, the valve took almost a second to respond to the command to open; second, the thrust had a value of approximately 0 N before the test and about 50 N after. The first issue was probably due to the valve "sticking", that is, the actuator is unable to properly overcome the static friction inside the valve and does not respond to the input torque of the servo motors. The second was most likely due to the initial jolt of the motor shifting the load cell out of place slightly. Regardless, the parameters of interest were not significantly affected and reasonable conclusions could be drawn.

It was noted that, again, the thrust was only significantly affected when the valve was at approximately 65° and the motor completely shut off at around 45°. This was in line with the predictions laid out by the first failed test. However, during this test, it was noticed that the decrease in thrust was not linear with the decrease in valve angle. It was theorised that this was due to the inherent flow nonlinearity of ball valves.
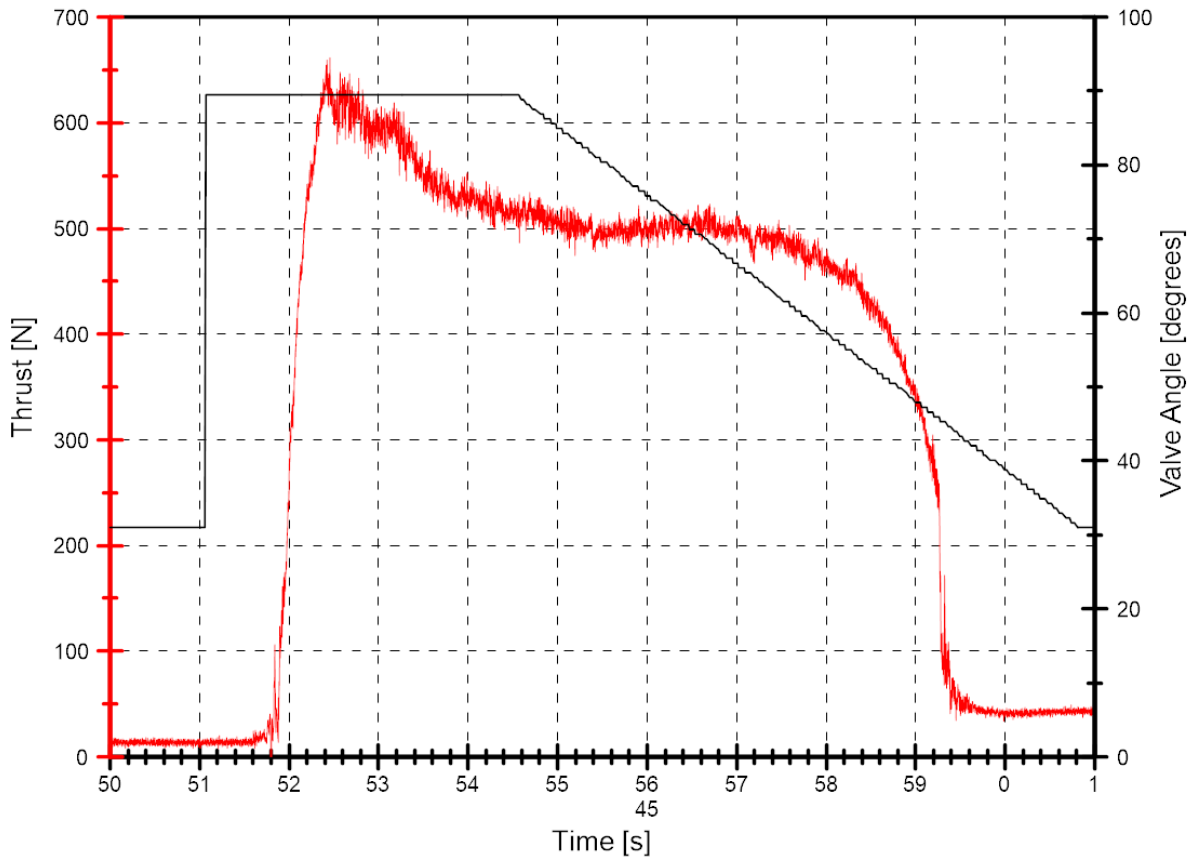
Figure 6.2: Thrust produced over time versus valve angle.

Test 3

A third open-loop test was carried out but with different parameters to more accurately portray the control authority of the valve. Parameters are tabulated in Table 6.3.

Table 6.3: Initial conditions and parameters set for the third open-loop hot fire test.

Parameter	Value
Opening angle	90°
Time at open position	3.5 s
Set point	N/A
Intermediate Valve Angle	55°
Final Valve Angle	25°
Time to close	4 s

Due to the narrow control authority range and difficulty in accurately determining thrust versus valve angle, one more open-loop test was done with emphasis on the estimated range of control. A command profile was inputted where the valve was to open fully for a short time to establish stability, close

66

quickly to the upper end of the estimated control range (65°) and then close slowly to the lower end (45°). Five degrees were added on to the estimated upper range in the event the motor started throttling at a valve angle slightly higher than predicted, and five degrees were added to the lower end of the range to ensure the motor did not move into the unstable region and cause damage to the components. Therefore, the open-loop test commanded the valve to open for three seconds, close quickly to 65° and stay there for a second, and then slowly close to 45° over a period of four seconds following immediate shut off.
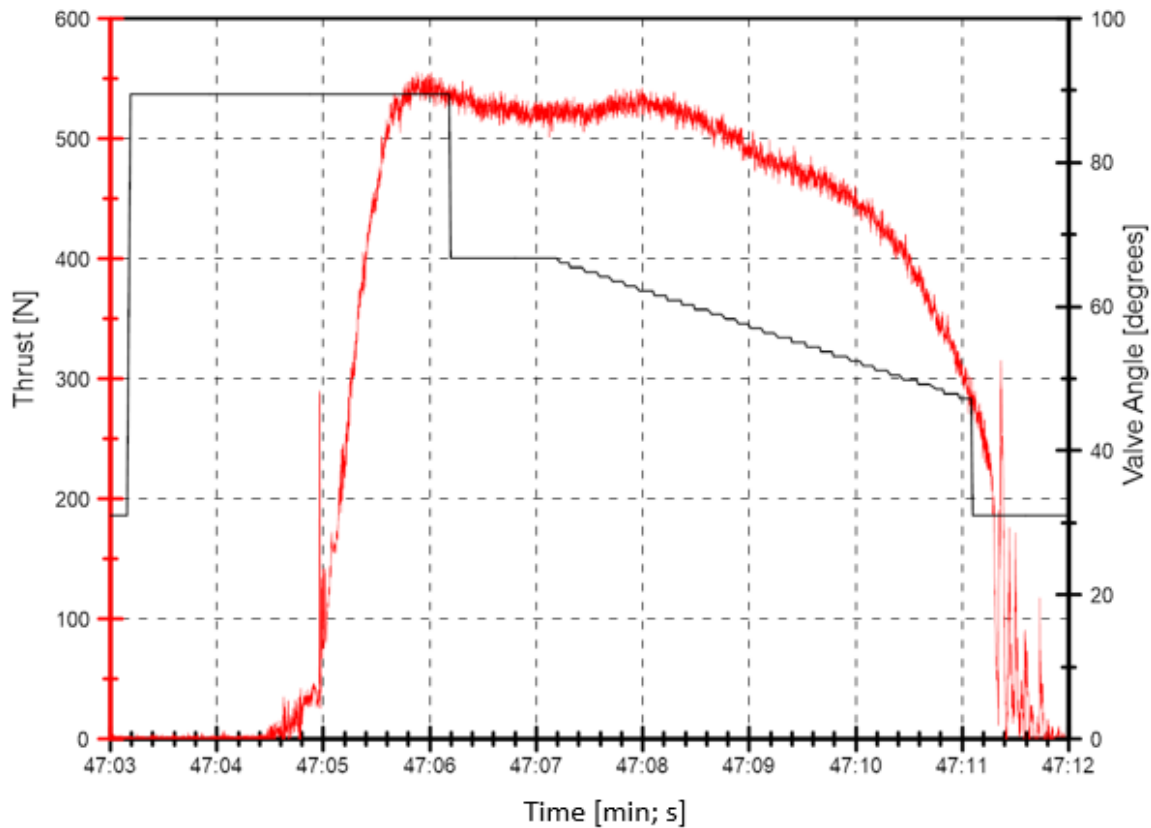
Figure 6.3: Valve angle versus thrust showing delayed valve angle closing

As seen in Figure 6.3, the thrust is only noticeably affected after 65° when the thrust was at approximately 550 N. Thereafter the thrust decreased linearly to about 450 N, which corresponded to a valve angle of about 50°, after which the thrust dropped to just under 300 N when the valve was at 45°. It was hypothesised that between the 50° to 65° range, the thrust will behave linearly, and between the 45° to 50° zone, the thrust will vary greatly with small corresponding changes in valve angle. This seems to correlate with non-linear relationship of ball valve angles versus mass flowrate. A large time delay of almost two seconds could still be seen between the valve open command and the start of the motor.

6.3   PRESSURE DROP ACROSS THE VALVE

Thrust in the motor is modulated by varying the oxidiser flowrate using a full bore ball valve. This modulating action causes a pressure drop across the valve which was of interest for determining the limits of throttlabilty and the effect of cavitation on thrust produced. Due to the nonlinear nature of flow through ball valves, the flow characteristics and data obtained from open-loop tests will be important for future tests involving ball valves for throttling. Figure 6.4 shows the pressure drop through the valve for test 3 and indicates that where the pressure drop rises above zero, the thrust decreases correspondingly. This serves to reinforce the prediction that the thrust can be regulated through the modulation of the oxidiser flowrate. Also noticeable is that from 90° to 50° the pressure drop does not rise significantly and so the thrust does not drop for that region of the ball valve angle.
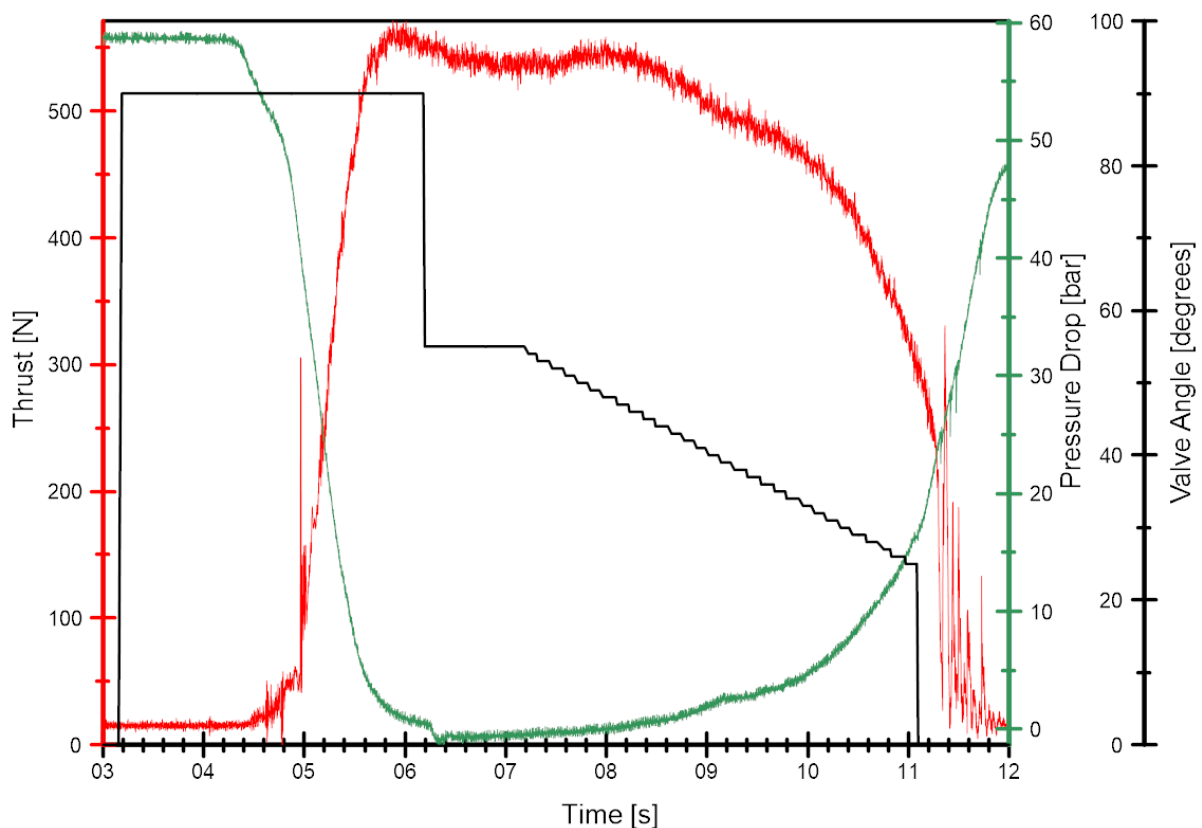
Figure 6.4: Relation between pressure drop through control valve and produced thrust

6.4   RESULTS AND CONCLUSION

Results from tests 1 to 3 showed that there is no appreciable effect on the thrust produced by the motor from a fully open valve position of 90° to 50°. There are several possible reasons for this. First, in that range there is excess oxidiser with a portion of it not reacting in any noticeable way and thus only when the oxidiser is throttled sufficiently does the O/F ratio change enough to affect thrust output. This theory is bolstered by the graph in Figure 6.3 which shows a small increase in thrust just before the motor begins throttling down, indicating the possibility of an optimum O/F ratio at that point. Secondly, the

68

mass flowrate through the feed line is possibly too high for the injector and so only when the mass flowrate is significantly reduced is the pressure drop across the injector small enough to affect a change in thrust output.

It is possible to define a relationship between the valve angle and the thrust produced by the motor. This is useful for inputs that are non-linear in nature such as the angle of the ball valve and the flowrate it permits. From a control design perspective, it is simpler to establish a relationship between the valve angle and thrust produced and then create a feed forward component for the controller using a one dimensional lookup table. Such a table was developed from the results acquired during open-loop testing and is shown in Table 6.4. The measured thrust values are rounded up to the nearest 10 N since a higher degree of precision is not required and not easily measured. The results also provide the "throttle range" within which the motor's generated thrust can be safely modulated. This is predicted to be between 500 N and 300 N; as a precaution a more conservative range of 310 – 490 N was selected.

Table 6.4: Valve angle versus produced thrust as predicted from the open-loop tests.

Valve Angle	Measured Thrust
90°	530 N
65°	530 N
55°	490 N
50°	400 N
45°	300 N

The primary advantage gained from using the lookup table is that the speed of the controller as well as the accuracy is greatly increased. With the feed-forward component the controller has a means to arrive quickly at the desired thrust with only small changes needed to achieve a high degree of precision. However, the fact that the oxidiser feed system uses the blow-down method produces the problem of decaying oxidiser flowrate as the pressure in the run-tank decreases. Thus, the valve angle to produced thrust varies over time, albeit by a small amount. Coupled with the fact that hybrid rocket motor thrust is inherently transient, a feedback component is still necessary for the controller to ensure the motor produces the thrust commanded. The closed-loop testing described in Chapter 7 utilized the feed forward lookup table along with the feedback loop to assess the viability of the control scheme.

7 CLOSED-LOOP TESTING

7.1 INTRODUCTION

The primary objectives of closed-loop testing were the evaluation of the designed control scheme as well as to determine the viability of throttling liquefying-fuel hybrid rocket motors in general. All the closed-loop tests that were performed were hot-fire tests.

7.2 TEST SETUP

The physical setup for closed-loop testing remained the same as for open-loop testing, as the only element that was changed was the way in which the LabVIEW™ program interacted with the physical components. Water cooling of the nozzle was not employed for closed-loop testing since much lower temperatures were reached compared to motors that contain metallic additives (Maharaj, 2018). Previous hot-fire tests using pure paraffin wax did not degrade the nozzle in any way, even after prolonged, repeated burning, so the implementation of cooling methods was deemed unnecessary.

On the controller, limits were set such that the valve angle could not drop below 48° to avoid induced instabilities. In addition, the program was configured to completely close the valve after a specified time, regardless of controller behaviour for safety reasons. This was set as a separate, over-riding code.

7.3 RESULTS

Several tests were conducted with the first three failing to meet their prescribed test objectives. All three failings were attributed to controller error or user input error. The final three tests showed positive results with the controller modulating the thrust to track the prescribed set point as predicted. The detailed results from ten hot-fire tests are given in the sections that follow.

Test 1

Table 7.1 shows the controller parameters and other initial conditions for the first closed-loop test.

Table 7.1: Controller parameters for test 1.

Parameter	Value
Opening angle	90°
First set point and duration	490 N for 3 s
Intermediate set point and duration	310 N for 3 s
Final set point and duration	490 N for 4 s
Proportional Gain [P]	1.750
Integrative Gain [I]	0.010
Derivative Gain [D]	0.004

The first test was run with no feed forward control at all; only the feedback loop was used to coerce the thrust to the desired value. The thrust command variable was as follows: valve fully open for one and a half seconds to attain stability, throttle down to 490 N for three seconds, throttle down further to 310 N for three seconds, throttle up to 490 N for four seconds and then close the valve. The motor ignited successfully however the control system did not work as designed and behaved erratically, as can be seen in Figure 7.1. Again, the black data set represents the valve angle command variable, the red data set is the thrust measurement in Newtons, and the blue line represents the desired thrust profile.

Figure 7.1: Valve angle and set-point profile superimposed over measured thrust

The first stage of the test behaved as predicted; the valve opened fully to 90° and remained there for one and a half seconds. That duration was chosen as the servo motors take just over 0.7 seconds to fully open the valve and, previous tests showed that half a second is all that is required for the system to be adequately stable for throttling. After the first stage it is apparent that the control system reacted erratically with the control output oscillating rapidly. It can be seen, however, that the thrust output still throttled down to approximately 490 N. Thereafter the controller failed to reduce the thrust down to the specified 310 N with the controller output remaining somewhat constant. At the final stage of the burn the motor once again failed to produce the desired thrust. However, this was not a controller fault, since the valve was set to the maximum position. Instead, the motor simply could not produce enough thrust to meet the targeted value.

71

The first observation to be made is that the thrust values before and after the burn are different with the final value about 50 N higher that the initial. This mirrors previous observations and highlights a recurring issue that requires attention. If the thrust values shift from initial values, then there is a possibility of the controller receiving measurements that are out of the set boundary limits. The erratic response of the controller suggested that the noise on the input signal to the controller was interfering with the controller response. Typically, the derivative function is omitted when the input signal is noisy due to unpredictable response typically resulting in "servo jitter", whereby the servo motors behave erratically as seen in the controller output in Figure 7.1. This was accounted for by setting a low sample rate for the controller but still did not produce an acceptable result. Based on this result, the derivative function was left out in all remaining tests.

Test 2

Initial conditions and controller parameters are shown in Table 7.2.

Table 7.2: Controller parameters for the second closed-loop control test

Parameter	Value
Opening angle	90°
First set point and duration	480 N for 3 s
Intermediate set point and duration	310 N for 3 s
Final set point and duration	480 N for 4 s
Proportional Gain [P]	1.750
Integrative Gain [I]	0.010

The first closed-loop test did not operate as intended, therefore, a second hot fire test was run with improvements made to the controller. The derivative component of the controller was removed and the sample rate was lowered further. The test setup was the same as before with only the PI parameter values and controller sample rate altered. Although this test did not perform as expected and the results were sub-par, the controller output was much improved with no noticeable servo jitter and far more coherent commands, as seen in Figure 7.2. The thrust profile was set to the same as the previous test but with the change of the upper limit from 490 N to 480 N. Therefore, the valve was set to open to 90° for one and a half seconds, throttle to 480 N for three seconds, throttle to 310 N for three seconds, back up to 480 N until the total allowed burn time is reached.
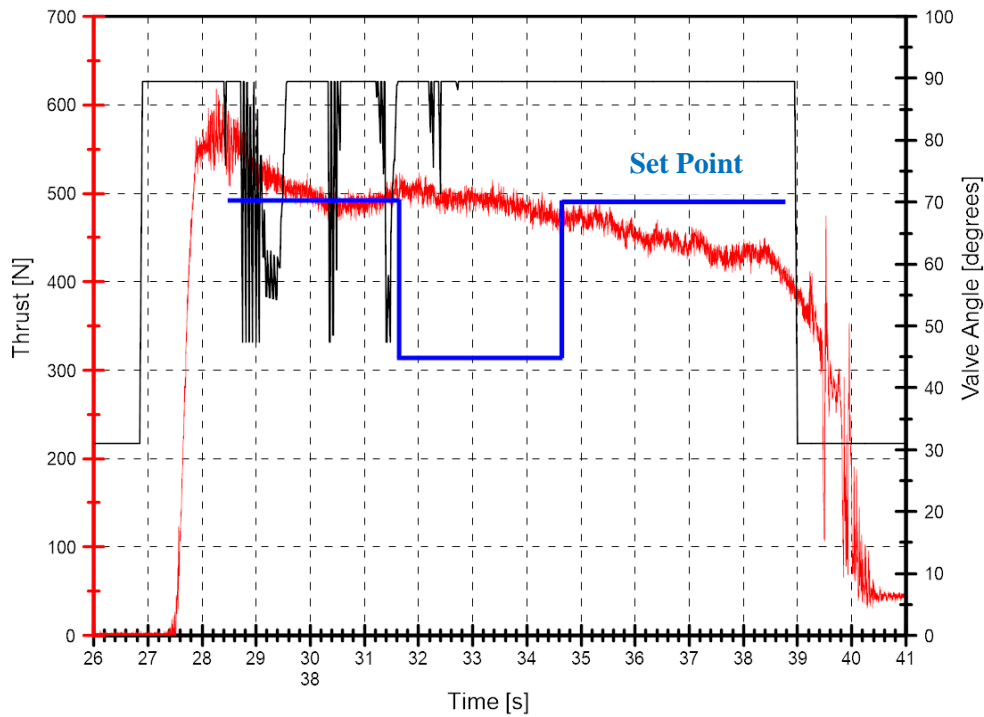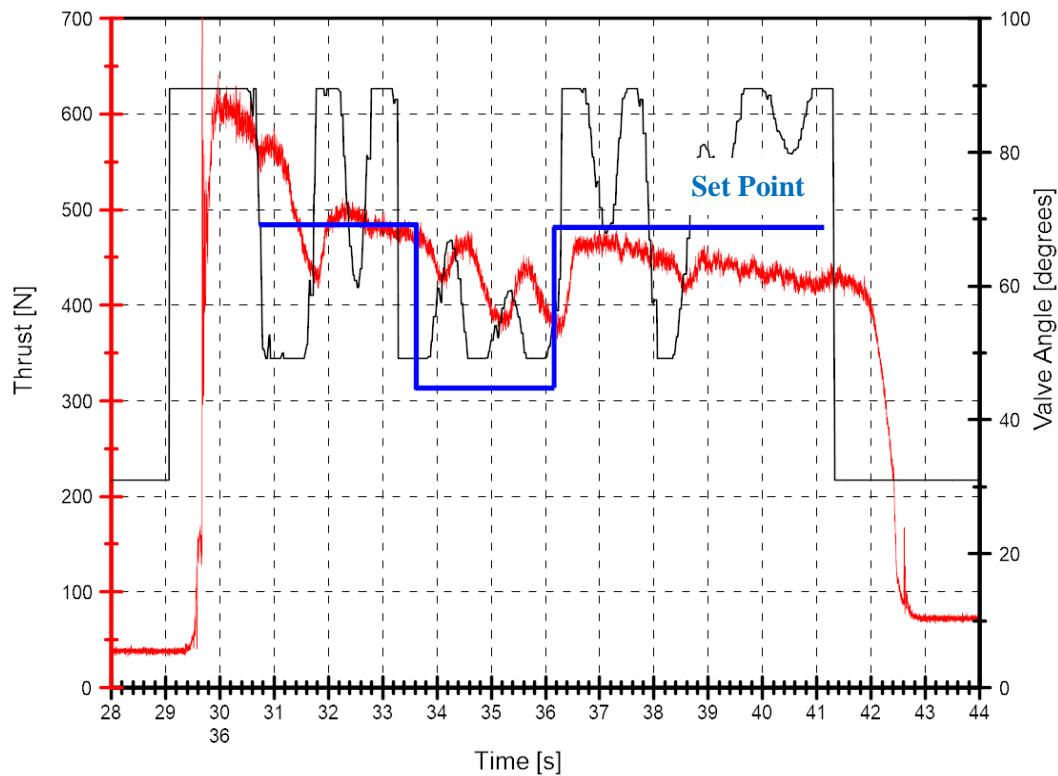
Figure 7.2: Valve angle and set-point profile superimposed over measured thrust

The first stage of the profile worked as expected; the valve opened to maximum and remained there 1.5 s. The controller then attempted to throttle down to 480 N which elicited a quick response showing a significant amount of undershoot followed by oscillations in the controller output, as the controller attempts to maintain the prescribed thrust level. These types of oscillations are typical in control schemes that do not use a derivative component. In the third stage, the command was given to throttle down to 310 N. The controller immediately signalled to move the valve to the lowest allowed angle, however the motor seemed reluctant at this stage to respond to the given inputs. In the fourth and final stage, the command is given to throttle the motor back up to 480 N but as Figure 7.2 shows, the natural thrust decay of the motor once again caused the maximum possible thrust to be below that of the thrust demanded.

These results raised the suspicion that the valve angle limit, set at 48° was not low enough. A thrust level lower than 350 N could not be achieved despite the valve operating at the lower boundary limit. Also, the initial and final thrust readings were again shifted up by approximately 50 N. This test confirmed that the shift in thrust affected the controller response by more than initially thought, and adjustments were made to account for this in further tests.

There was uncertainty regarding the limits of throttlabilty, and so a test was designed with feed forward commands to follow the same square wave format but with the maximum valve angle set to the valve

73

in the fully open position, and the minimum at the lowest angle feasible. This was intended to establish the absolute margins for throttling and the acceptable safety margins that could be implemented while still allowing for significant throttling.

Test 3

Table 7.3 shows the parameters set for the open-loop test to determine the maximum and minimum thrust values possible.

Table 7.3: Valve angle parameters for open-loop hot fire test

Parameter	Value
Opening angle and duration	90° for 3 s
Intermediate angle and duration	43° for 3 s
Final angle and duration	90° for 3 s

The aim of the third test was to establish the acceptable thrust limits that could be imposed on the controller. The intention was to remove ambiguity regarding limits placed on the valve and, in addition, to see how the thrust decay of the motor affected the maximum attainable thrust. Parts of this section are taken from the conference paper "Safety Aspects of Nitrous Oxide Use in Hybrid Rocket Motor Design and Testing" presented at the 2018 Joint Propulsion Conference of the American Institute of Aeronautics and Astronautics (AIAA) in Cincinnati, Ohio (Velthuysen et al., 2018).

The test resulted in a major equipment failure and bursting of an oxidiser feedline which caused the LabVIEW™ program to shut down abruptly. Data from the last few seconds of the test were thus not recorded as illustrated in Figure 7.3. Regardless, the test still provided useful and usable data for the next set of experiments. The natural decay of thrust for the first stage of the test was recorded and could be extrapolated to find the upper bounds of obtainable thrust. The test also showed the absolute minimum the thrust could be throttled down to before instabilities occur and the motor shuts down.
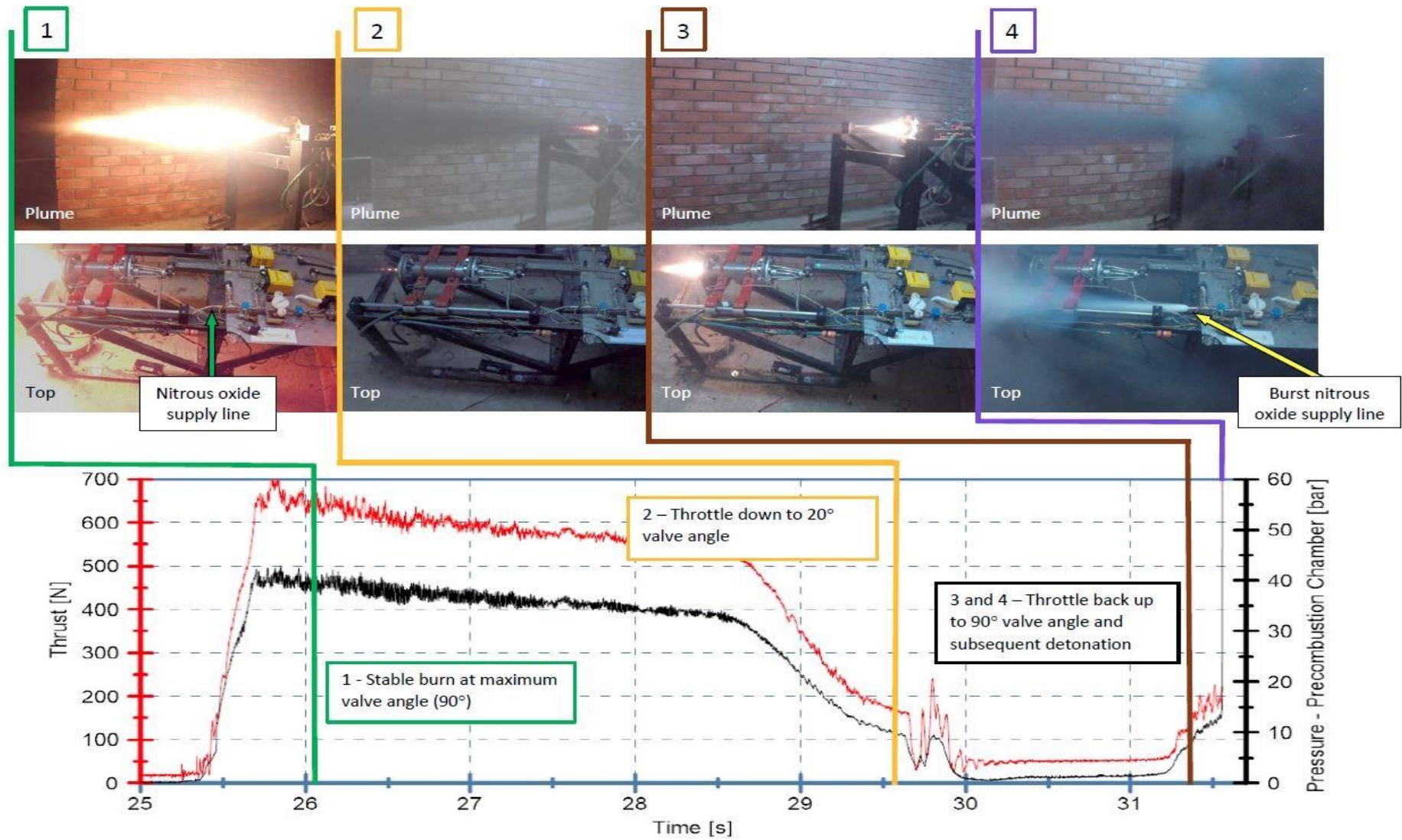
Figure 7.3: Graphic showing overpressurization event and relevant data obtained

The first stage of the test showed a stable burn with the measured thrust reaching almost 700 N and decaying to about 550 N over a period of 3 seconds. Thereafter the valve was commanded to close to 43° and stay there for three seconds before opening up again to 90° for the final three seconds of the test. During this stage the measured thrust dropped to just over 150 N about 1.7 seconds after the valve was required to move to 43°. The motor then showed signs of instability for a short period and then appeared to shut off. When the valve was commanded to open again, the flexible oxidiser feed line ruptured and the LabVIEW™ program completely shut down, stopping all data acquisition after that point, as can be seen in Figure 7.4.

Video footage suggests that combustion did continue during the unstable period but due to a fluctuating pressure before the injector, some wax was forced back through the injector causing combustion to take place inside the feedline. Wax was found on the entrance side of the injector which supports this conjecture. Almost immediately following the valve opening, a decomposition event is thought to have occurred forcing the braided hose to burst, with the subsequent shock turning off all electronic equipment and damaging the throttling valve and pressure sensor on the line.
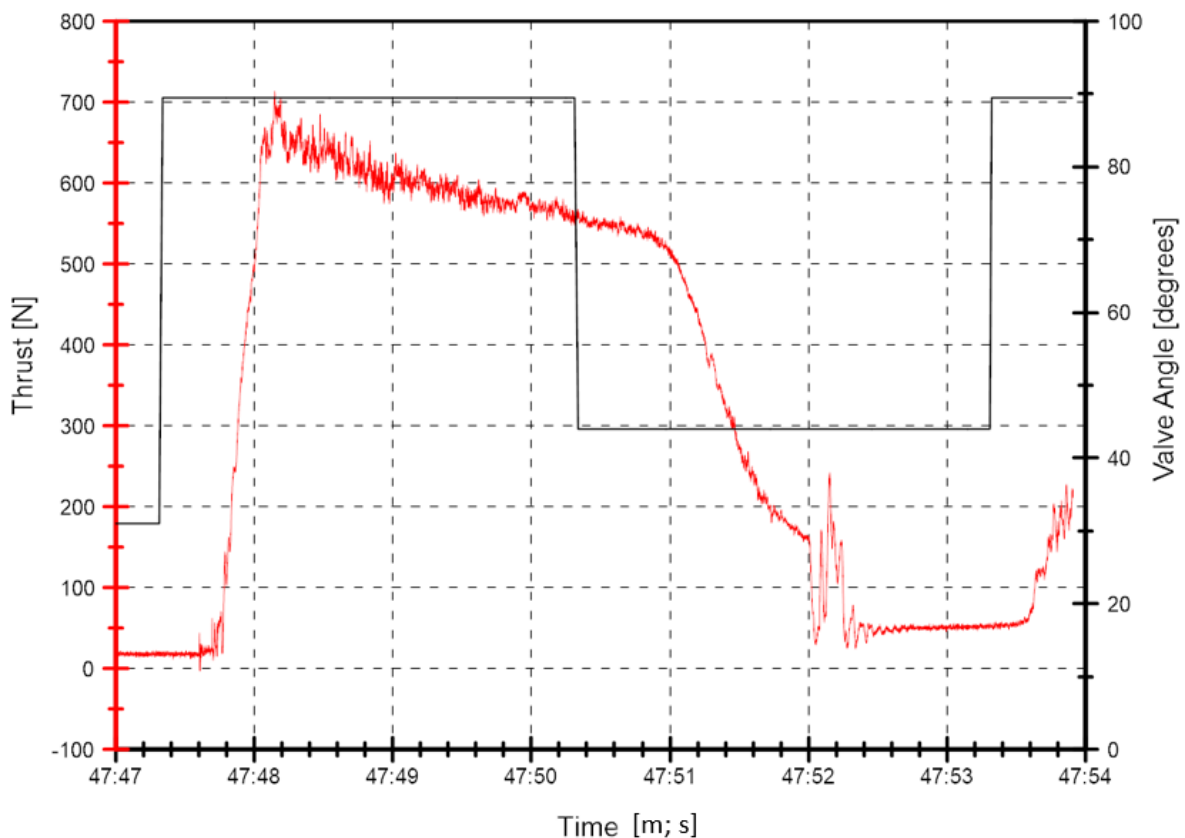

Figure 7.4: Thrust and valve angle versus time for an open loop test that resulted in an overpressurization event.

76

Despite this failure, useful information was obtained, especially regarding the limits of motor throttling. Due to this test, a limit was set on the lowest permitted valve so as to avoid instability. In addition, the thrust decay was extrapolated and so an upper limit of thrust could be set ensuring the motor always achieves the commanded thrust value.

Test 4

This test aimed to establish the accuracy and sensitivity of the controller. The initial conditions and parameter values can be seen in Table 7.4.

Table 7.4: Set points, controller parameters and initial conditions of Test 4.

Parameter	Value
Opening angle	90°
Initial set point	400 N
Intermediate set point	300 N
Final set point	400 N
Proportional Gain [P]	1.75
Integrative Gain [I]	0.015

In test 4, the controller was instructed to reach a set point of 400 N, then 300 N and finally back down to 400 N. It was concluded that 300 N was the minimum thrust level the motor should be instructed to track to avoid instabilities, meaning the thrust turndown ratio would be 1.67:1. This was a relatively small range for the motor but is sufficient to satisfy the aims of this experiment. Figure 7.5 shows the valve angle dipping below the allowable amount, subsequently cutting off the oxidiser flow and therefore stopping the motor. This was due to an error in the software which was corrected before the following test. When the valve reopens, the thrust increase is due to the N_2O passing through the combustion chamber generating a low level of thrust.
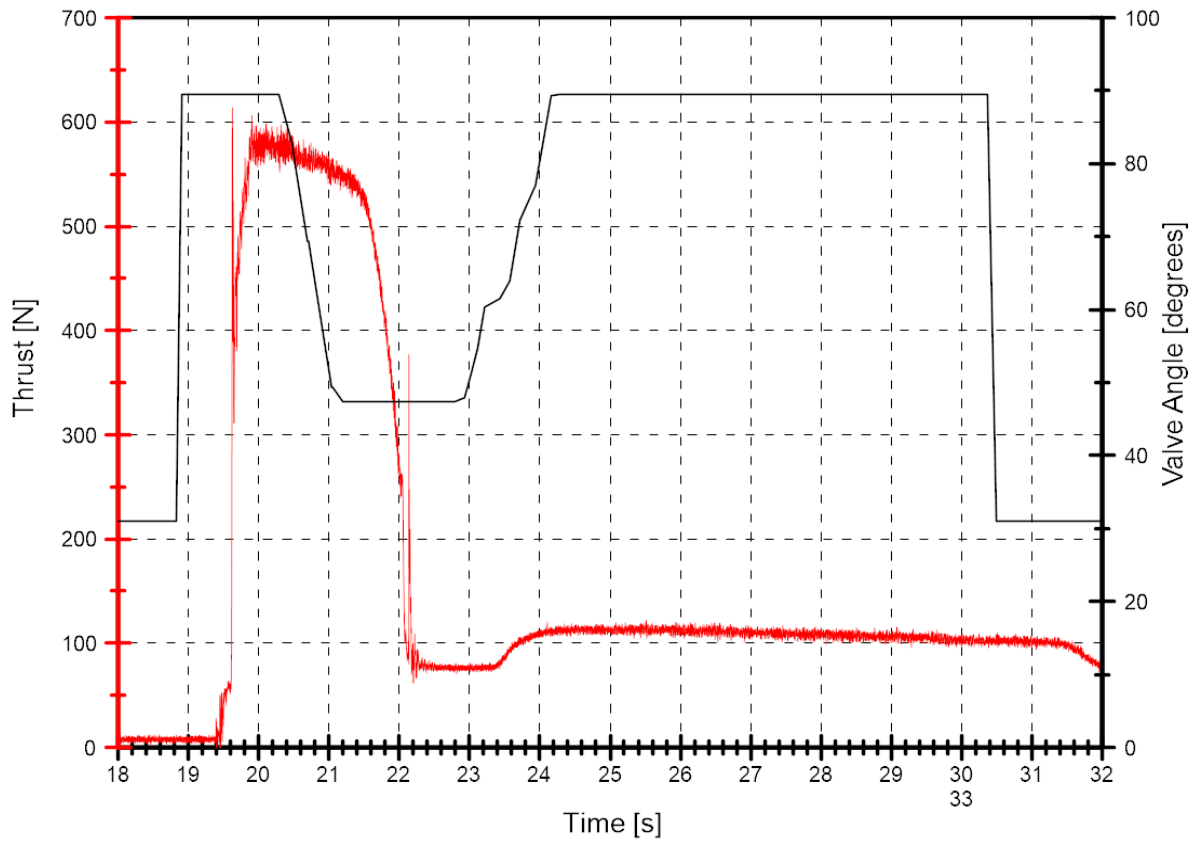
Figure 7.5: Thrust produced vs the valve angle achieved. Note that the valve angle dips to 45°.

Test 5

The objective of this test was to investigate the minimum required oxidiser mass flowrate. Parameters are shown in Table 7.5

Table 7.5: Parameters for mass flowrate test.

Parameter	Value
Opening angle	90°
Intermediate valve angle	46° until end of test (7 seconds)

The previous test experienced a premature shutdown of the motor and as such the valve was limited to close to a pre-set angle. In support of this, the valve was modelled in a CAD package to predict when the valve would be closed to an acceptable degree. It was observed that the valve closes at just under 44°. In order avoid another motor shutdown incident, the valve was not permitted to close to under 46°. The controller settings were left mostly unchanged. As seen in Figure 7.6, after the valve closed to 46°

there was no noticeable change in the thrust save for a steady decrease from about 550 N at the start of the burn to about 450 N at the end of the burn. There was no change in thrust after the valve closed to half its fully open position, and this suggests that the flowrate of the oxidiser feed system was originally designed incorrectly. If the O/F ratio is very high and then reduced by even a considerable amount, there may be no visible change in thrust output.
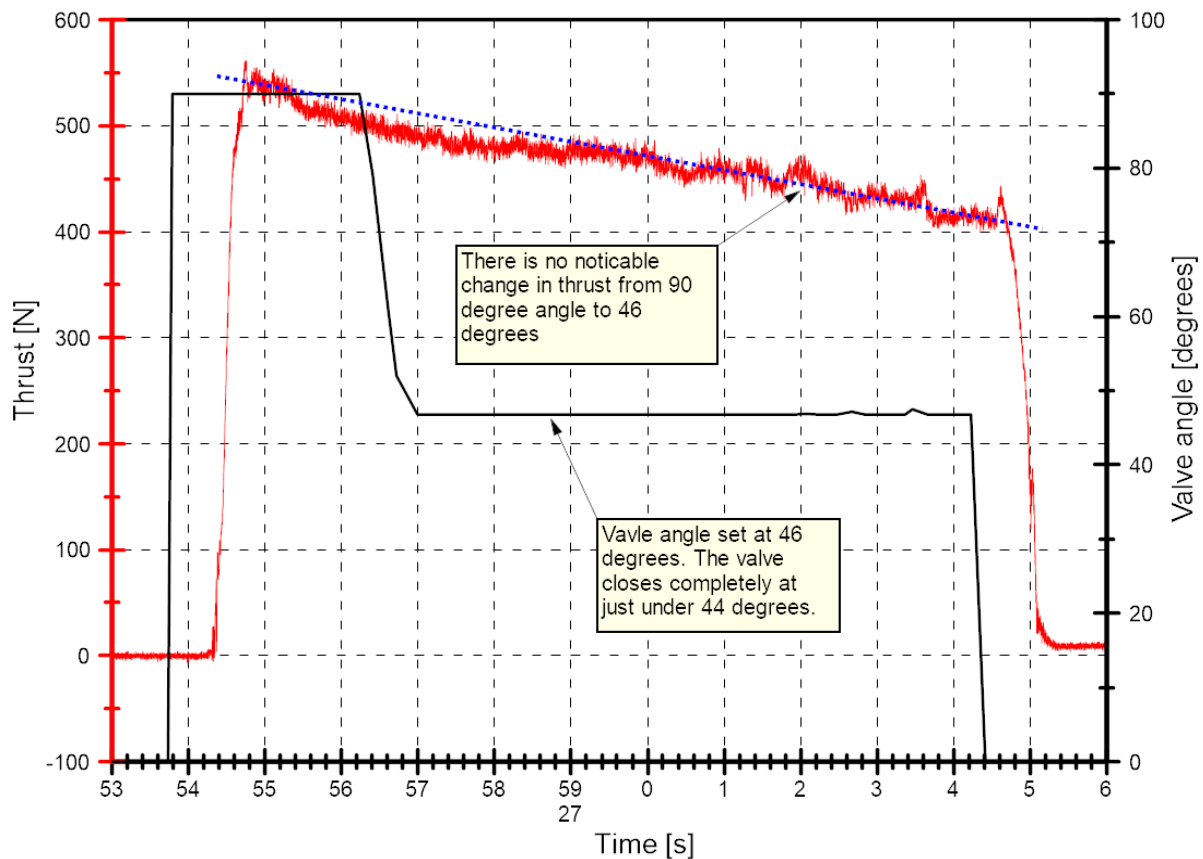
Figure 7.6: Measured thrust and valve angle versus time

7.4 NEW INJECTOR DESIGN

Further investigation showed that the oxidiser mass flowrate was approximately 0.212 kg/s on average as illustrated on Figure 7.7. As part of this study NASA CEA™ and MATLAB™ were used to determine that the motor needs only 0.125 kg/s on average to maintain a thrust of 350 N and an O/F ratio of 6.8. The injector was therefore redesigned such that the maximum allowable mass flowrate was 0.150 kg/s.

Figure 7.7: Tank mass over time for old injector

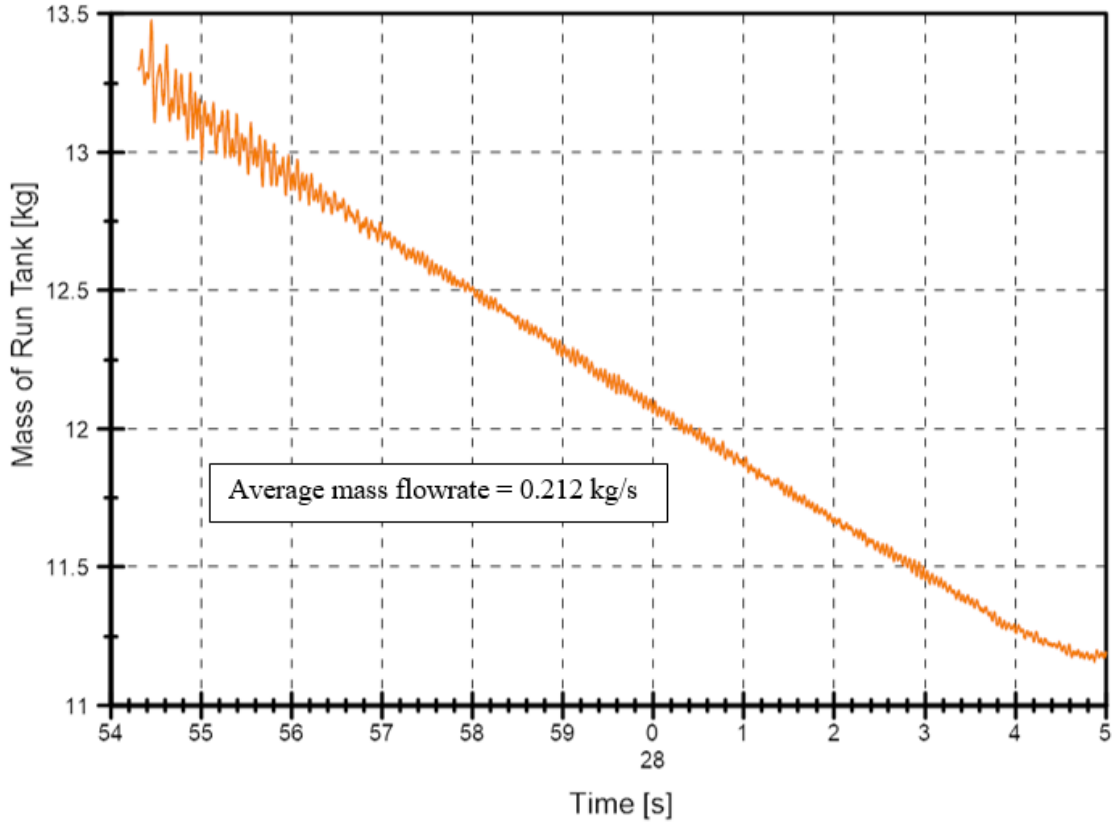Using the Homogenous Equilibrium Model (HEM) and values for enthalpy from REFPROP™, the injector was redesigned with five holes of 1 mm diameter, with each hole having a length of 10 mm to ensure adequate cavitation of the nitrous oxide and to prevent combustion instabilities. Two injectors were designed and manufactured, one with a maximum of 0.120 kg/s at initial conditions and another at 0.160 kg/s. The HEM model assumes that the flow is isentropic throughout and that the fluid in the pressure vessel outflows through a pipe that is much smaller than the vessel diameter. This is consistent with the design of the hybrid rocket motor injector used in this study. The mass flowrate through the injector can then be calculated as:

$$\dot{m}_{HEM} = C_d A \rho_2 \sqrt{2(h_1 - h_2)} \tag{7.1}$$

where $\dot{m}_{HEM}$ is the mass flowrate though a single hole or port of the injector as calculated by the HEM model, C_d is the coefficient of discharge through the injector which was estimated to be 0.8 in this instance, A is the cross-sectional area of a single port in the injector, ρ_2 is the density of the vapour/liquid mixture at the injector exit and h_1 and h_2 are the enthalpies of the vapour/liquid mixtures at the start and end of the injector respectively. Using the REFPROP™ package, and the equations of

state for nitrous oxide therein, the calculation of the mixture properties at the injector exit are easily obtained. Literature suggests that the critical mass flowrate for short tube injectors is significantly under predicted using the Homogenous Equilibrium Model, likely due to non-equilibrium effects (Waxman, 2014). To reduce these inaccuracies as much as possible, the L/D (length of injector port divided by its diameter) was designed to be high enough to ensure enough time for the fluid to reach thermodynamic equilibrium (Henry and Fauske, 1971). Using a value of 10 for the L/D ratio, and Equation (7.1) to find the area of each individual port, two injectors were designed and manufactured out of brass bolts. The old and new injectors are shown side by side in Figure 7.8.
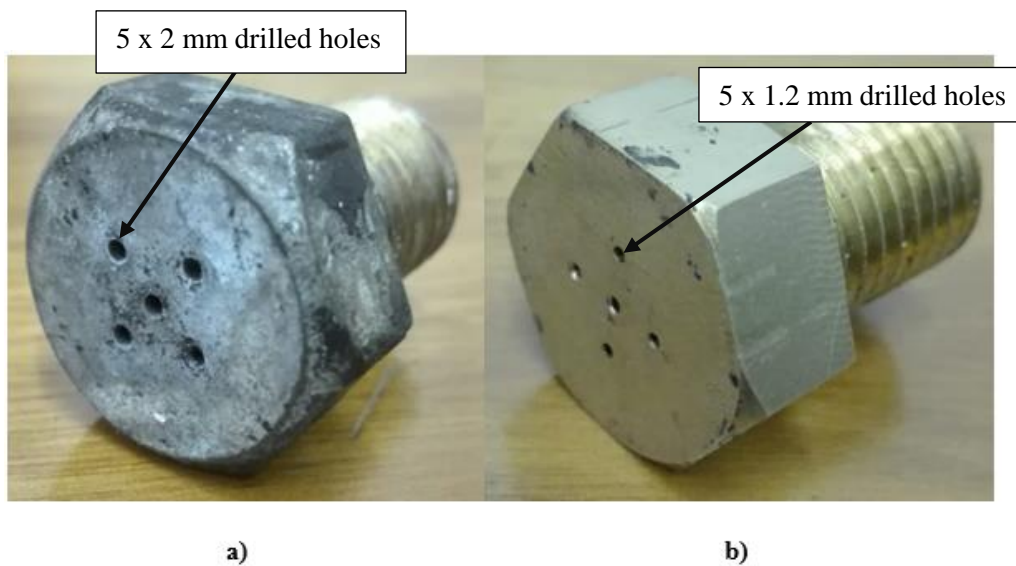

Figure 7.8: Illustration of a) previous injector designed for a mass flowrate value that proved to be too high, and b) new injector design using REFPROP and the Homogenous Equilibrium Model

Brass was chosen for the injectors due to its compatibility with nitrous oxide and machinability. Prior to machining, the bolt faces of the hex head were machined such that they are parallel to the axis of the bolt. The ports were drilled out using a 1.2 mm cobalt drill bit while a 10 mm drill bit was used to drill out the back, as can be seen in Figure 7.9. A 10 mm end-mill was then used to flatten the bottom out. The ports were chamfered on the inside using a 2 mm drill bit. A full detailed drawing of the injectors can be found in Appendix B.
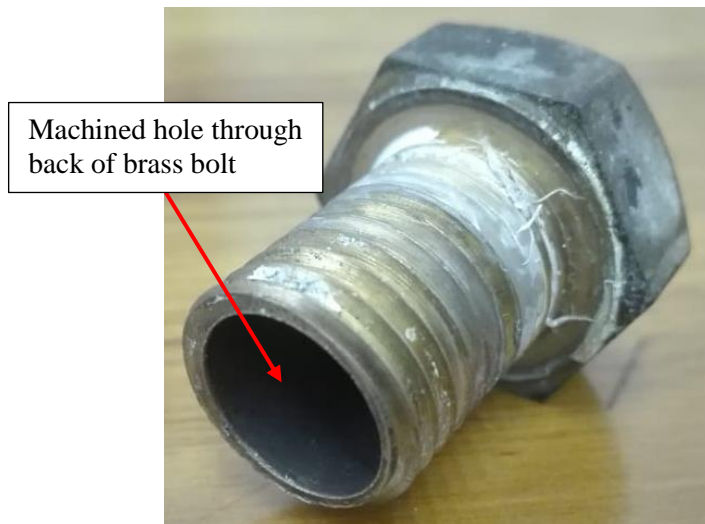
Figure 7.9: Rear view of the injector after machining

During testing, the first injector caused combustion instabilities, probably due to the flowrate being too low. The second injector, with six port each of 1.2 mm diameter, was then tested and found to provide a flowrate of 0.132 kg/s on average. It produced a stable level of thrust and was implemented in all further testing. The weight of the tank for the duration of the burn using this injector is illustrated in Figure 7.10.

Figure 7.10: Mass of the run-tank after installation of new injector

Test 6

The aim of Test 6 was to determine the minimum allowable valve angle for the new injector. Parameters are shown in Table 7.6.
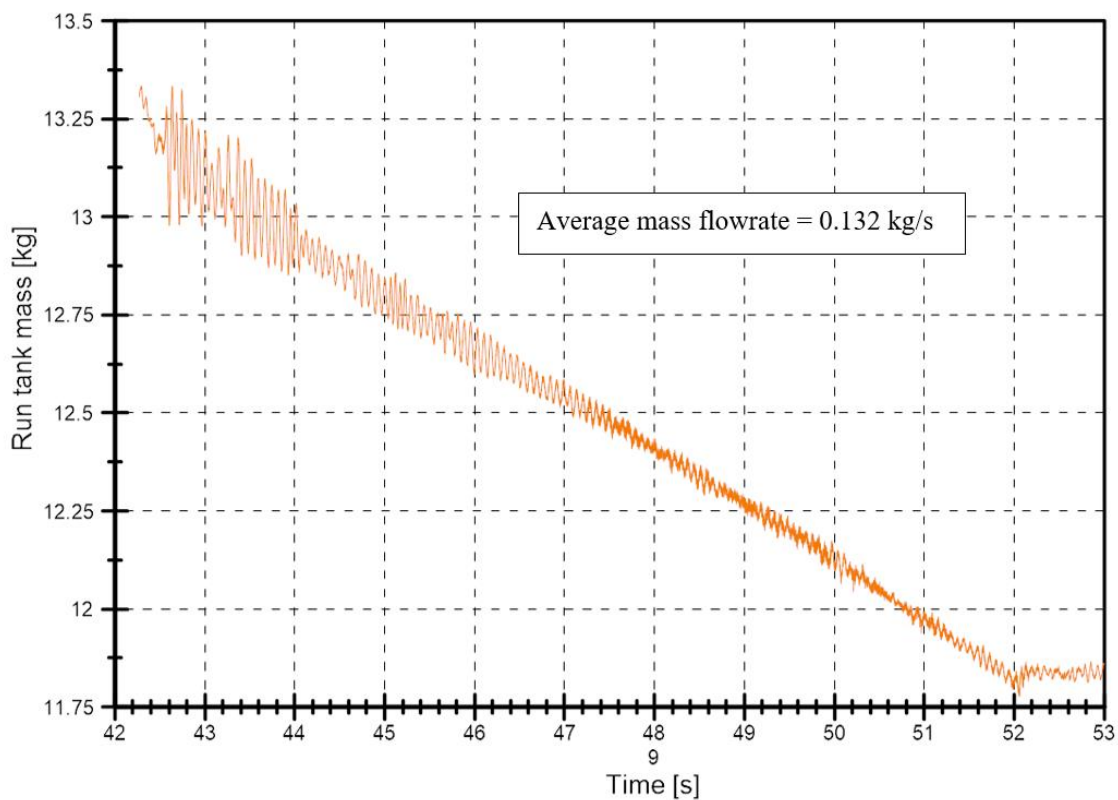
Table 7.6: Controller parameters and thrust set point

Parameter	Value
Opening angle	90°
Set point	300 N
Proportional Gain [P]	1.25
Integrative Gain [I]	0.015

A new injector was designed and tested and so a sixth closed-loop test was done with only minor modifications to the controller limits. Based on previous tests, the motor was predicted to burn stably at around 300 N. The controller set point was then set to 300 N with an additional safety mechanism to prevent the motor from attempting to restart once shutting down. This safety mechanism closes the valve were the thrust to dip below 200 N. This prevents the controller from attempting to open the valve if the motor cut out, thereby preventing an over-pressure event as recorded in Test 3. As seen in Figure 7.11, although the valve closed to its minimum allowable position, this did not create a large enough pressure drop to reduce the oxidiser flowrate enough to reach the prescribed set point. The lower valve angle limit was therefore lowered further.
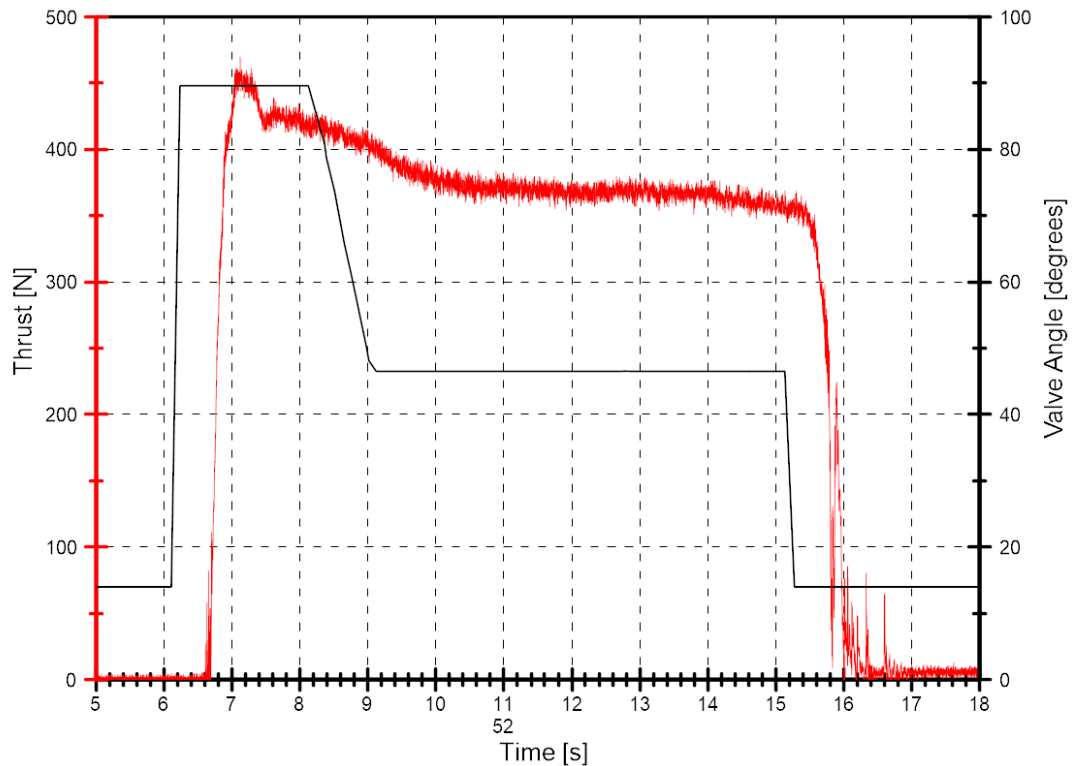
Figure 7.11: Measured thrust and valve angle over time

Test 7

Adjustments were again made to the controller and test 7 was conducted to allow a lower valve angle to be employed. Table 7.7 shows the parameters.

Table 7.7: Controller parameters for Test 7

Parameter	Value
Opening angle	90°
Set point	350 N
Proportional Gain [P]	1.25
Integrative Gain [I]	0.015

The aim of this hot fire test was to throttle the motor to a thrust of 350 N. Upon opening the valve and firing the motor, an Arduino™ module, used to control the servo motors via a LabVIEW™ Lynx™ plugin, vibrated loose and the system defaulted to shut the valves and purge the system. No useful throttle data was obtained but measurements of the fuel grain may be useful in the future for derivation of regression rate data and injector mass flowrate data.
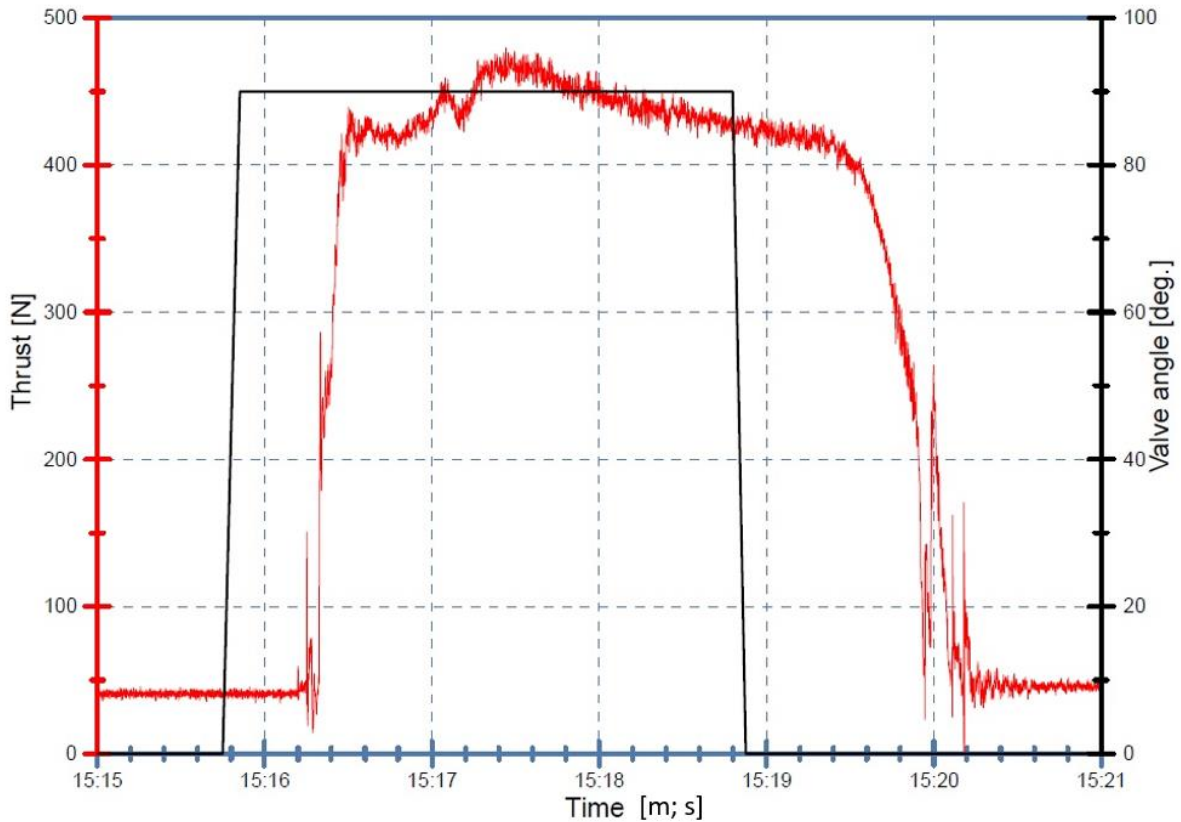
84

Figure 7.12: Thrust data and valve angle command

Test 8

Test 8 was the first closed-loop control test to successfully track the prescribed thrust set point. Parameters are shown in Table 7.8

Table 7.8: Initial parameters set for test 8

Parameter	Value
Opening angle	50°
Set point	370 N
Proportional Gain [P]	1.25
Integrative Gain [I]	0.015

After securing the Arduino™ control board, the test was rerun with similar parameters except that the valve was set to open to 50° and then to throttle the motor after 2 seconds. As seen from Figure 7.13, the valve opened to the predetermined value and after two seconds immediately closed to the maximum allowable minimum. Following this, there was a slow response of about 1.5 s until the motor reached the set point value of 370 N. The thrust then undershot the set point slightly for about two seconds

whereafter it oscillated with a maximum amplitude of 10 N on either side of the set point until the motor was commanded to shut down.
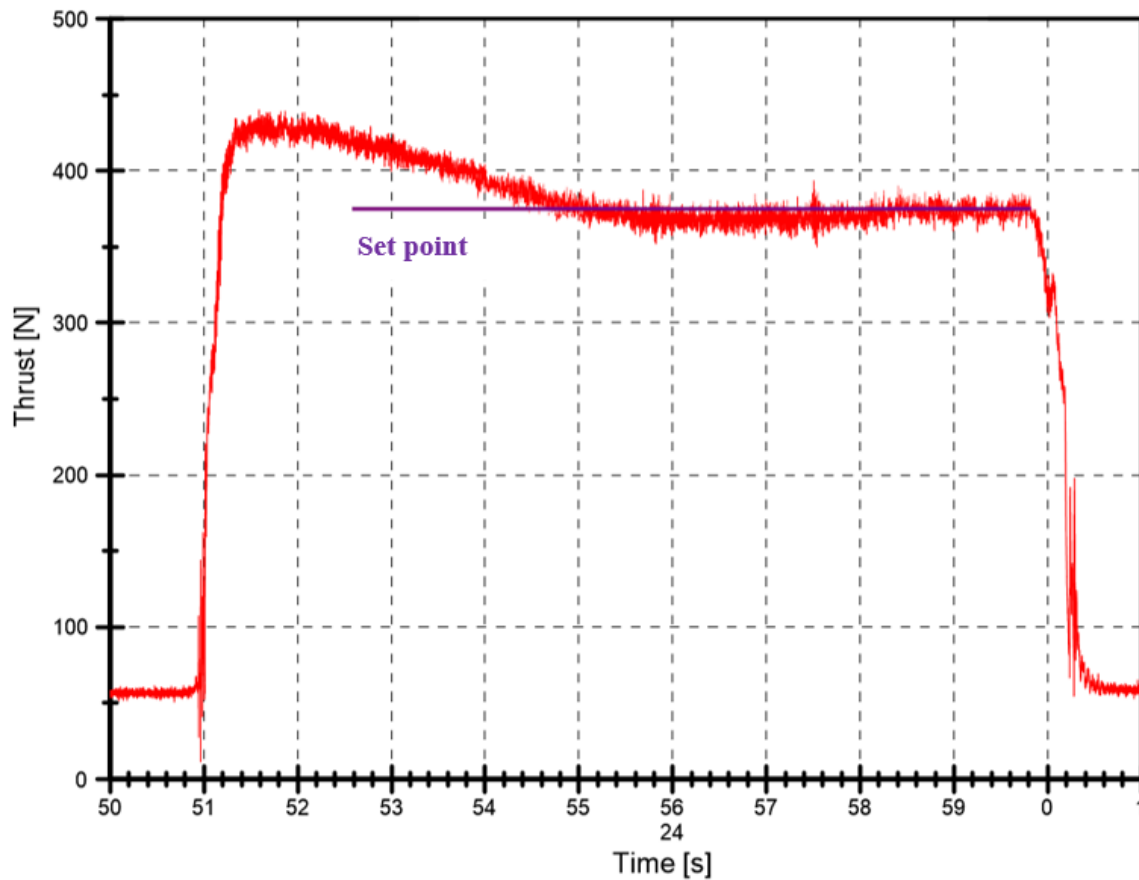

Figure 7.13: Thrust tracking set-point (signified by the purple line) over time.

This was the first hot-fire test in which the thrust successfully tracked and maintained the thrust set point and the controller behaved as designed. One issue of concern was the slow initial response time. There are various transients that may contribute to the overall response of the system as shown in Table 7.9, however they are all of relatively short duration and could not account for the two second response lag seen in this test. In addition, other tests done previously showed a much quicker response time to a change in oxidiser mass flowrate, such as Test 2, which demonstrated a very small lag from a change in valve angle to a change in thrust.

A second possible explanation for the slow response is that when the valve closes to its minimum allowable value, the oxidiser mass flowrate is still too high and therefore the O/F ratio is not low enough to decrease the thrust to the set point. Then, as the port of the fuel grain becomes larger over time, the O/F ratio shifts low enough to reach the thrust set point and then allow for controllability. A simple solution to this is to lower the minimum allowable valve angle.

Table 7.9: Transient timescales of various phenomena in a typical hybrid rocket (Karabeyoglu et al., 2005)

Physical phenomenon	Timescale	Explanation
Solid-phase kinetic times, s	$\tau_{sp} < 10^{-3}$	Degradation mechanisms of the polymer
Gas-phase kinetic times, s	$\tau_{gp} < 10^{-3}$	Hydrocarbon combustion mechanisms
Feed system response times	Varies greatly from system to system	Response time of the feed system
Evaporation times	$\tau_{evap} = f(U_o, T_1, \Delta P)$	Evaporation process of the liquid oxidizer
Thermal lags in solid, s	$\tau_{tl} \propto \kappa/\dot{r}^2 \approx 10^{-1}$	Thermal profile changes in the solid grain
Boundary-layer diffusion times, s	$\tau_{bl} \propto L/u_e \approx 10^{-1}$[b]	Turbulent boundary layer diffusion processes
Acoustic times (longitudinal), s	$\tau_a \propto L/c \approx 10^{-3}$[b]	Propagation of the acoustic waves
Gasdynamic filling times, s	$\tau_{fill} \propto L^*/c^* \approx 10^{-1}$[b]	Global mass flow balance

[b]Varies greatly from case to case.

Test 9

In Test 9 the set point was allowed to ramp up slowly. Parameters are shown in Table 7.10.

Table 7.10: Controller and set point parameters for thrust ramp test.

Parameter	Value
Opening angle	50°
Set point	370 N for 4 s
Ramp set point	To 410 N over 4 s
Proportional Gain [P]	1.25
Integrative Gain [I]	0.015

Following Test 8's successful tracking of a static set-point profile, the parameters were adjusted and a closed-loop test was run again, but with a varying set point. The set point was set to 370 N for four seconds and was then set to steadily increase to 410 N over the remaining four seconds of the burn. Figure 7.14 shows the thrust produced superimposed over the set point line and the valve angle. As per standard operation, the valve opened to 50° for the first one and a half seconds, thereafter the controller attempted to throttle the motor to 370 N. A similar issue was encountered as with the previous test; the thrust level decreased very slowly even though the valve angle was set to the minimum allowable value. After the valve reached its minimum angle value, a few minor oscillations can be seen which were attributed to noise from the thrust load cell.

Approximately five seconds into the burn, the thrust variable dipped below the set point line which subsequently caused the controller to begin opening the valve. When the valve angle reached 45° the thrust output became noisy and unresponsive. Although the average thrust did steadily increase at the same rate as the set point value, the thrust remained offset from the set point despite the valve angle increasing accordingly. It was conjectured that when the control valve began to open to throttle up the motor, the O/F ratio shifted too high and caused various combustion instabilities and uneven burning which resulted in an unsteady output.
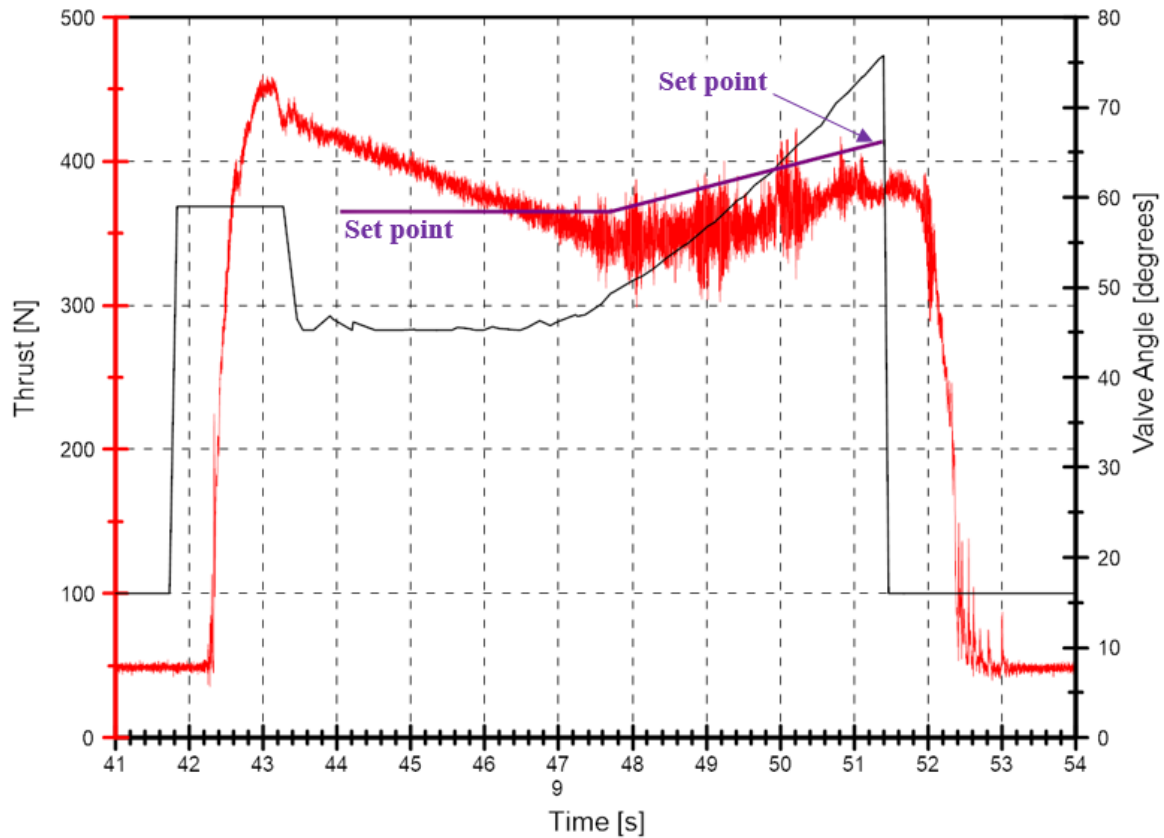
Figure 7.14: Set-point, shown in purple, and valve angle superimposed over measured thrust

Test 10

The final closed-loop control test was done using the chamber pressure as the feedback variable rather than the measured thrust. Relevant data is tabulated in Table 7.11.

Table 7.11: Parameters for pressure feedback closed-loop control.

Parameter	Value
Opening angle	50°
Set point	370 N
Proportional Gain [P]	1.25
Integrative Gain [I]	0.015

Test 10 was carried out to determine the control response using pressure feedback rather than thrust. Due to the difficulties in obtaining a value for thrust in flight, pressure and thrust values were correlated in order to accurately predict thrust at a given pressure. It has been shown by Peterson (2012) that a hybrid rocket motor's thrust is directly proportional to the combustion chamber pressure. Furthermore, chamber pressure and thrust output can be empirically correlated to an acceptable degree of accuracy

from graphical analysis of past hot-fire tests. Prior to Test 10, the necessary pressures required to obtain the prescribed thrust values were calculated and the controller was modified such that chamber pressure is the measured variable rather than the thrust value from the load cell.

The controller was given a pressure command of 24 bar to track for four seconds, followed by a step-down to 22 bar for a further four seconds after which the motor was commanded to shut off. It was estimated that at 24 bar the motor would achieve 330 N of thrust and at 22 bar, 310 N. Figure 7.15 shows the comparison between combustion chamber pressure and thrust for this test. The thrust scales up almost linearly from the chamber pressure values except when over about 370 N (about 25 bar). The directly proportional relationship between the two variables can be clearly seen here, allowing for the use of chamber pressure as the measured feedback variable. Figure 7.16 shows the chamber pressure tracking the command input. The response of the motor is noticeably slow and takes almost four seconds to reach 24 bar. After reaching the set point the pressure continues to drop, as seen in Test 8, and eventually rises after two second to reach the set point which is, at that moment, 22 bar. The pressure then tracks the set point for the remainder of the burn.
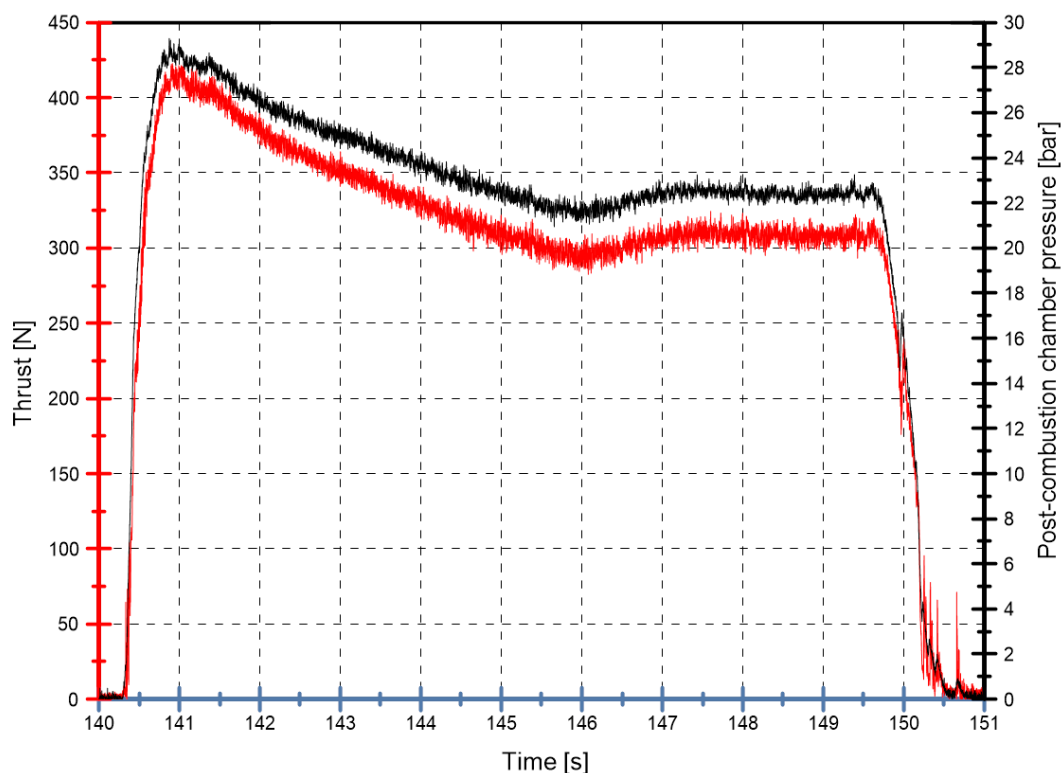

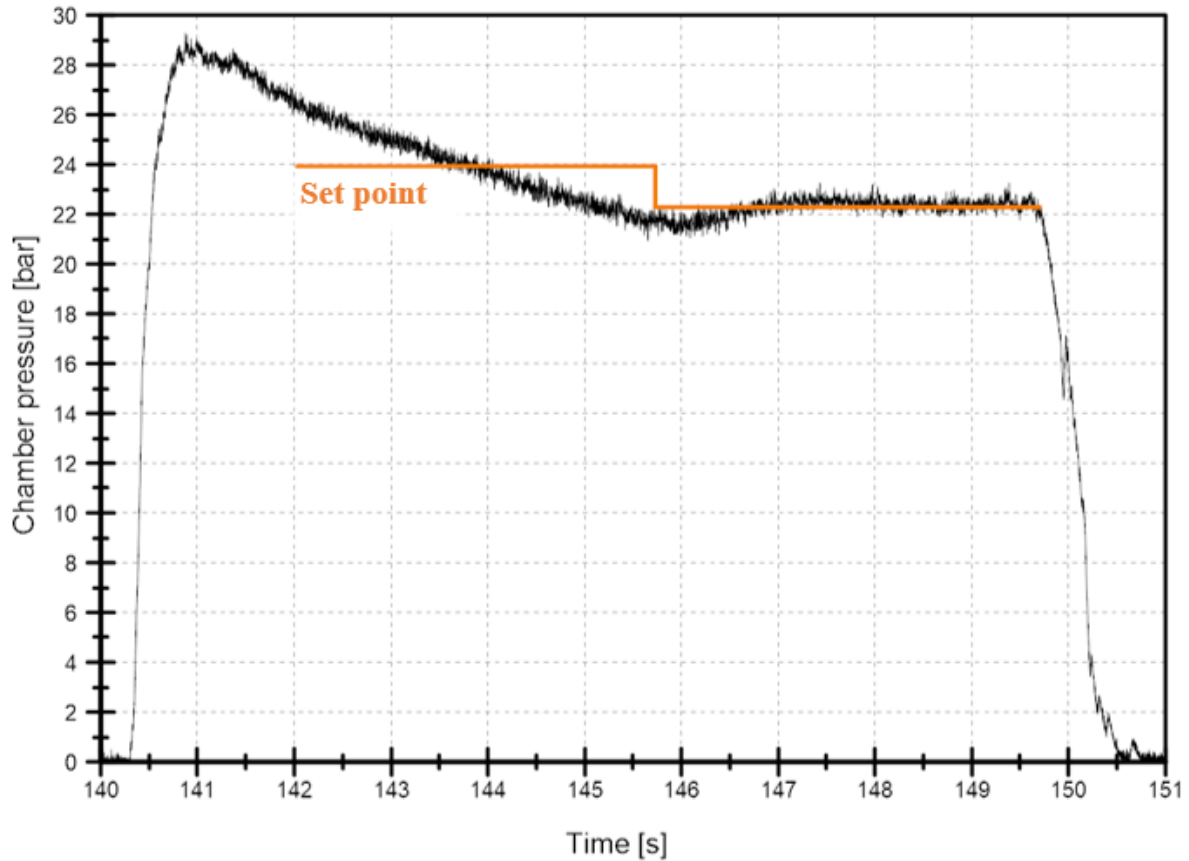Figure 7.15: Comparison chamber pressure and measured thrust

Figure 7.16: Chamber pressure tracking set point, signified by the orange line, in closed-loop pressure test

7.5 CONCLUSION

Initial throttling tests did not result in adequate thrust control and the controller response was erratic. This led to the refinement of the transfer function and the selection of better controller constants. The derivative aspect of the controller was removed to eliminate the effects of noise from the load-cell. A new injector was developed to limit oxidiser flow and thereby permit greater control authority by the valve. Successful control of the motor was demonstrated for a fixed set point using the combination of a feedback loop and coercion functions. In addition, control with a varying set point was also achieved. Finally, chamber pressure was used as the feedback variable to demonstrate that throttling of a hybrid rocket is possible in the absence of thrust measurements from a ground-based load cell.

8   CONCLUSION

8.1   OVERVIEW

The primary objective of this research was to design and test a control regime for the throttling of a paraffin wax/N_2O hybrid rocket motor, by modulating the oxidiser flowrate. The controller was required to be robust and stable as well as to be able to fit a wide variety of applications. At the outset of this study it was not known how well this particular propellant combination would respond to throttling so a further objective was to determine which throttling applications are most acceptable. This study describes the research, design and construction of a controller and related hardware and software for the thrust modulation of a laboratory-scale hybrid rocket motor, including a predictive simulator of the laboratory-scale motor.

8.2   AIMS AND CONCLUSIONS

The conclusions that are presented here are in reference to the aims described in Chapter 1:

1. *Develop a mathematical model of the laboratory-scale hybrid rocket motor*

In order to predict the response of the motor and potentially negate the need to perform multiple hot-fire tests in order to characterise the response of the motor, a simulator was designed to test various control parameters before implementing them on the physical laboratory-scale motor. The simulator borrowed from the HRPC MATLAB™ code already developed by a previous student (Genevieve, 2013), mostly modifying physical characteristics and simplifying sections of code as described in Chapter 4. The simulator required characterisation of the relationship between oxidiser flowrate and valve angle, and this was achieved using CFD modelling from which the results were extrapolated and embedded in the code.

2. *Use the model to determine the controller constants that best describe the desired response of the motor*

Using the simulator, control parameters were selected and used to construct the controller. The constants were continually adjusted until the controller produced satisfactory outputs. The rise-time, settling-time and steady state error were all taken into account in the selection on the controller constants. The controller was initially designed to be a PID controller with a reduced sample rate, but as observed in the first closed-loop test in Chapter 7, the response was erratic and not useful in controlling the motor. Thus the derivate term was dropped and a restriction was placed on the servo motor's rotation speed. Overall, the model proved to be useful in selecting initial controller constants and greatly diminished the time and resources required if the constants were selected based purely off empirical testing. The controller constants were slightly tweaked after hot-fire testing to better control the physical motor.

3. Design and select hardware required to throttle the flowrate of oxidizer into the chamber

A number of flow control solutions were considered whereafter a through-port ball valve was selected to control the oxidiser flowrate into the combustion chamber. Two high-torque DC electric servo motors were used to manipulate the valve and throttle the flow of oxidiser. Due to the difficulty in mathematically modelling cavitation and two-phase flow through a throttled valve, the steady flow through the ball valve was modelled for various valve angles using CFD and a table constructed correlating the mass flowrate with the valve angle. This is detailed in Chapter 4. The mass flowrate of the nitrous oxide was calculated by weighing the tank with a load cell over the duration of the burn, the output is differentiated over time in order to obtain the oxidiser mass flowrate.

4. Perform open-loop hot-fire tests on the laboratory-scale motor to obtain limits of throttlabilty

Open-loop tests were done to determine the control authority of the valve as well as to roughly characterise the relation of valve angle to thrust output. The first open-loop test was inconclusive and so more were done with slower closing times toward the end of the valve operating range. This yielded much clearer results and showed a non-linear relation between valve angle and oxidiser flowrate. These tests showed that the motor with a nominal thrust output of 500 N could be throttled down to approximately 300 N without becoming unstable over a total burn-time of 12 s. This translates to a turndown ratio of 1.67:1. It was also concluded that the control authority of the valve spanned from 45° to approximately 65°. A combination of open-loop control, to obtain the approximate thrust value, and closed-loop control, to adjust the thrust more precisely to the prescribed value, was used. This method was abandoned due to insufficient disturbance rejection qualities and instead substituted with full closed-loop control with embedded code to coerce the output angle value to a specific, predetermined value. This is described in Chapter 5.

5. Demonstrate closed-loop thrust control on the laboratory-scale motor

Very little research on closed-loop throttle control of hybrid rocket motors has been done and almost none with a paraffin wax/N$_2$O propellant combination. Through a series of incrementally improving hot-fire tests, this work demonstrates successful closed-loop throttle control using a readily available ball valve as the flow control element. Three successful tests were done showing the closed-loop thrust control over the laboratory-scale motor. The first test used the motor thrust measured by the load cell as feedback to modulate the oxidiser flowrate and therefore, the thrust of the motor to follow a prescribed set-point profile. The profile was set to a constant thrust which the controller achieved after two seconds with only a slight under-shoot. The second successful test followed a ramp-up profile which the controller followed with reasonable accuracy. The thrust output had a delayed response which produced an offset to the profile. The thrust also became unstable as the oxidiser flowrate was increased.

Additionally, the motor was successfully throttled using combustion chamber pressure as the feedback variable. Chamber pressure has been shown to be directly proportional to thrust produced by the motor as described in Chapter 7. The set-point profile was a constant thrust for three seconds followed by a small step to a lower thrust. The controller took three seconds to reach the profile, after which it followed it with a reasonable degree of accuracy. Despite difficulties encountered, this study has demonstrated that it is possible to exercise a moderate level of thrust control over a liquefying fuel hybrid rocket motor, using a low-cost ball valve as the main oxidiser flow control element.

8.3   RECOMMENDATIONS AND FUTURE WORK

The control authority of the main oxidiser flow valve in a liquefying fuel hybrid rocket motor is very restricted, and only affects the thrust at the very lower limits of the allowable valve angle. This means that control over the motor is difficult to achieve when small changes in valve angle produce large changes in thrust. Compounding this is the fact that the gears that drive the valve from the servo motors in this study were 3D printed ABS plastic. Although care was taken to manufacture them as accurately as possible, the gears still flex slightly under load which makes it difficult to get an accurate angle versus thrust profile. A more direct method of modulating the oxidiser flow is recommended, such as a rotatable plate mated to the injector which could change the effective area of each injector port quickly and accurately.

It has been shown mathematically that the thrust of a hybrid rocket motor can be modulated by adjusting the angle of the ball valve and thereby controlling the mass flowrate of the oxidiser in Chapter 5. Although this has also been shown experimentally on the laboratory-scale motor, the results are not as clear as predicted. First, the paraffin wax/N_2O hybrid rocket motor does not have a very large turndown ratio compared to a HTBP-nitrous oxide motor (Peterson, 2012). This is speculated to be a result of using higher regression rate fuels. Second, it was seen that the motor typically responds very sluggishly, especially toward the beginning of the test. Third, the motor does not respond well to the step-up or ramp-up commands, producing a number of instabilities and inadequate response times. Further research is recommended in this area to determine the reason for the slow response of paraffin wax/N_2O hybrid rocket motors, as well as the instabilities produced when attempting to throttle-up the motor.

In terms of practical applications, this propellant combination is not suitable for throttling in situations where precise, rapid response is required, but rather for applications where an accurate and stable thrust is demanded and where slow response is acceptable. Since hybrid rockets are used primarily for sounding and for scientific experiments, the level of control demonstrated here should be acceptable. It also has applications where sensitive electronic equipment is part of the payload, and requires low acceleration to avoid damage, a throttled hybrid rocket could start with a very low thrust and gradually increase to nominal thrust levels.

A throttled paraffin wax/N_2O hybrid rocket might also find application where a very specific altitude is required, such as in meteorology. A throttled motor combined with predictive software, such as the HYROPS software developed at UKZN (Chowdhury, 2012), could ensure the correct altitude is reached. Finally, although test three of the closed-loop testing regime failed the test aims, it inadvertently showed that a paraffin wax-N_2O motor can be restarted. During Test 3, the motor was inadvertently shut off because of insufficient oxidiser, however the valve was commanded to open fully after 3 s which caused a hard start and an overpressurization event chronicled in Chapter 7. This event, although unplanned, showed that even after the motor was shut down, it could still be restarted provided the combustion chamber temperature was high enough. This has many potential applications including in the performance of orbital manoeuvers.

9   REFERENCES

Altman, D. (1991). Hybrid Rocket Development History. *American Institute of Aeronautics and Astronautics, Inc*. 27 (1), p1-20.

Altman, D; Holzman, A. (2007). Overview and History of Hybrid Rocket Propulsion. *American Institute of Aeronautics and Astronautics*. 218 (1), pp1-33.

Arves, J., Gnau, M., Joiner, K., Kearsney, D., McNeal, C., and Murback, M. (2003). Overview of the Hybrid Sounding Rocket (HYSR) Project. *American Institute of Aeronautics and Astronautics*. 5199

Balmogim, U (2017). *Design and Development of the Phoenix-1B Hybrid Rocket*. Durban, South Africa: University of KwaZulu-Natal. p57.

Blau, P. (2013). *SpaceShipTwo performs first Rocket-Powered Flight*. Available: http://www.spaceflight101.com/spaceshiptwo-first-powered-test-flight.html. Last accessed 27th Aug 2018.

Boiron, A; Cantwell, B. (2013). Hybrid Rocket Propulsion and In-Situ Propellant Production for Future Mars Missions. *49th AIAA/ASME/SAE/ASEE Joint Propulsion Conference and Exhibit*.

Brooks, M. J., Pitot de la Beaujardiere, J. F., Genevieve, B., Chowdhury, S. M. and Roberts, L. W., 2010. Introduction to the University of KwaZulu-Natal Hybrid Sounding Rocket Programme. *46th AIAA/ASME/SAE/ASEE Joint Propulsion Conference & Exhibit.* Nashville, TN, United States of America, 25-28 July, pp1-14.

Chowdhury, S. M., 2012. *Design and Performance Simulation of a Hybrid Sounding Rocket,* MScEng Thesis, Durban: University of KwaZulu-Natal.

Culick, F. (1996). Combustion Instabilities in Propulsion Systems. *Unsteady Combustion*. 306 (9), pp173-227.

David, L. (2012). *Virgin Galactic to Launch Passengers on Private Spaceship in 2013*. Available: https://www.space.com/16057-virgin-galactic-spaceshiptwo-launches-2013.html. Last accessed 27th Aug 2018.

Doran, E., Dyer, J., Marzona, M.T., Karabeyoglu, A., Zilliac, G., Mosher, R., and Cantwell, B., "Status Update Report for the Peregrine Sounding Rocket Project: Part III", *AIAA 2009-4840*, 2009.

Duban, P., (1968). The LEX rocket probe (LEX small rocket probe for in-flight testing of ONERA studies of hybrid propulsion, discussing design and programme). *L'Aeronautique et L'Astronautique*. pp47-54.

Dyer, J., Doran, E., Dunn, Z., and Lohner, K., "Design and Development of a 100 km Nitrous Oxide/Paraffin Hybrid Rocket Vehicle", *43rd AIAA/ASME/SAE/ASEE Joint Propulsion Conference & Exhibit*, Cincinnati, OH, United States of America, 8-11 July 2007.

Flittie, K. J., Estey, P.N., and Kniffen, R. (1992). The Aquilla Launch Vehicle: A Hybrid Propulsion Space Booster. *Acta Astronautica*. 28, pp99-110.

Franklin, B., Mead, J., Bornhorst, B.R., (1969). Certification Tests of a Hybrid Propulsion System for the Sandpiper Target Missile. *AFRPL-TR-69-73*.

Genevieve, B (2013). *Development of a Hybrid Sounding Rocket Motor*. Durban, South Africa: University of KwaZulu-Natal. p2.

Gordon, S., and McBride, B. J., "Computer Program for Calculation of Complex Chemical Equilibrium Compositions and Applications", NASA RP-1311, 1994.

Hamers, J. (1967). Experimental Investigation of Prepackaged Hybrid Propellant Systems. *AFRPL-TR-67-168*.

Henry, R. E. and Fauske, H. K., "The Two-Phase Critical Flow of One- Component Mixtures in Nozzles, Orifices, and Short Tubes*," Journal of Heat Transfer,* May 1971, pp. 179–187.

Karabeyoglu, M. A., Cantwell, B. J., and Altman, D., "Development and Testing of Paraffin-based Hybrid Rocket Fuels", *Proceedings of the 37th AIAA/ASME/SAE/ASEE Joint Propulsion Conference & Exhibit*, July 8-11, 2001, Salt Lake City, Utah.

Karabeyoglu, M. A., Altman, D., Cantwell, B. J, "Combustion of Liquefying Hybrid Propellants: Part 1, General Theory", *Journal of Propulsion and Power*, Vol. 18, No. 3, May-June 2002.

Kobald, M., Fischer, U., Tomilin, K., Petrarolo, A. (2018). Hybrid Experimental Rocket Stuttgart: A Low-Cost Technology Demonstrator. *American Institute of Aeronautics and Astronautics*. 55 (2), pp. 484-500

Knop, T., Huijsman, R., Powell, S., Werner, R., Ehlen, J., Lindermann, F., Wink, J., Becker, C., Samarawickrama, K., Zandbergen, B. and Vervone, A., 2013. Sorbitol-Based Hybrid Fuel Studies with Nitrous Oxide for the Stratos II Sounding Rocket. 49th AIAA/ASME/SAE/ASEE Joint Propulsion Conference & Exhibit. San Jose, CA, United States of America, 14-17 July.

Kniffen, R., McKinney, B., and Estey, P. (1990). Hybrid Rocket Development at the American Rocket Company. *American Institute of Aeronautics and Astronautics*. 90 (2762)

Leverone, F (2013). *Performance Modelling and Simulation of a 100 km Hybrid Sounding Rocket*. Durban, South Africa: University of KwaZulu-Natal. p3.

Maharaj, C (2018). *Performance Characterisation of Metal Additives in Paraffin Wax Hybrid Rocket Fuel Grains*. Durban, South Africa: University of KwaZulu-Natal.

Maritz, W., Govender, S., Premlall, R. (2017). *Hybrid Rocket Motor Test Facility*. Durban, South Africa: University of KwaZulu-Natal. pp60-63.

Mathworks. (2006). *Rise time, settling time, and other step-response characteristics.* Available: https://www.mathworks.com/help/ident/ref/stepinfo.html. Last accessed 25th July 2018.

Moore, G.E. and Berman, K., (1956). A Solid-Liquid Rocket Propellant System. *Jet Propulsion*. 26 (11), pp965-968.

National Aeronautics and Space Administration. (1973). State of the art. In: Douglass, H., Keller, R. *Liquid Rocket Valve Components*. Cleveland, Ohio: National Aeronautics and Space Administration, Lewis Research Centre. pp4-5.

Parissenti, G., Pessana, M., Gaia, E., Pavarin, D., Bettella, A., Ronningen, J., Put, P., Van Popola, R., Pistek, A., Mammarella, M., Grandou, D., Stasse, V. (2011). Throttleable hybrid engine for planetary soft landing. *Gaia Ecological Perspectives for Science and Society*. 4, p2.

Penn, C.D. and Branigan, J.E., (1975). Preliminary Flight Tests of the HAST Propulsion System. *AFRPL-TR-15-5*.

Peterson, Z.W. (2012). *Closed-Loop Thrust and Pressure Profile Throttling of a Nitrous Oxide/Hydroxyl-terminated Polybutadiene Hybrid Rocket Motor*. Logan, Utah: Utah State University.

Pump and Systems. (2011). *Surge Control in Pumping Stations.* Available: https://www.pumpsandsystems.com/topics/valves/surge-control-pumping-stations?page=5. Last accessed 24th November 2016.

Smith, C., Copripio, A. (1985). *Principles and Practice of Automatic Process Contro*. New Jersey: John Wiley & Sons. p65.

Spalding, D.B, Jain, V.K. (1959). Theory of the Burning of Monopropellant Droplets. *Aeronautical Research Council*.

STAR-CCM+, 2015. *STAR-CCM+ User Guide Version 9.06,* United States of America: CD-adapco.

Stienecker, A. (2011). *General PID control.* Available: https://drstienecker.com/tech-332/7-pid-control/. Last accessed 14th August 2018.

Sutton, G; Biblarz, O (2001). *Rocket Propulsion Elements*. 7th ed. Canada: John Wiley & Sons. p579-580.

Tabor, A. (2017). *From Pedicures to the Peregrine Rocket, Paraffin Wax Proves Its Worth.* Available: https://www.nasa.gov/feature/ames/from-pedicures-to-the-peregrine-rocket-paraffin-wax-proves-its-worth. Last accessed 24th May 2017.

Thiokol Corporation - Space Operations (1989). *Hybrid Propulsion Technology Programme Phase I Final Report*. 1: NASA/Marshall Space Flight Center. pp1-3.

Waxman, B.S (2014). *An Investigation of Injectors for Use with High Vapour Pressure Propellants with Applications to Hybrid Rockets*. California: Stanford University.

Zilliac, G. and Karageyoglu, A. M., 2006. *Hybrid Rocket Fuel Regression Rate Data and Modelling.* Sacramento, 42nd AIAA/ASME/SAE/ASEE Joint Propulsion Conference and Exhibit.

APPENDIX A: CFD RESULTS ON VALVE

Valve angle at 51.5°

What follows are the CFD results from the intermediate angle, 51.5° and all relevant data pertaining to it.
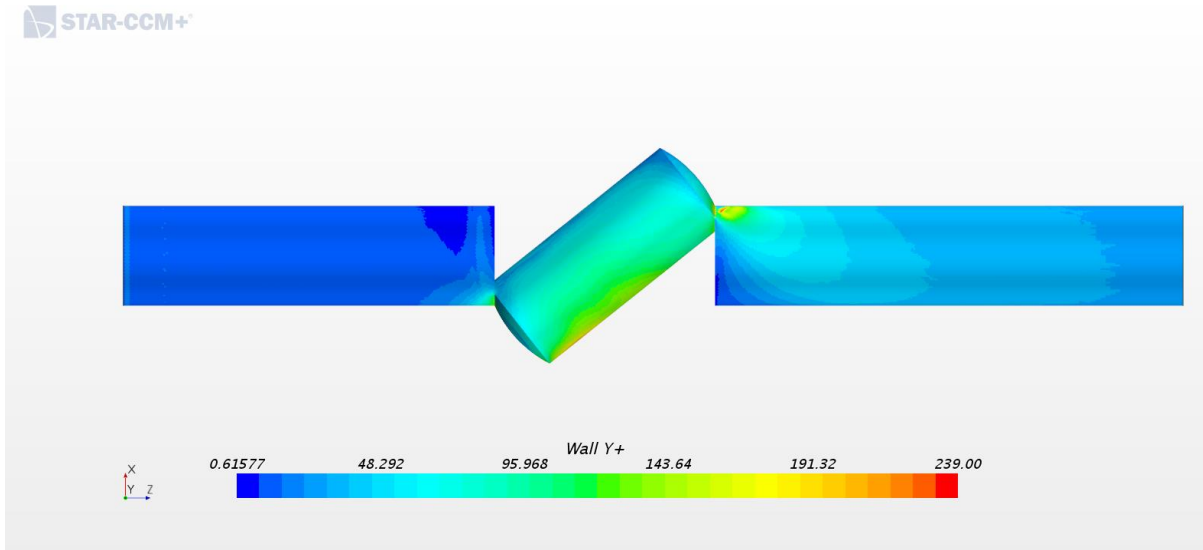
Figure A.1: Graphic showing wall Y+ values. Most of the wall surface is between the 30 and 300 range
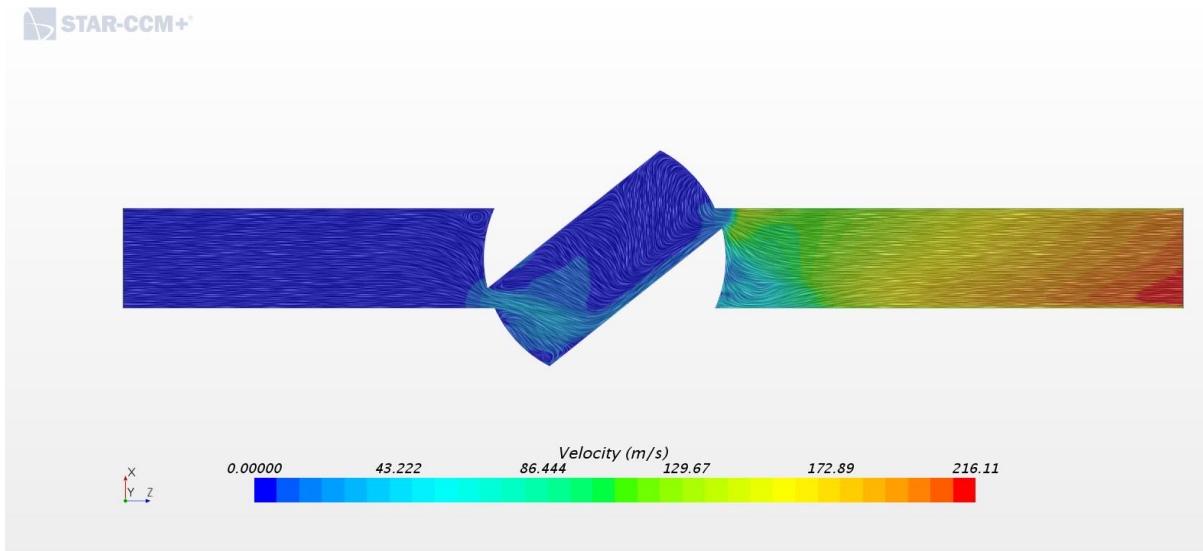
Figure A.2: Convoluted line integral diagram showing velocity vectors and contours
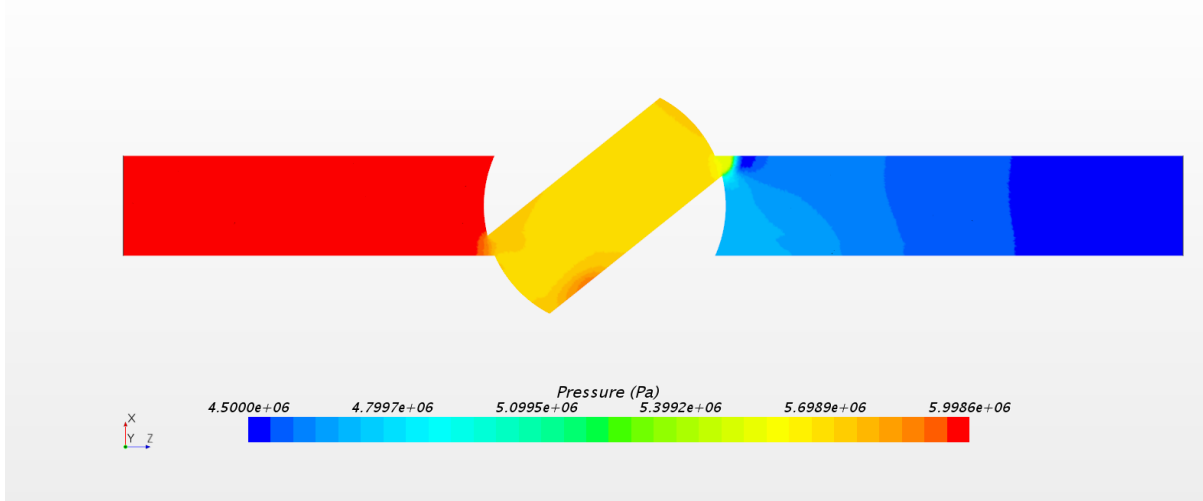
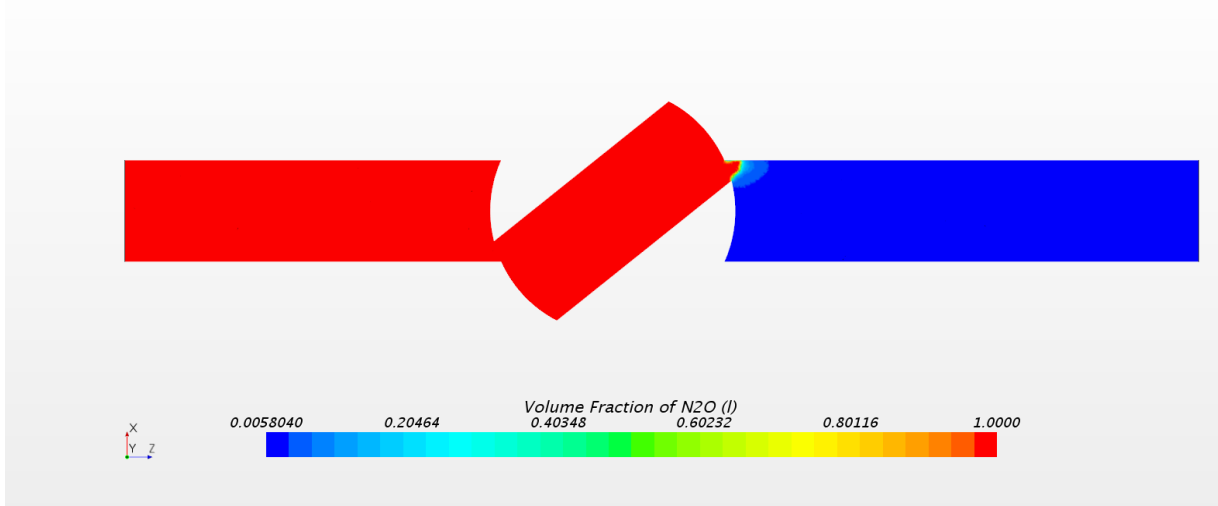Figure A.3: Illustration of pressure gradient distribution through valve.

Figure A.4: Graphic showing volume fraction through valve. Here the CFD software predicts that the flow will be fully gaseous upon exiting the ball section of the valve.
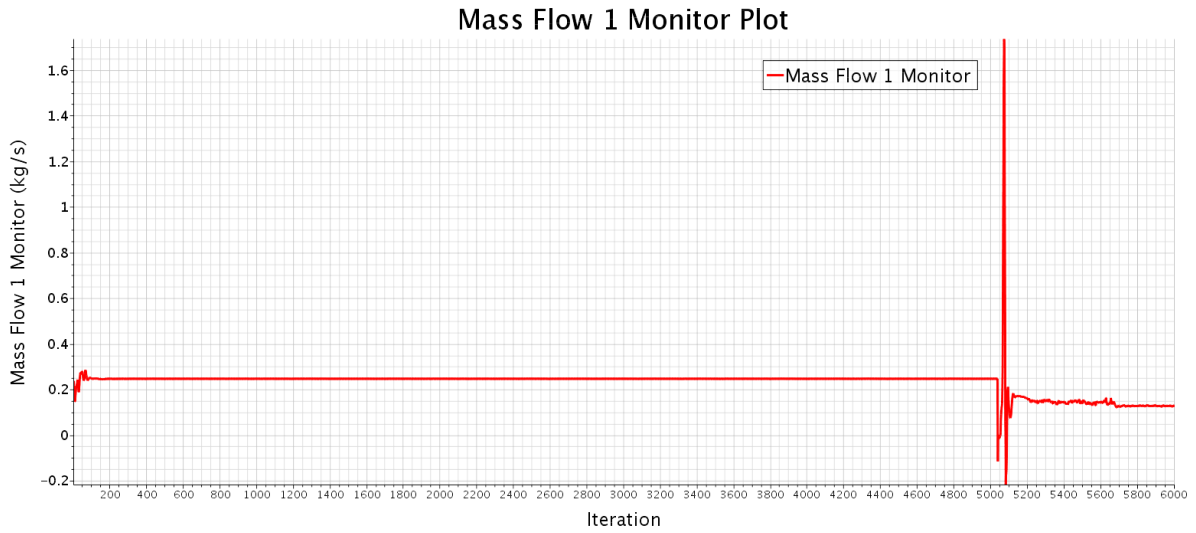
Figure A.5: Mass flowrate monitor at valve angle of 51.5°. Nominal mass flowrate was 0.125 kg/s.
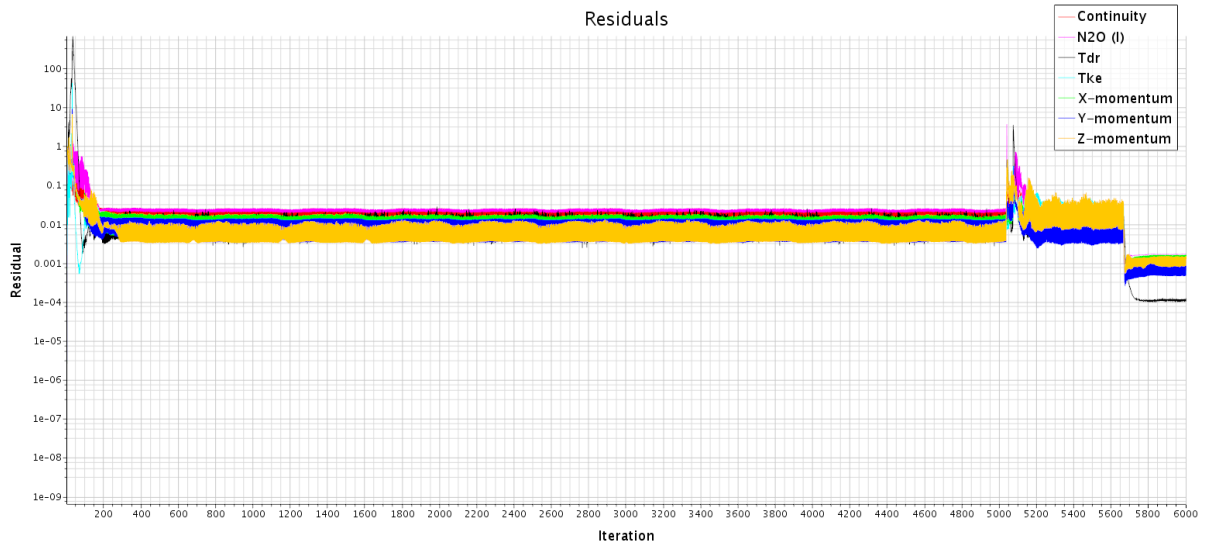
FigureA.6: Residuals for 51.5° valve angle simulation. After 5000 iterations, parameters were changed to more accurately reflect the physical set up.

Valve at 65.5°

All relevant CFD data obtained from the valve at the 65.5° position is shown below.
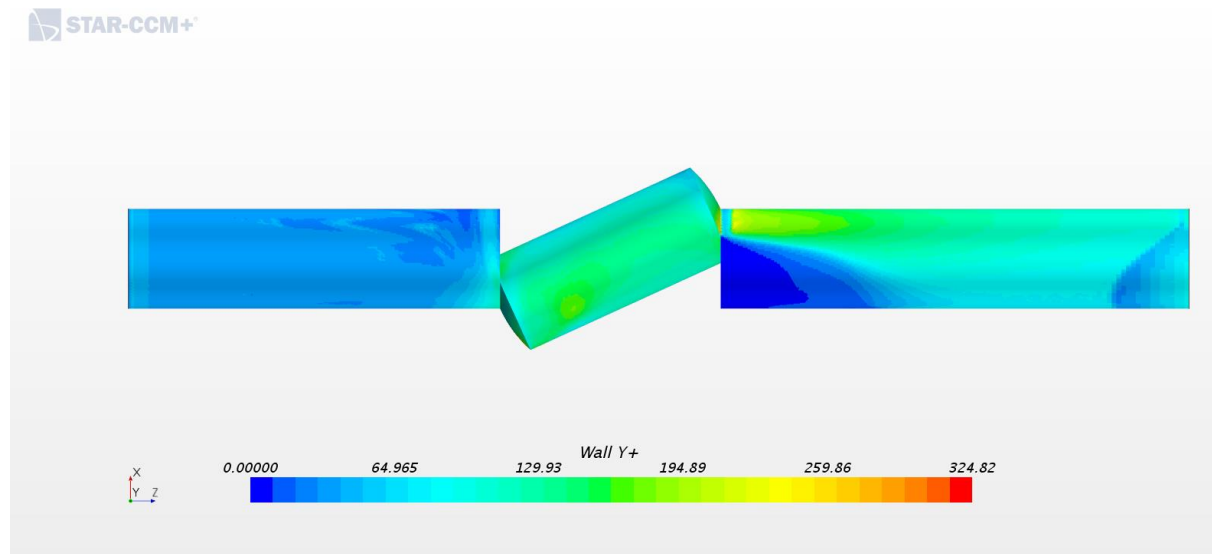

Figure A.7: Wall Y+ values for the valve at 65.5°. Most of the values fall within the high wall Y+ range of 30 – 300.
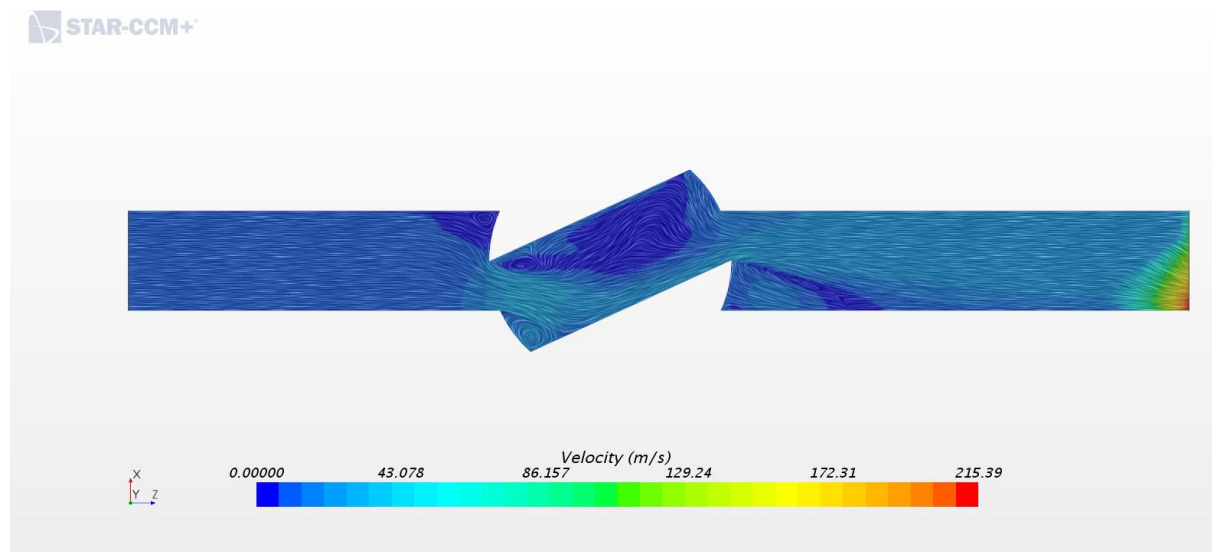

Figure A.8: Velocity vectors through the valve. Areas of slow moving flow can be seen just before, inside and just after the ball.
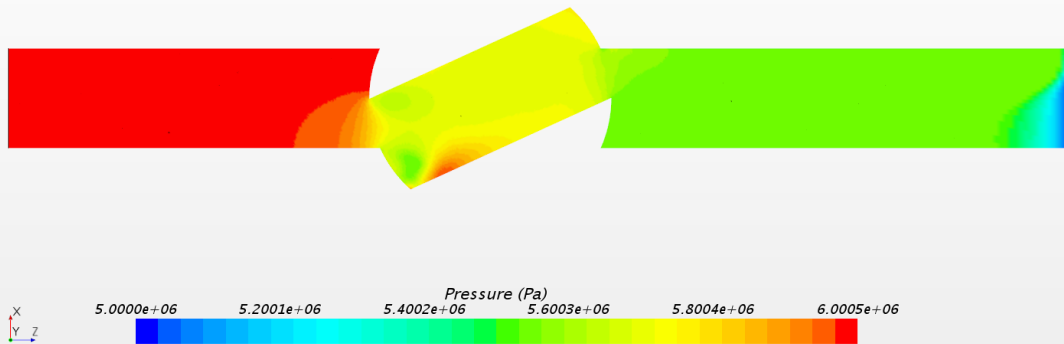
Figure A.9: Pressure gradient through the ball valve. This figure suggests the flow is at vapour pressure after exiting the ball section.
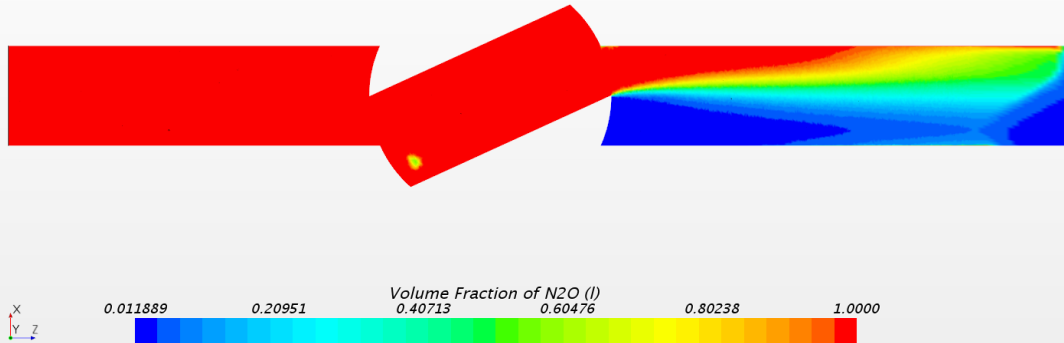

Figure A.10: Volume fraction where red is fully liquid and blue is fully vapour.
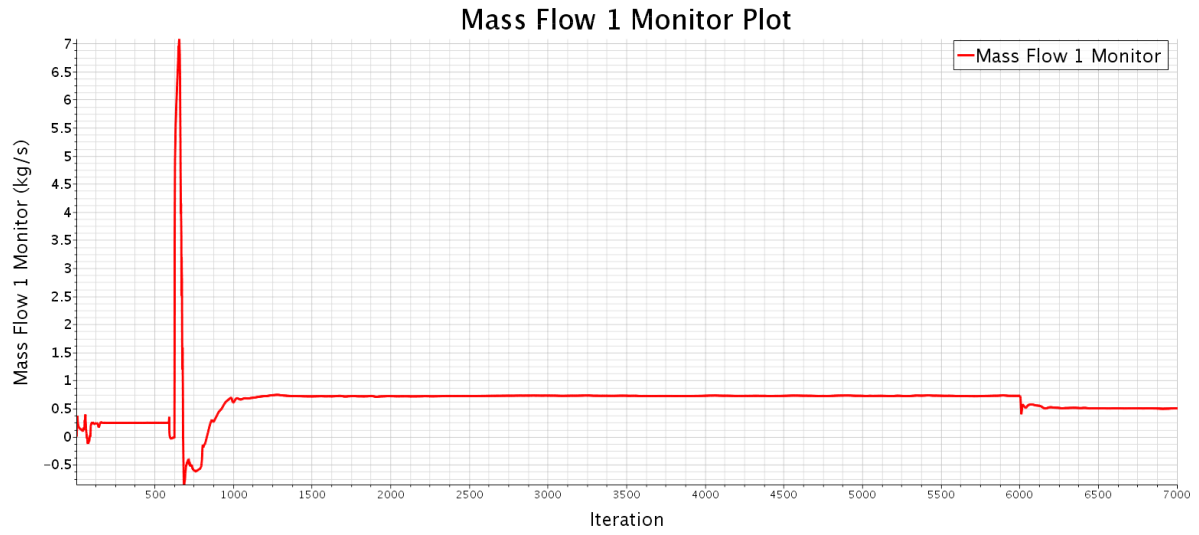
Figure A.11: Mass flowrate result from valve at 65.5° angle. Nominal mass flowrate is approximately 0.5 kg/s
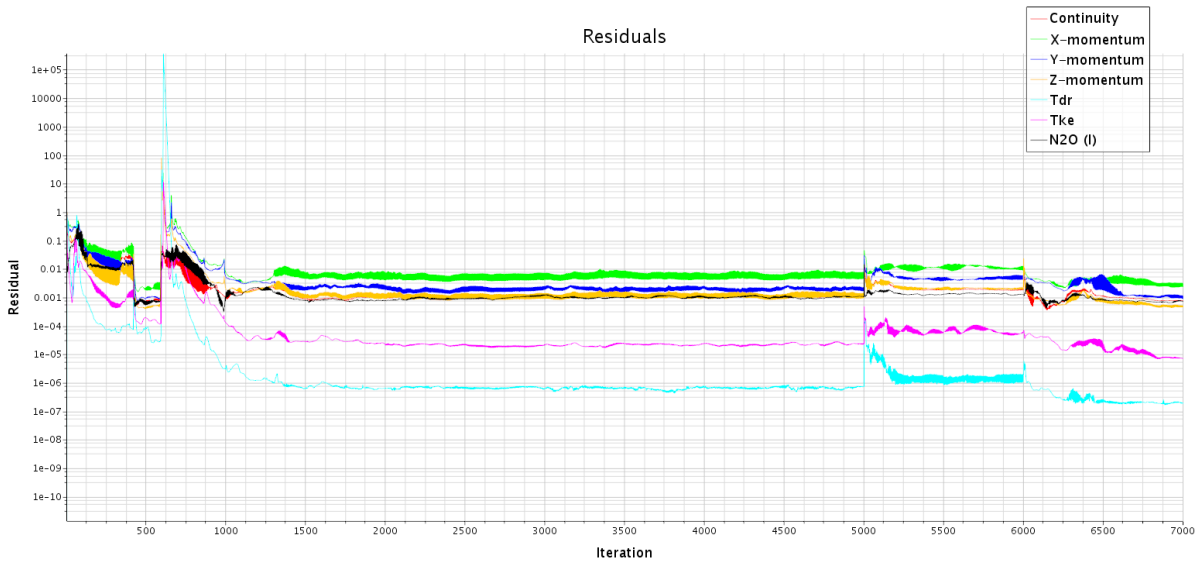

Figure A.12: Residuals for 65.5° valve angle simulation
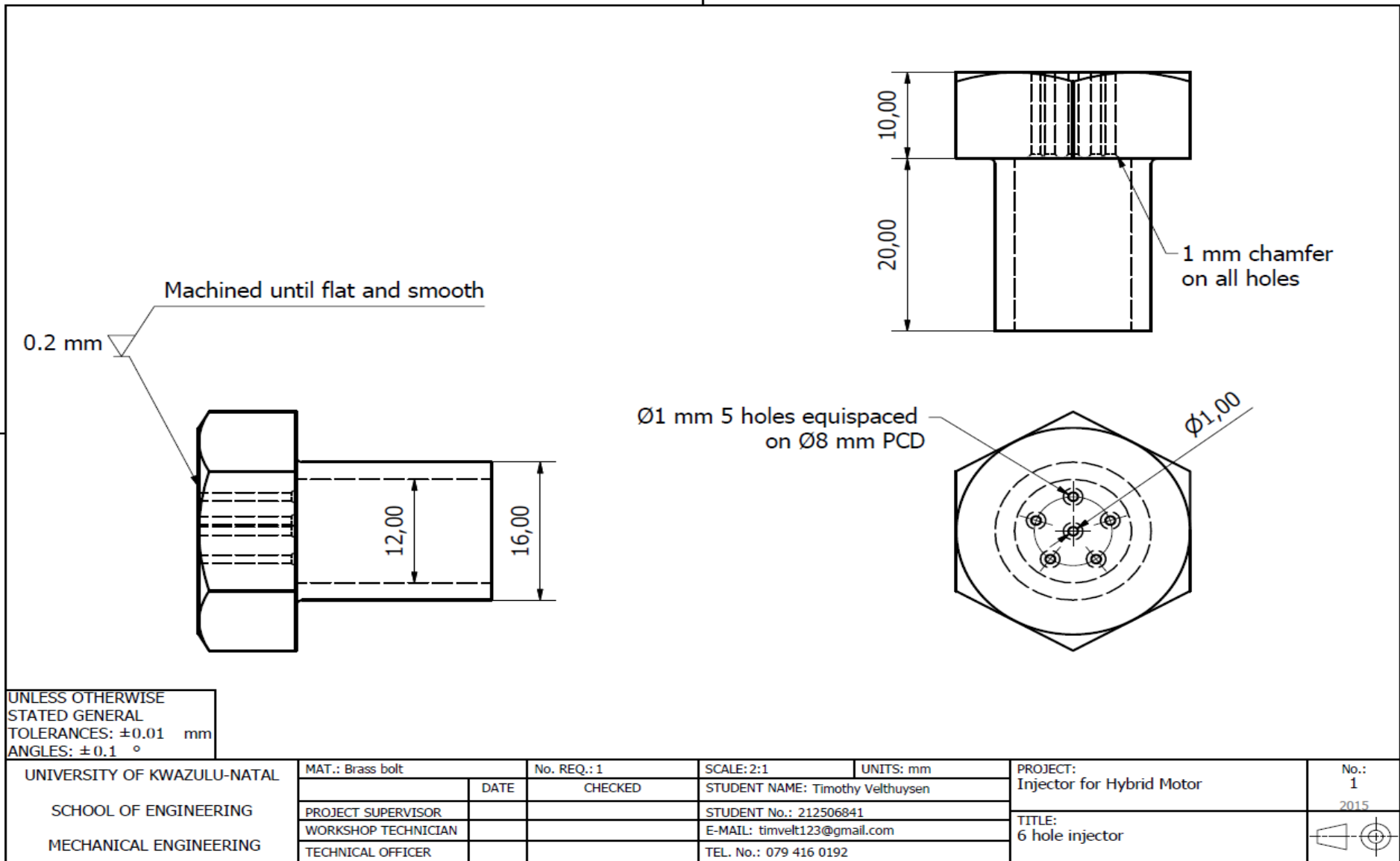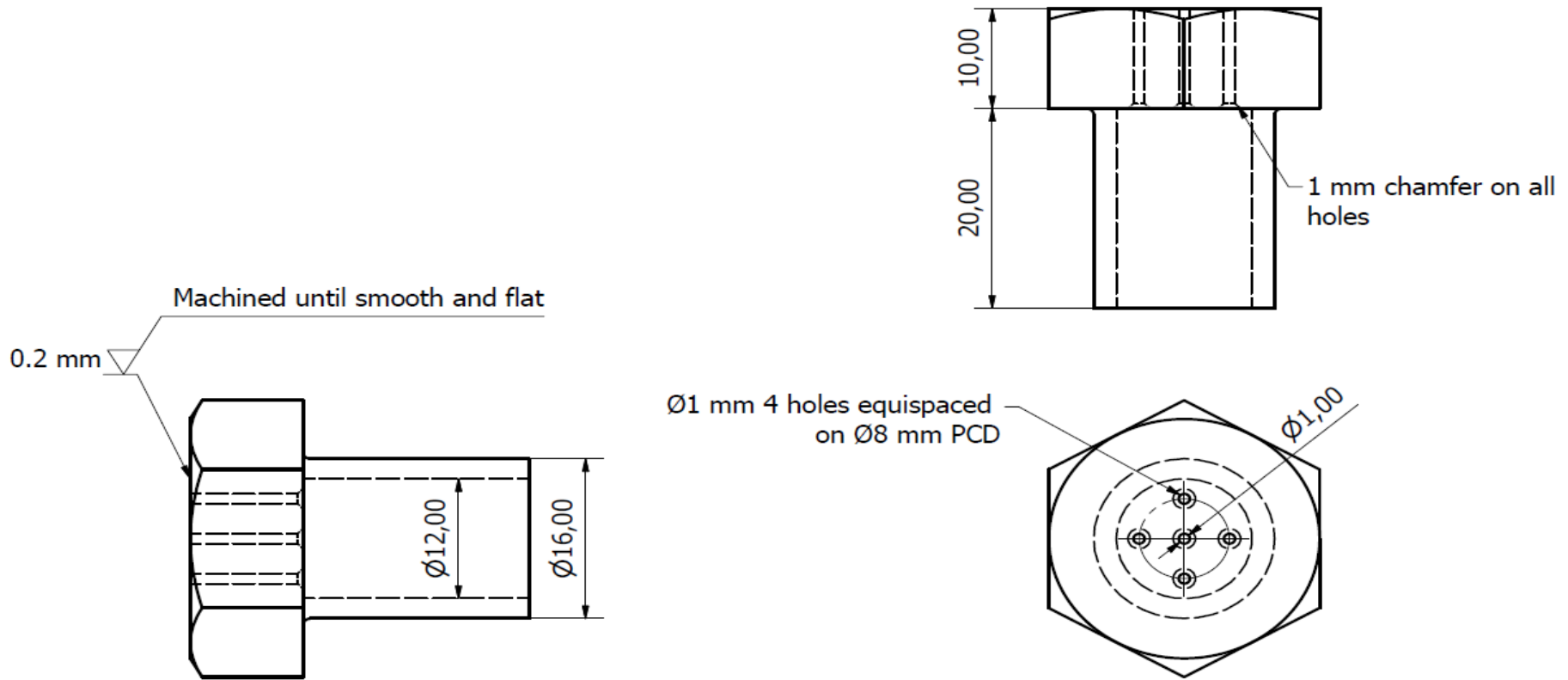
APPENDIX B: INJECTOR DRAWINGS

Drawings of new injector

Machined until flat and smooth

0.2 mm

10,00

20,00

1 mm chamfer
on all holes

12,00

16,00

Ø1 mm 5 holes equispaced
on Ø8 mm PCD

Ø1,00

Figure B.1: 6-hole injector drawing

10,00

20,00

1 mm chamfer on all holes

Machined until smooth and flat

0.2 mm

Ø1 mm 4 holes equispaced on Ø8 mm PCD

Ø1,00

Ø12,00

Ø16,00

UNLESS OTHERWISE STATED GENERAL TOLERANCES: ±0.01 mm
ANGLES: ±0.1 °

UNIVERSITY OF KWAZULU-NATAL	MAT.: Brass		No. REQ.: 1		SCALE:		UNITS: mm	PROJECT: Injector for Hybrid Motor		No.: 1
		DATE	CHECKED		STUDENT NAME: Timothy Velthuysen					
SCHOOL OF ENGINEERING	PROJECT SUPERVISOR				STUDENT No.: 212506841			2015		
	WORKSHOP TECHNICIAN				E-MAIL: timvelt123@gmail.com			TITLE: 5 hole injector		
MECHANICAL ENGINEERING	TECHNICAL OFFICER				TEL. No.: 079 416 0192					

Figure B.2: 5-hole injector drawing

APPENDIX C: HOT-FIRE TESTING VIDEOS

Open-loop tests:

Designator	Date	Burn Time
Test 1	30-10-2017	10 s
Test 2	03-11-2017	7 s
Test 3	21-11-2017	6 s

Closed-loop tests:

Designator	Date	Burn Time
Test 1	30-11-2017	12 s
Test 2	08-12-2017	12 s
Test 3	15-12-2017	4 s
Test 4	02-03-2018	2 s
Test 5	08-03-2018	10 s
Test 6	24-04-2018	9 s
Test 7	11-05-2018	3.5 s
Test 8	23-05-2018	9 s
Test 9	01-06-2018	11 s
Test 10	04-07-2018	10 s

See attached digital media for footage and test data in TDMS format